

Measurement of the stopping power of water
for carbon ions in the energy range of 1 MeV -
6 MeV using the inverted Doppler-shift
attenuation method

Dissertation
zur Erlangung des mathematisch-naturwissenschaftlichen Doktorgrades
"Doctor rerum naturalium"
der Georg-August-Universität Göttingen
—
im Promotionsprogramm ProPhys
der Georg-August University School of Science (GAUSS)

vorgelegt von
Johannes Martin Rahm
aus Fulda
Göttingen, 2016

Betreuungsausschuss

Prof. Dr. Hans-Christian Hofsäss, II. physikalisches Institut, Universität Göttingen

Dr. Ulrich Vetter, II. physikalisches Institut, Universität Göttingen

Dr. Hans Rabus, Fachbereich 6.5 Strahlenwirkung, Physikalisch-Technische
Bundesanstalt Braunschweig

Mitglieder der Prüfungskommission

Referent: Prof. Dr. Hans-Christian Hofsäss, II. physikalisches Institut, Universität
Göttingen

Koreferent: Prof. Dr. Tim Salditt, Institut für Röntgenphysik, Universität Göttingen

weitere Mitglieder der Prüfungskommission

Prof. Dr. Jörg Enderlein, III. physikalisches Institut, Universität Göttingen

Prof. Dr. Ariane Frey, II. physikalisches Institut, Universität Göttingen

Prof. Dr. Sarah Köster, Institut für Röntgenphysik, Universität Göttingen

Prof. Dr. Claus Ropers, IV. physikalisches Institut, Universität Göttingen

Tag der mündlichen Prüfung: 31.10.2016

Contents

Abstract	III
List of Abbreviations	V
List of Symbols	VI
1 Introduction	1
2 Fundamentals	3
2.1 Stopping power	3
2.2 Bethe–Bloch theory	6
2.3 Inverted Doppler–shift attenuation	9
3 Experimental set–up	15
3.1 Detector	15
3.1.1 Photon processes	15
3.1.2 Detection of photons	20
3.1.3 HPGe–detector	22
3.2 Data acquisition	24
3.3 Energy calibration	27
3.4 Target	28
3.4.1 Vacuum target	28
3.4.2 Water target	29
3.4.3 Entrance window	30
3.4.4 Carbon layer	35
3.5 Target moving system	36
3.6 Electronics	37
3.7 Software	42
4 Measurement	45
4.1 Unattenuated γ –energy spectra	45
4.2 Attenuated γ –energy spectra	48
4.3 Durability of the carbon layer	51
5 Instrumentation effects	55
5.1 Background correction	55
5.2 System response function	56
5.3 Angular resolution	59

6	Data evaluation	61
6.1	Experimental unattenuated γ -energy spectra	61
6.2	Experimental attenuated γ -energy spectra	62
6.3	Deconvolution	63
7	Results and discussion	67
7.1	Stopping power	67
7.2	Uncertainty analysis	70
7.3	Discussion	78
7.4	Impact on radiation therapy	86
8	Conclusion and outlook	89
A	Kinematics of the scattering processes	99
B	Angular resolution	101
C	Angular correlation	107
C.1	Angular distribution of $^{12}\text{C}^*$ projectiles in the centre of mass system	107
C.2	Energy levels of the compound nucleus	108
C.3	Comparison and results	111
	Acknowledgement	117

Abstract

Cancer therapy using carbon ions has gained increasing interest in the last decade due to its advantageous dose distributions. For the dosimetry and treatment planning, the accurate knowledge of the stopping power of water for carbon ions is of crucial importance. In the high energy region, the stopping power can be calculated rather accurately by means of the Bethe–Bloch formula. In the case of projectile velocities comparable to those of the valence electrons of the target, these calculations are subject to large uncertainties.

There exist no experimental data for the stopping power of water for projectile energies prevailing in the so-called Bragg peak region. The currently available stopping power data for water are derived from measurements in water vapour or D₂O ice and, hence, neglect the dependence on the state of aggregation. The stopping power of water for charged particles is of high interest not only for practical applications but also to consider how physical and chemical state of the target influence the collisional energy transfer.

For the measurement of the stopping power of water, the inverted Doppler-shift attenuation method was used in this work. This method has the advantage that the projectile itself is not needed to be detected and can be slowed down entirely in the target. In this method, the stopping power is determined from the Doppler-shift of the γ -quanta emitted by projectiles during their slow down. This experiment can be performed at atmospheric pressure and consequently, the stopping power of water can be measured in its real physiological condition.

In this work, the stopping power of water for carbon ions was measured for the first time in the energy range between 1 MeV and 6 MeV covering the kinetic energies of carbon ions in the Bragg peak region. The experimental method is presented in detail along with the design of the apparatus and of the data acquisition system.

A comprehensive analysis of instrumental effects influencing the experimental results was performed. The overall relative uncertainty of the present data amounts to 11.9%. Within the uncertainty, the measured data is consistent with the stopping power predicted by MSTAR [68], CASP [82] and the recommendation of the ICRU report 73 errata [91]. The data predicted by SRIM2013 [99] and ICRU report 73 [11] appear to be higher by 13% in average.

List of Abbreviations

ADC	Analogue digital converter
CU	Central unit
DC	Direct current
DLC	Diamond-like carbon
DPHA	Digital pulse height analysis
FET	Field effect transistor
HPGe	High purity germanium
HV	High voltage
IC	Integrated circuit
IDSAM	Inverted Doppler-shift attenuation method
LET	Linear energy transfer
MCU	Motor control unit
μ C	Micro controller
OP	Operational amplifier
PCI	Peripheral components interconnected
PS	Power section
PTV	Planning target volume
PWM	Pulse width modulation
Smp	Sample(s)
UART	Universal asynchronous receiver transmitter bridge
USB	Universal serial bus

List of Symbols

A_p	Mass number of the projectile
A_t	Mass number of the target atom
c	Speed of light
d	Depth in absorber
$d\tilde{N}_u/dE_\gamma$	Measured unattenuated γ -energy spectrum
dN_u/dE_γ	Unfolded unattenuated γ -energy spectrum
$d\tilde{N}_a/dE_\gamma$	Measured attenuated γ -energy spectrum
dN_a/dE_γ	Unfolded attenuated γ -energy spectrum
E_γ	measured γ -energy
ϵ	Complex dielectric response function
η_F	Radially dependent detection efficiency of the detector
$FWHM$	Full width at half maximum
\hbar	Reduced Planck constant
$\langle I \rangle$	Mean excitation energy
$\underline{\underline{\Lambda}}$	Covariance matrix
L_Δ	Restricted LET
m	Mass of carbon nucleus
m_e	Electron mass
$\underline{\underline{M}}_A$	Matrix representation of energy resolution
$\underline{\underline{M}}_B$	Matrix representation of the γ -energy spread in unattenuated γ -energy spectrum arising due to the finite detector solid angle
$\underline{\underline{M}}_C$	Matrix representation of the γ -energy spread in attenuated γ -energy spectrum arising due to the finite detector solid angle
μ/ρ	Mass attenuation coefficient
μ	Total linear attenuation coefficient
μ_{Cs}	Linear attenuation coefficient due to Compton scattering
μ_{pe}	Linear attenuation coefficient due to photoelectric absorption
μ_{pp}	Linear attenuation coefficient due to pair production

N_A	Avogadro number
φ	Emission angle of the Doppler-shifted γ -quanta
\underline{q}	Momentum transfer
S	Stopping power
r_e	Classical electron radius
ρ_t	Density of the target
$\sigma_a(E_{\gamma,i})$	Total uncertainty of channel i in attenuated γ -energy spectrum
$\sigma_u(E_{\gamma,i})$	Total uncertainty of channel i in unattenuated γ -energy spectrum
T	Kinetic energy of the projectile
τ	Mean lifetime of the first excited state of ^{12}C
ϑ	Flight-angle of excited carbon nucleus
u	Atomic mass unit
v	Velocity of the projectile (carbon ion)
Var_1	Variance due to deconvolution
Var_2	Variance due to uncertainty of energy resolution function
Var_3	Variance due to background subtraction
$W(v_0)$	Initial velocity distribution of excited carbon nuclei
\underline{x}_a	Vectorial representation of true attenuated γ -energy spectrum
\underline{x}_u	Vectorial representation of true unattenuated γ -energy spectrum
\underline{y}_a	Vectorial representation of measured attenuated γ -energy spectrum
\underline{y}_u	Vectorial representation of measured unattenuated γ -energy spectrum
Z	Nuclear charge of the projectile
Z_{eff}	Mean charge of the projectile
Z_t	Atomic number of the target atoms

Chapter 1

Introduction

In radiation therapy using heavy particles such as carbon ions, the main benefit comes from the locally well-defined dose distribution. At a certain depth, ions with a distinct initial energy will cause a sharply defined dose deposition: the Bragg peak. The aim in radiation therapy is to maximise the dose deposition in the planning target volume (PTV). To achieve this, the beam energy is tuned, so that the ions in the PTV reach an energy at which the stopping power reaches the maximum. Additionally, not only the major increase in dose in the PTV is decisive but also the relative biological effectiveness (RBE). This quantity is dependent on the so-called linear energy transfer (LET), which is equal to the stopping power in the case of its unrestricted representation.

In the pre-PTV region, the energy loss per length can be calculated rather accurately by means of the Bethe-Bloch theory. However, for the biologically most relevant region, the Bragg peak, there exist no theoretical models enabling accurate calculation of the stopping power for ions.

The experimental determination of the stopping power in the Bragg peak region using traditional transmission methods are not feasible for water. The existing data stem from measurements of the stopping power of water vapour or D₂O ice and, hence, neglect the dependence of the stopping power on the state of aggregation. Experiments carried out by Siiskonen *et al.* [92] for the stopping power of liquid water for protons in the energy range 4.7 MeV – 15.2 MeV and Shimizu *et al.* [88, 87] for protons with energies down to 0.3 MeV were initiated by upcoming interest for the stopping power in energy regions in the vicinity of the stopping power maximum. However, it has to be mentioned that these data also do not contain the energy region in which the maximum of the stopping power occurs and refer only to light charged particles such as protons.

There still exists confusion concerning the difference between the stopping cross section of water and water vapour. The actual available data sets are neither consistent in absolute values nor agree in the sign of the aggregation effects.

A measurement of the stopping power of water for carbon ions in the energy region around the maximum of the stopping power can provide a great step towards clarification.

It would also help improve treatment planning, as stopping power influences the dose distribution at the distal end of the beam where healthy tissue may acquire higher doses than prescribed. It would also provide a database for benchmarking other quantities such as the mean charge state of the projectile in dependence of its energy, the mean excitation energy and the dependence of the stopping power on the state of aggregation. As the latter two are properties of the target, they can also be applied to radiation therapy using other charged particles such as protons or oxygen.

The inverted Doppler–shift attenuation method provides a great tool for precise measurement of the stopping power of water for carbon ions in the intermediate energy range as there is no need for detecting the projectile itself. Here, the stopping power is determined by measuring the Doppler–shift of γ -quanta that have high penetrability.

In this work, the experimental set up and the methodological base for the measurement of the stopping power of water for carbon ions with energies in the Bragg peak region using the inverted Doppler–shift attenuation method will be developed. Furthermore, the experimental effects influencing the experiment and its results will be discussed and regarded in a detailed analysis of the uncertainty. The experimental data obtained will be discussed and compared to previously available data.

This work closes with an outlook how the accuracy of the measurement can be increased.

Chapter 2

Fundamentals

This chapter explains the physical meaning of the stopping power and its related quantities that play an important role in clinical dosimetry. Subsequently, the Bethe–Bloch theory, which provides the basic formula for the calculation of the stopping power, is described. This involves a discussion of the mean excitation energy, as it is an essential quantity in the Bethe–Bloch formula.

The limits of the Bethe–Bloch theory and the experimental difficulties in measuring the stopping power in the vicinity of the Bragg peak will be outlined, and the advantage of the inverted Doppler–shift attenuation method (IDSAM) applied in the present work will be described.

The chapter closes with a derivation of the measurement equation used for the determination of the stopping power from the Doppler–shifted γ –energy spectrum.

2.1 Stopping power

Charged particles traversing a medium lose their energy by interaction predominately with the electrons of the material. The ability of the target medium to slow down the moving particles is expressed by the stopping power S , which is defined as the energy loss per length:

$$S = -\frac{dT}{dx}. \quad (2.1)$$

At energies above 1.5 keV/u , the contributing interaction processes are mainly inelastic collisions of the projectile with the target medium. The projectile loses its kinetic energy due to momentum transfer to the electrons of the medium, leading to an excitation or ionisation of the target atoms or molecules. This kind of energy loss is described by the electronic stopping power S_e . Below energies of about 1.5 keV/u , the energy loss of the projectile predominately occurs through elastic collisions with the atoms or molecules of the traversed medium which is described by the nuclear stopping power S_n . The sum of

these two contributions gives the collisional stopping power

$$S_c = S_e + S_n. \quad (2.2)$$

Charged particles can additionally lose their kinetic energy by emission of bremsstrahlung in the electric field of the target nuclei. This energy loss is described by the radiative stopping power S_r . The total stopping power S can then be written as the sum of S_c and S_r :

$$S = S_c + S_r. \quad (2.3)$$

It is related to the stopping cross section S_σ via

$$S_\sigma = \frac{V}{N} S \quad (2.4)$$

with the number of atoms or molecules N in a volume V . As the radiative stopping only occurs at very high projectile energies, it will be not further considered in this work.

The stopping power does not only depend on the physical properties of the target, such as its electronic structure and density, but also on the mass and charge of the projectile. Furthermore, the stopping power is a function of the kinetic energy of the projectile. An example of the dependence of the components of the collisional stopping power on the kinetic energy T is given in figure 2.1. When coming from the high-energy side, the stopping power increases with decreasing projectile energy T until it reaches its maximal value at energies around 300 keV/u . At the left hand side of the maximum, the stopping power shows a steep decrease with decreasing projectile kinetic energy. The energy of a projectile with an incident energy of T_0 in a certain depth d of the traversed medium can be calculated by

$$T(d) = T_0 - \int_{x=0}^{x=d} S(T(x')) dx'. \quad (2.5)$$

Figure 2.1(b) shows the stopping power of water for carbon ions with an initial energy of $T_0 = 1.3 \text{ GeV}$ as function of the penetration depth d calculated using equation 2.5. The stopping power data used for the calculation, shown in figure 2.1(a) were taken from SRIM2013 [99]. At the end of the projectile range a sharp maximum is built up which is called Bragg peak. Its location in depth depends on the initial energy of the projectiles as well as on the stopping power of the target medium.

In principle, the stopping power can be determined by transmitting projectiles with known energy T through a thin slice of material with a definite thickness dx and then measuring their final energy (see also figure 2.2). This transmission method is, however, limited to those materials which are thin enough to enable a differential measurement and at the same time are stable in an evacuated environment. The maximal thickness of the target that can be accepted for a transmission measurement can be estimated according

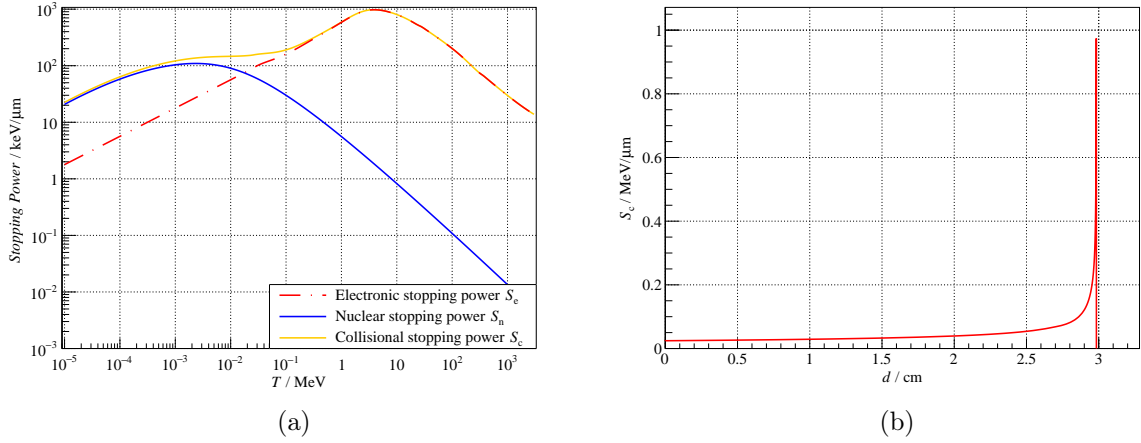


Figure 2.1: (a) Stopping power of carbon ions in water calculated with SRIM2013[99]. (b) Stopping power as function of the depth in water for carbon ions with a starting energy of 1.3 GeV.

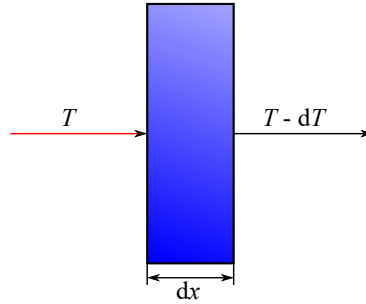


Figure 2.2: Illustration of the transmission method for the measurement of the stopping power.

to the average residual range R of the projectiles:

$$R(T_0) = - \int_{T_0}^{T=0} \frac{1}{S(T')} dT' . \quad (2.6)$$

Figure 2.3 shows the average residual range of carbon projectiles in water in dependence on their initial kinetic energy T calculated using equation 2.6. As it can be seen from figure 2.3, the residual range of projectiles is rather small in the vicinity of the Bragg peak area.

In the case of water, this measurement has to be performed at atmospheric pressure. This is necessary to prevent a variation of the target thickness during the measurement and the slow down of the projectiles in the evaporated water. Consequently, the target must be sealed against the vacuum of the beam line. If the primary particles are not available from a radioactive source as in the case for protons or carbon ions, the projectiles have to be produced by an accelerator with an evacuated beam line. The entrance window of the target sealing against the beam line must have a mechanical strength to withstand the pressure difference between the atmosphere and the vacuum. Usually, this mechanical strength requires a window thickness in the same order as the range of the incident

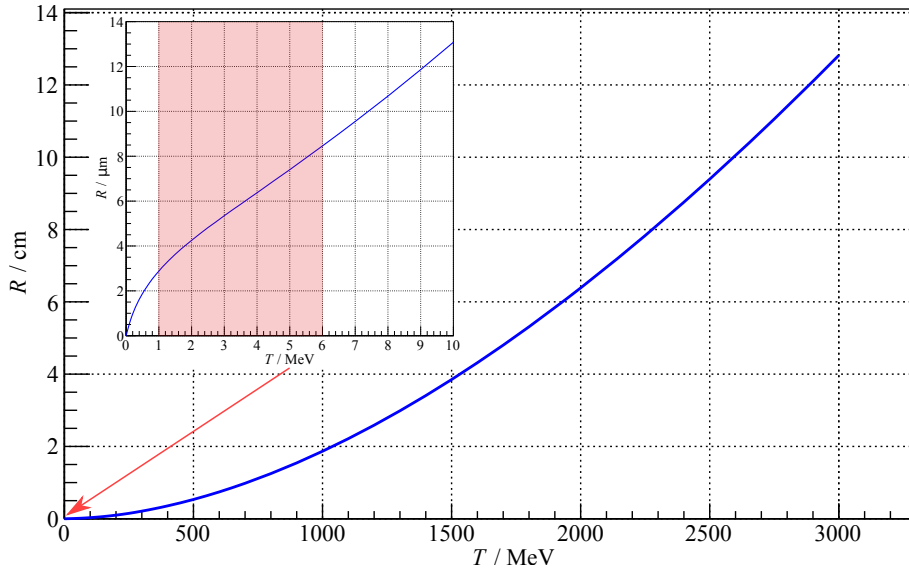


Figure 2.3: Residual range of carbon ions stopped in water in dependence on the kinetic energy. The marked region covers the energy interval in which the stopping power reaches the maximal value.

projectiles. Therefore, the application of the transmission method for the measurement of the stopping power of water for projectile energies of a few hundred keV/u is not feasible.

As mentioned above, the stopping power only describes the energy loss of a projectile per length. In the field of dosimetry of ionising radiation, the term Linear Energy Transfer (LET) is commonly used. It describes the energy transfer to the medium per path length. The LET is defined as

$$L_{\Delta} = \frac{dT_{\Delta}}{dx} \quad \text{and} \quad \lim_{\Delta \rightarrow \infty} L_{\Delta}(T) = S_c(T). \quad (2.7)$$

It gives the energy transfer up to energies of Δ . In the limit of $\Delta = \infty$ the LET and stopping power are equal.

Radiobiological experiments indicate that the LET is correlated to the relative biological effectiveness (RBE) of ionising radiation [23]. It has to be mentioned that RBE not only depends on the projectile and the LET but also on the fractionation of the irradiation, the cell type and cell cycle, the environment and oxygen saturation, and so on. However, it can be assumed that the radiation damage increases with the LET due to the larger amount of energy deposited along the same length. For the quantification of the radiation damage in case of treatment planning, the stopping power of the projectiles at all depths in the healthy tissue and malignant neoplasm (cancer) has to be known.

2.2 Bethe–Bloch theory

The calculation of the stopping power is commonly based on Bethe–Bloch theory [6]. At a kinetic energy at which the ion has lost all its electrons, the stopping power S can be

calculated using the relativistic Bethe–Bloch theory [51]:

$$\frac{dT}{dx} = -\tilde{S}\rho\frac{Z_t}{A_t}\frac{Z^2}{\beta^2}\left[\ln\left(\frac{2m_e}{1-\beta^2}v^2\frac{W_{\max}}{\langle I \rangle^2}\right) - 2\beta^2 - \delta - 2\frac{C_s}{Z_t}\right] \quad (2.8)$$

The constants \tilde{S} is given by [45]:

$$\tilde{S} = 4\pi r_e^2 m_e c^2 u^{-1} = 0.307075 \text{ MeVcm}^2/\text{g} \quad (2.9)$$

The quantity W_{\max} represents the maximum energy transfer from the projectile with the velocity $\beta = v/c$ to the target electrons

$$W_{\max} = \frac{2m_e c^2 \beta^2}{(1-\beta^2)\left(1 + 2\frac{m_e}{m_p}\sqrt{1 + \frac{\beta^2}{1-\beta^2}} + \left(\frac{m_e}{m_p}\right)^2\right)}. \quad (2.10)$$

In the case of projectiles with a mass much larger than the electron mass m_e , as in the case of ions, W_{\max} can be approximated by:

$$W_{\max} \sim 2m_e c^2 \frac{\beta^2}{1-\beta^2} \quad (2.11)$$

The term δ is the correction of the density effect. As a charged particle passes an atom, its electrical field induces polarisation in the target atom or molecule. This leads to a screening of the electric field of the projectile, leading to a reduced interaction strength between the collision partners. Without the density correction, the Bethe–Bloch formula would overestimate the stopping power at high projectile energies. This effect strongly depends on the mass density, more accurately on the electron density of the traversed medium.

In general, the Bethe–Bloch formula is valid if the average velocity of the valence electrons of the traversed medium is much smaller than the projectile velocity. If the velocity of the projectile approaches that of the target valence electrons, the different response of electrons in the different atomic shells to the electric field of the projectile has to be taken into account. This is handled by introducing an additional term, called shell correction C_s , in the Bethe–Bloch formula. However, despite the shell correction, the Bethe–Bloch theory cannot provide an accurate calculation for projectile velocities below $\approx 5\%$ of the speed of light as it only corrects for the atomic binding of the electrons but not for complex charge exchange processes which become dominant in the low energy regime [9].

The most important quantity in the Bethe–Bloch formula is the mean excitation energy $\langle I \rangle$, which depends on the electronic structure of the target. It is noteworthy that not only the Bethe–Bloch formula itself, but also the applied corrections depend on the mean

excitation energy. In case of discrete transitions, the mean excitation energy can be obtained from the oscillator strength f_n and the corresponding transition energy E_n [100].

$$\ln \langle I \rangle = \sum_n f_n \ln E_n \quad (2.12)$$

The sum of oscillator strength f_n fulfils the *Thomas–Reiche–Kuhn–sum* [27]. The oscillator strength describes the transition of a particle with mass m_0 , in this case the mass of an electron, from one state $|m\rangle$ into other states $|n\rangle$:

$$f_{n \rightarrow m} = \frac{2m_0}{\hbar^2} \sum_n \Delta E |\langle n | \hat{x} | m \rangle|^2 . \quad (2.13)$$

ΔE describes the difference of energy of the states $|m\rangle$ and $|n\rangle$. The term \hat{x} is the dipole transition operator. Generally, the calculation of the mean excitation energy $\langle I \rangle$ is hampered by the lack of the data for the oscillator strengths of the target. Fortunately, Fano [32, 63] presented a simple relation between the mean excitation energy and the dielectric property of the target:

$$\langle I \rangle = \frac{2}{\pi \omega_P^2} \int_0^\infty \omega_P \Im \left[-\frac{1}{\epsilon(\underline{q}, \omega)} \right] \ln(\hbar\omega) d\omega \quad (2.14)$$

where ω_P denotes the plasma frequency and ϵ is the complex dielectric response function which is given by:

$$\epsilon(\underline{q}, \omega) = \epsilon_1(\underline{q}, \omega) + \imath \epsilon_2(\underline{q}, \omega) , \quad (2.15)$$

with the imaginary unit \imath and the momentum transfer \underline{q} . The dielectric response function of water has been measured by Hayashi *et al.* [40, 39] using small-angle inelastic X-ray scattering (IXS) experiments.

Literature values for $\langle I \rangle$ are often derived from measurements of the stopping power and semi-empirical equations, where $\langle I \rangle$ is regarded as being dependent on the atomic number Z_t [45]:

$$\frac{\langle I \rangle}{Z_t} = \begin{cases} \left(12 + \frac{7}{Z_t} \right) \text{ eV} & \text{for } Z_t < 13 \\ (9.77 + 58.8 Z_t^{-1.19}) \text{ eV} & \text{for } Z_t \geq 13 \end{cases} \quad (2.16)$$

The stopping power is not only influenced by the mean excitation energy but also by the charge state of the projectile. In general, the Bethe–Bloch formula assumes a fully ionised projectile which is only valid for high projectile energies. The formalism of using an effective charge goes back to an idea of Bohr [15] and was formalised by Northcliffe [61]. However, Ziegler [100] interprets and handles the effective charge as an additional fit parameter for the circumstance that the Bethe–Bloch theory is used

at lower energies. Brandt and Kitagawa [16] have developed a theoretical approach to determine the charge state of the projectile. However, at projectile velocities where the stopping power approaches its maximum, the charge state is not uniquely defined so that the stopping power in this energy regime cannot be described by one closed model.

Beside the shell and density correction, there are further corrections which take additional effects like higher order quantum electrodynamic processes or ultra relativistic velocities into account. Usually, the contribution of these effects to the stopping power is less than 1 % and is only relevant in the high energy range.

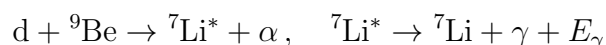
Concerning projectile energies below 0.1 MeV/u , the dependence of the stopping power is given by the Lindhard–Scharff–Schiott theory, where the interaction of projectile and target is described as quasi-elastic collisions [53]. In this theory, the stopping is described by a Thomas–Fermi type formula for the electronic stopping which was combined with an approximated universal differential scattering cross section which was derived in the work of Lindhard *et al.* by using the extrapolated perturbation method for classical scattering [53].

2.3 Inverted Doppler-shift attenuation

This section explains the principle and the mathematical formalism of the inverted Doppler-shift attenuation method (IDSAM) developed by Neuwirth *et al.* [59] and used by Baek *et al.* for the measurement of the energy loss of ^{12}C projectiles in different carbon modifications [4].

As mentioned above, the measurement of the stopping power of liquid water by means of traditional transmission experiments, in which the particle of interest traverses a thin slice of a material, is not feasible for low energies.

This difficulty can be avoided by applying an indirect method such as the IDSAM. It provides the advantage that the projectile does not have to leave the target material, as the projectile itself does not need to be detected. The origin of the IDSAM goes back to the 1950s, where Rasmussen *et al.* [72] observed a broadening in the γ -lines gathered from the bombardment of a beryllium target with deuterium. This bombardment leads to a nuclear reaction producing ^7Li in the first excited state via:



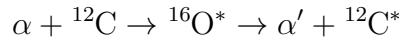
with an energy of $E_\gamma = 0.477 \text{ MeV}$. The Doppler broadening of γ -lines was used by Devons *et al.* [25] to determine the lifetime of the γ -transition. Great progress in this method was made by the availability of high purity germanium detectors which are able to detect γ -quanta with a high energy resolution. Today, the Doppler-shift attenuation method (DSAM) is a suitable tool for determination of lifetimes in the order of fs up to a few ps.

The idea behind the inversion of the DSAM is the determination of the stopping power from the known lifetime of the excited state of the projectile [59].

As shown below, the stopping power of a projectile can be expressed as the temporal change of its velocity times its mass:

$$\begin{aligned} S &= -\frac{dT}{dx}, \quad \text{with} \quad T = \frac{1}{2}mv^2 \\ &= -\frac{1}{2}m \frac{dv^2}{dx} = -mv \frac{dv}{dx} = -mv \frac{dv}{dt} \frac{dt}{dx} = -mv \frac{dv}{dt} \frac{1}{v} \\ &= -m\dot{v} \end{aligned} \quad (2.17)$$

and has the dimension of a force. The (mass) stopping power of a projectile can therefore be determined by a measurement of the projectile velocity as a function of time. In the IDSAM, the projectile velocity is monitored by means of the Doppler-shift of the γ -quanta emitted during the de-excitation of the projectile, while the information on the time elapsed since the production of the excited projectile is obtained from the exponential decay law. In this work, the excited projectiles are carbon nuclei in their first excited state with an energy of $E(|2^+)) = 4.4389 \text{ MeV}$. These are produced by means of the nuclear reaction



and decay by the exponential decay law

$$N(t) = N_0 e^{-\frac{t}{\tau}}. \quad (2.18)$$

$N(t)$ is the number of excited nuclei at time t , N_0 is the number of excited nuclei at time $t = 0$, and τ is the lifetime of the first excited state in carbon, $\tau({}^{12}\text{C}^*) = 61 \text{ fs}$. In the laboratory frame, the carbon nucleus is not at rest so that the frequency of the emitted electromagnetic radiation and, hence, the energy is modified by the Doppler effect:

$$E_{\gamma}(\beta, \varphi) = E_0 \frac{\sqrt{1 - \beta^2}}{1 - \beta \cos \varphi}, \quad \text{where} \quad \beta = \frac{v}{c}. \quad (2.19)$$

The energy of the γ -quantum depends on the velocity v of the carbon nucleus in the laboratory frame at the moment of the γ -emission as well as on the emission angle φ of the γ -quantum relative to the moving direction of the carbon nucleus and can be described by equation 2.19 [18] (see also figure 2.4). In the rest frame of the decaying nucleus, the γ -energy is the energetic difference $E_0 = 4.439 \text{ MeV}$ [33] of the first excited and the ground state of the nucleus. If the experiment is arranged such that the flight angle of the carbon nucleus relative to the axis of the incoming α -projectile and the emission angle of the detected γ -quantum are equal ($\varphi = \vartheta$), the Doppler-shifted γ -energy E_{γ} is determined by the velocity of the carbon nucleus and its flight angle ϑ . This relation is

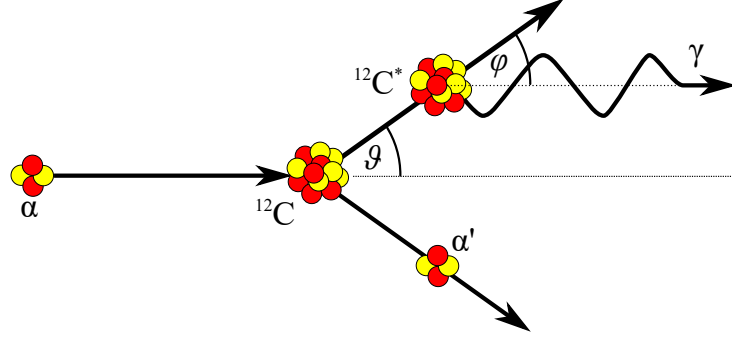


Figure 2.4: Sketch of the reaction used to produce $^{12}\text{C}^*$ projectiles.

shown in figure 2.5 and its explicit derivation is given in appendix A.

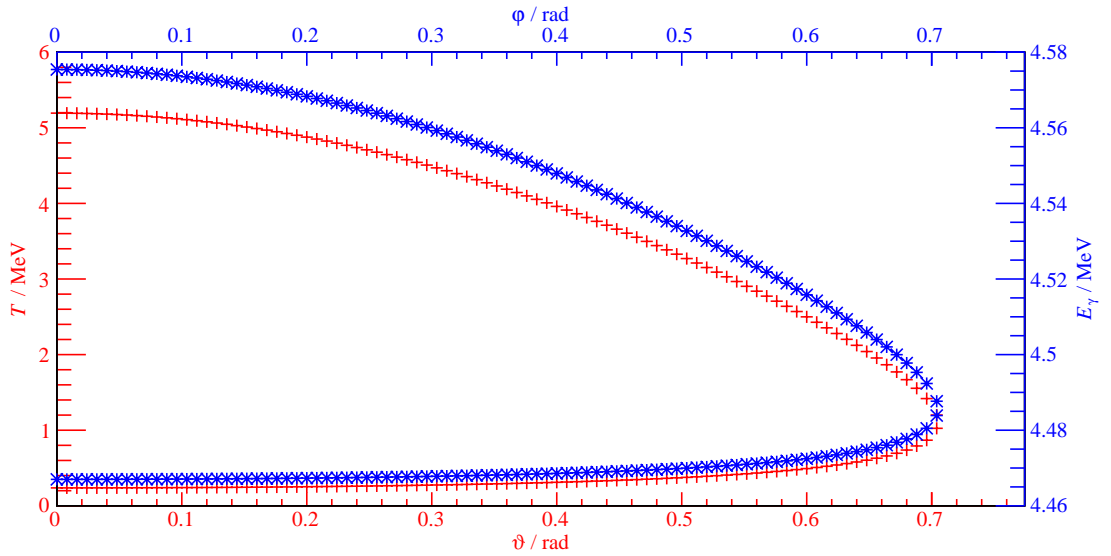


Figure 2.5: Kinetic energy T (+) of the excited carbon ion and the Doppler-shifted γ -energy E_γ (*) as function of the flight angle ϑ . The calculation was carried out for an α -particle energy of 10.2 MeV and $\varphi = \vartheta$ using equations A.7 and 2.19.

In the case that the back scattered α -particle is detected in coincidence at a certain angle, the kinematics is entirely characterised and only $^{12}\text{C}^*$ projectiles with a fixed start velocity and the corresponding flight angle are taken into account. If the carbon nuclei were slowed down during their decay, the initial velocity spectrum changes. The degree of the change depends on the stopping power of the target. The velocity spectrum of the slowing down carbon nuclei can be written as:

$$\frac{dN}{dv} = \frac{dN}{dt} \frac{dt}{dv} \quad \text{with} \quad \frac{dN}{dt} = -N_0 \frac{1}{\tau} e^{-\frac{t}{\tau}}. \quad (2.20)$$

Equation 2.20 can be interpreted as the product of the count rate \dot{N} derived from the decay law and the reciprocal of the deceleration $1/v$. The count rate of γ -quanta depends on the mean lifetime of the excited state τ and the time elapsed t . The decay law provides an intrinsic stopwatch to the method.

The stopping power expressed by equation 2.17 can be used to calculate the time elapsed from the production of an excited carbon nucleus with initial velocity v_0 until its decay at the velocity v :

$$t(v) = \int_v^{v_0} \frac{m}{S(v')} dv'. \quad (2.21)$$

This expression can be substituted into equation 2.20, giving

$$\frac{dN}{dv} = N_0 \exp \left[- \int_v^{v_0} \frac{m}{\tau S(v')} dv' \right] \frac{m}{\tau S(v)}. \quad (2.22)$$

Equation 2.22 describes the number of excited carbon nuclei which decay in the velocity interval $[v, v + dv]$. The transformation from the velocity spectrum to the γ -energy spectrum can be done according to

$$\frac{dN}{dE_\gamma} = \frac{dN}{dv} \frac{dv}{dE_\gamma}. \quad (2.23)$$

The derivative $\frac{dv}{dE_\gamma}(\vartheta, v)$ can be obtained from Doppler formula 2.19 with $dv = d\beta c$. The resulting Doppler-shifted γ -energy spectrum for one starting velocity v_0 can then be written as:

$$\frac{dN_a}{dE_\gamma}(v_0) = N_0 \exp \left[- \int_v^{v_0} \frac{m}{\tau S(v')} dv' \right] \frac{m}{\tau S(v)} c \frac{d\beta}{dE_\gamma}(\vartheta, v). \quad (2.24)$$

If the γ -quanta are not measured in coincidence with the α -particles, the full spectrum of start velocities has to be considered. This can be expressed as a superposition of equation 2.24 with the start velocity spectrum $W(v_0)$ of the excited carbon nuclei:

$$\frac{dN_a}{dE_\gamma} = \int_{v_{\min}}^{v_{\max}} N_0 \exp \left[- \int_v^{v_0} \frac{m}{\tau S(v')} dv' \right] \frac{m}{\tau S(v)} c \frac{d\beta}{dE_\gamma}(\vartheta, v) W(v_0) dv_0. \quad (2.25)$$

The spectrum described by equation 2.25 is called **attenuated γ -energy spectrum** in this work.

The start velocity distribution $W(v_0)$ can be obtained by measuring the Doppler-shifted γ -energy spectrum of carbon ions at their initial velocity. This can be achieved by letting the $^{12}\text{C}^*$ projectiles decay in vacuum. The result dN_u/dE_γ of this measurement is associated with the start velocity distribution by:

$$\frac{dN_u}{dE_\gamma} = \frac{dN_u}{dv_0} \frac{dv_0}{dE_\gamma} = W(v_0) \frac{dv_0}{dE_\gamma} \quad (2.26)$$

and is called the **unattenuated γ -energy spectrum**. The derivative dv_0/dE_γ can be obtained from Doppler equation 2.19 and the kinematics of the nuclear reaction.

It should be noted that the IDSAM requires an appropriate lifetime of the excited state of the nuclei. If the lifetime is very long, most of the nuclei will decay after they have been completely stopped, providing no significant dependence of the γ -energy spectra on the projectile velocity. On the other hand it has to be long enough to cover a major part of the stopping time.

Chapter 3

Experimental set-up

The experimental set-up for recording the Doppler-shifted γ -energy distributions and its components will be described. For this purpose, the principles of γ -detection with different types of detectors and their selection criteria will be explained.

The data acquisition system, consisting of the commercially available hardware and the self-developed software, will be outlined including the description of the energy calibration and important experimental parameters.

Finally, the design and development of the carbon layer and water target system used to produce and slow down $^{12}\text{C}^*$ projectiles, respectively, is described with the special focus onto the selection of materials for the target housing to minimise neutron and γ -quanta background.

3.1 Detector

3.1.1 Photon processes

Photons traversing a material layer with the thickness d are attenuated by means of an exponential function:

$$N_\gamma = N_{\gamma,0}e^{-\mu d} \quad (3.1)$$

where $N_{\gamma,0}$ is the number of incident photons and μ it the total linear attenuation coefficient. This attenuation is due to interaction of the photons with the atoms in the traversed medium where the following three processes occur:

- photoelectric absorption,
- Compton scattering,
- pair production.

The total linear attenuation coefficient μ in equation 3.1 is a measure for the total photon interaction cross section and is the sum of the attenuation coefficient for photoelectric

absorption μ_{pe} , Compton scattering μ_{Cs} and pair production μ_{pp} :

$$\mu = \mu_{\text{pe}} + \mu_{\text{Cs}} + \mu_{\text{pp}} \quad (3.2)$$

and is mostly represented as the *mass attenuation coefficient* which is the linear attenuation coefficient normalised by the density of the absorber μ/ρ , where ρ is the mass density. Figure 3.1 shows the linear mass attenuation coefficients μ/ρ of germanium for the interactions described above in dependence on the γ -energy E_γ .

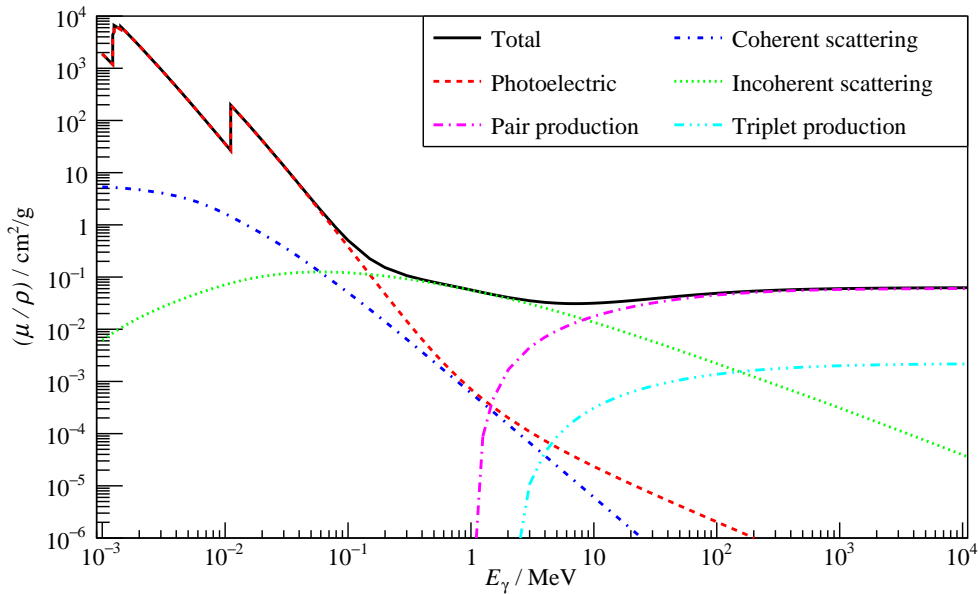


Figure 3.1: Mass attenuation coefficients as function of the photon energy E_γ for germanium.

Photoelectric absorption describes the process where the photon is fully absorbed and predominantly one of the inner atomic shells is ionised. The kinetic energy of the released electron is given by:

$$T_e = E_\gamma - E_b - q \quad (3.3)$$

where E_γ is the energy of the incident photon, E_b is the binding energy, and q is the energy transferred to the nucleus which in general is negligible as the mass of the nucleus is much larger than the electron mass. The vacancy is then filled by an electron of higher shells. The energy difference of both shells is emitted as characteristic X-ray radiation. Alternatively, a radiation free transition can occur by transferring the energy difference to an outer shell electron. This electron is called Auger-electron. The probability of the photoelectric absorption is described by the photoelectric absorption coefficient μ_{pe} which depends on the atomic number Z_t of the absorber and the energy of the photon E_γ .

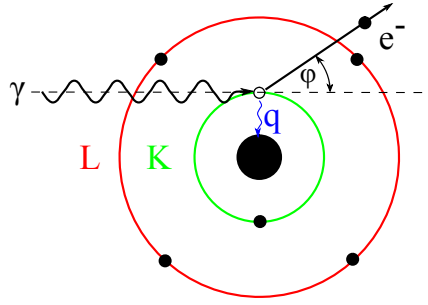


Figure 3.2: Illustration of the photoelectric absorption process.

It and can be approximated by [58]

$$\begin{aligned} \mu_{\text{pe}} &\propto \frac{Z^5}{E_\gamma^{7/2}} & \text{if } E_\gamma > E_B^{(\text{K})} \\ \mu_{\text{pe}} &\propto \frac{Z^5}{E_\gamma} & \text{if } E_\gamma \gg E_B^{(\text{K})} \end{aligned} \quad (3.4)$$

where $E_B^{(\text{K})}$ is the binding energy of the K-shell electrons. The probability sharply increases if the energy of the photon is equal to the binding energy of an atomic shell, leading to characteristic structures called K-edge, L-edge, etc. (see also figure 3.1).

Compton scattering describes the scattering of an incident photon with an electron of the outer shells where the electrons are weakly bound and can be regarded as quasi free. Part of the photon energy is transferred to the electron in form of kinetic energy. The electron energy can be calculated by

$$T_e = E_\gamma - E'_\gamma - E_b, \quad (3.5)$$

where E'_γ is the photon energy after the scattering and E_b is the binding energy of the electron. The energy E'_γ of the Compton-scattered photon depends on the scattering angle ϑ_γ :

$$E'_\gamma = \frac{E_\gamma}{1 + \frac{E_\gamma}{m_e c^2} (1 - \cos \vartheta_\gamma)}, \quad (3.6)$$

where E_γ is the initial energy of the γ -quantum. In contrast to the photoelectric absorption, almost no momentum transfer to the nucleus occurs. The dependence of the linear attenuation coefficient for Compton scattering μ_{Cs} on the absorber material and photon energy can be estimated by

$$\mu_{\text{Cs}} \propto \frac{Z_t}{A E_\gamma^n} \quad \text{where } n = [0.5, \dots, 1] \quad \forall 0.2 \text{ MeV} < E_\gamma < 10 \text{ MeV} \quad (3.7)$$

Pair production: In strong Coulomb fields, like in the vicinity of a nucleus or an electron, the photon energy can be converted into a pair of an electron and its antiparticle, the

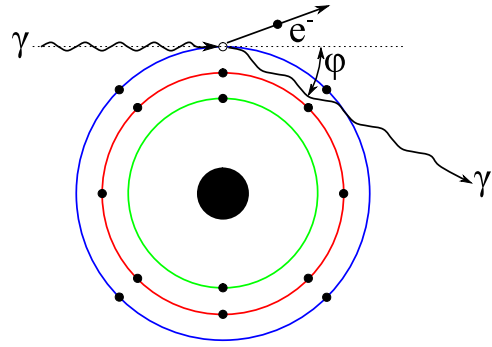


Figure 3.3: Illustration of Compton scattering.

positron (see also figure 3.4). This process is only possible if the photon energy is equal or above the sum of the rest mass of the positron and electron, $E_\gamma \geq 2m_e c^2 = 1022 \text{ keV}$. If its energy is larger than 1022 keV, the residual energy will be distributed among the electron and positron in form of kinetic energies. Due to the conservation of momentum,

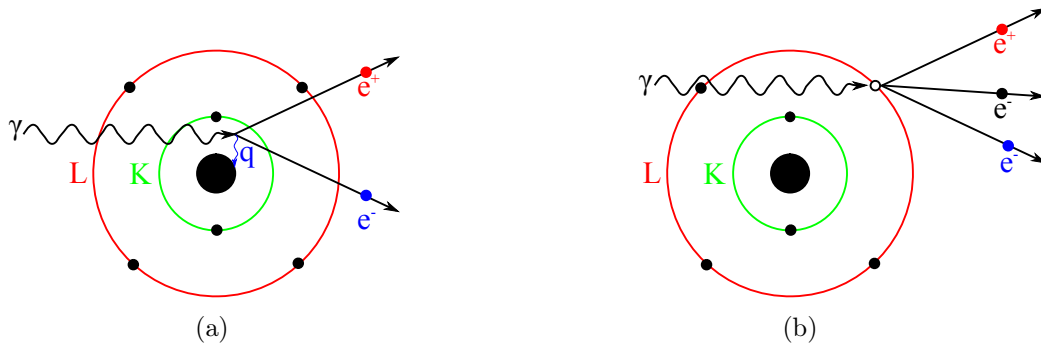


Figure 3.4: (a) Illustration of pair production in the vicinity of a nucleus and (b) pair production in the field of a shell electron (triplet formation).

the nucleus is needed as recoil partner, but in general the recoil momentum is negligible due to its large mass. The attenuation per length by pair production can be estimated by [58]:

$$\mu_{pp} \propto Z_t^2 \ln E_\gamma, \quad \text{with} \quad [E_\gamma] = \text{MeV}. \quad (3.8)$$

Alternatively to pair production in the field of a nucleus, the pair production can also take place in the Coulomb field of a shell electron (see also fig. 3.4(b)). Due to its small mass, the electron will get a high momentum and will leave the atom. As there are three free particles, the electron–positron–pair and the shell–electron participating in the process, it is called triplet production. As in the case of pair production in the field of a nucleus, this process has an energy barrier $E_{\gamma, \text{min}}$ which has to be exceeded. By using the assumption that the bound electron is initially at rest and that all three particles after their production are moving with the same velocity, momentum conservation requires that each of them carries a momentum of $1/3$ of the momentum of the incident photon E_γ/c . Before the interaction, the total energy of the system is given by the energy of the incident

photon and the rest energy of the bound electron. After the reaction, the energy is given by the sum of the energies of the triplet particles. Using the energy–momentum–relation

$$E_{e,0}^2 = E_e^2 - (p_e c)^2. \quad (3.9)$$

with $E_{e,0} = m_e c^2$, energy conservation requires that:

$$E_\gamma + m_e c^2 = \sqrt{9m_e c^2 + E_\gamma^2} \quad (3.10)$$

The solution of equation 3.10 for E_γ gives the minimum γ -energy $E_{\gamma,\min}$ needed for triplet–production:

$$E_{\gamma,\min} \geq 4m_e c^2, \quad (3.11)$$

where $2m_e c^2$ are needed for the production of the electron–positron pair and $2m_e c^2$ are transferred as kinetic energy to the three particles.

Figure 3.5 shows the dependence of the interactions mentioned above on the energy of the γ -quantum as well as on the atomic number of the absorber. In the grey shaded area the photoelectric absorption is the dominant process, the red line indicates the isarithm where $\mu_{pe} = \mu_{Cs}$. Within the yellow shaded area, which is confined by the isarithm of $\mu_{Cs} = \mu_{pp}$ indicated by the blue line, the pair production is the most dominant process. It can be seen from figure 3.5 that in the energy region regarded in this work (around

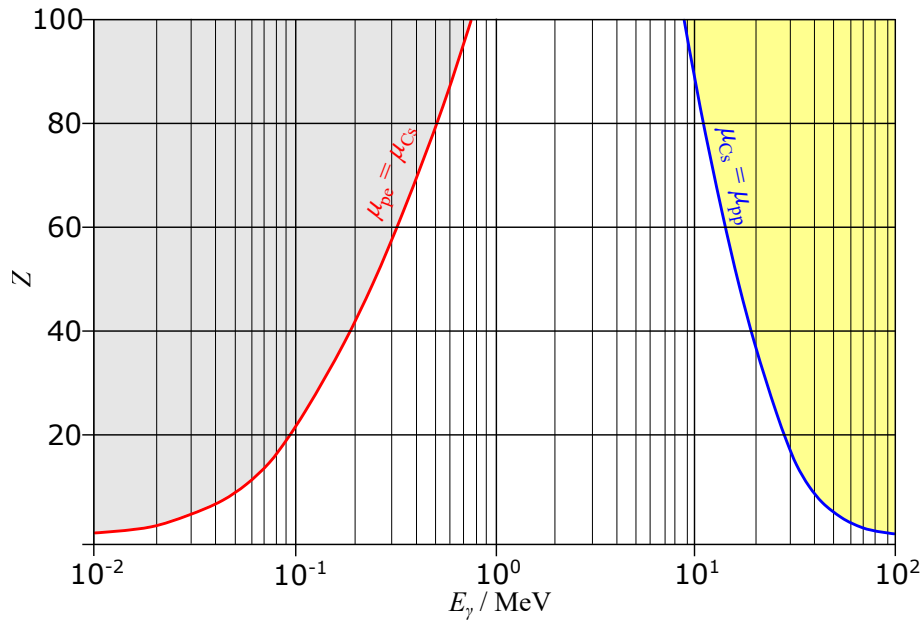


Figure 3.5: Major photon interaction processes in dependence of the photon energy E_γ and the atomic number of the absorbing material. In the grey shaded region, the photoelectric absorption is the most common interaction. The red line connects the points with the same probability for the photoelectric absorption and the Compton scattering. In the white region, the Compton scattering is the dominant process. The points with equal probability for Compton scattering and pair production are represented by the blue line. Pair production becomes the dominant process in the yellow area.

4.4 MeV) the most dominant process is Compton scattering which is indicated by the blank area.

3.1.2 Detection of photons

The principle of the detection of electromagnetic radiation is the conversion of the energy of the primary radiation into a number of charges which can be measured. These charges are produced in the interactions of the electrons released in photoelectric absorption, Compton scattering or the electrons and positrons released by the pair production. These secondary particles perform ionisation within the detector material until they have deposited nearly their complete kinetic energy. When the positron comes to rest, it couples with an electron of the medium and forms a positronium which annihilates and emits two photons with an energy of $E_A = 511$ keV. These two photons are sent out diametrical if the positronium was completely at rest at the time of its decay, otherwise the angle is shifted from 180° .

For the determination of the γ -quantum energy, it is crucial that its energy is completely absorbed within the detector. In the energy range considered in this work, the secondary electrons and positrons released in the photon interaction generally have a range of $10 \mu\text{m}$ up to a few $100 \mu\text{m}$ within which they lose their complete energy by interactions with the detector material. On the other hand, Compton-scattered photons and the photons produced in the annihilation of a positron have a mean free path of about a few cm for their interactions within the detector medium. As a result, for a detector of finite size they may escape from the detector volume as illustrated in figure 3.6.

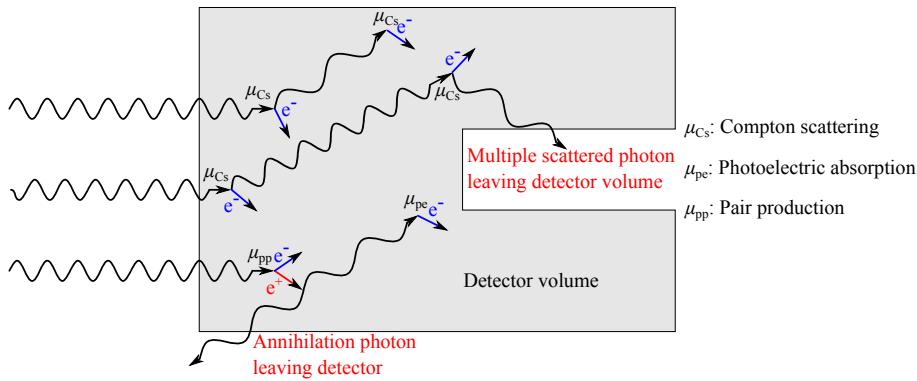


Figure 3.6: Illustration of photon interactions in a detector volume of a finite size. Any photon escaping the detector is a deficiency of absorbed energy and forms out characteristic shapes shown in figure 3.7.

In consequence, the detection of photons of a specific energy will always give a spectrum of energy deposited in the detector. As an example, figure 3.7 shows the γ -energy spectrum measured after the inelastic scattering of α -particles with ^{16}O . The distribution arises due to the γ -transition of the second excited state to the ground state in ^{16}O .

The green shaded region in figure 3.7 shows the full absorption peak at an energy of

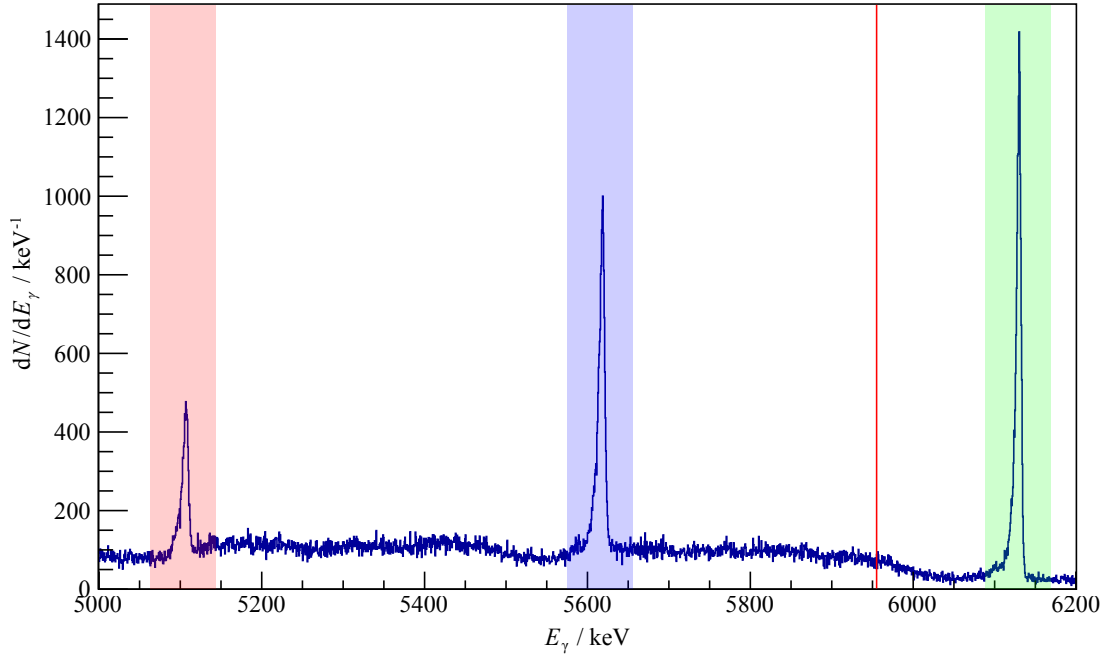


Figure 3.7: Distribution of γ -energies arising due to the transition from the oxygen second excited state to the ground state of the nucleus.

$E_\gamma = 6129.89$ keV [33]. This is not necessarily due to a photoelectric absorption. The γ -quantum can also lose its energy by means of the Compton scattering or it can interact by pair production. The subsequent full absorption of the scattered γ -quanta, electrons, positrons and the annihilation radiation within the detector will also contribute to the full absorption peak.

In case of Compton scattered γ -quanta leaving the detector volume, the Compton-continuum is built up and is limited by the Compton-edge. It is formed by the photons that are scattered in the backward direction, transferring the maximum possible energy to the electrons and is indicated by the red line in figure 3.7. The energy loss ΔE_γ of the photon due to Compton scattering depends on the scattering angle ϑ_γ :

$$\Delta E_\gamma = E_\gamma - E'_\gamma = E_\gamma \frac{\frac{E_\gamma}{m_e c^2} (1 - \cos \vartheta_\gamma)}{1 + \frac{E_\gamma}{m_e c^2} (1 - \cos \vartheta_\gamma)} \quad (3.12)$$

where E_γ is the initial energy of the γ -quantum. The energy E_{CE} of the Compton edge can be obtained by setting $\vartheta_\gamma = \pi$, resulting in:

$$E_{\text{CE}} = \Delta E_\gamma(\vartheta_\gamma = \pi) = \frac{2E_\gamma^2}{m_e c^2 + 2E_\gamma} \quad (3.13)$$

In the case of the γ -energy $E_\gamma = 6129.89$ keV, the Compton edge is located at $E_{\text{CE}} = 5884.6$ keV.

If one of the photons, which are emitted by the annihilation of the positron, leaves the

detector the recorded energy is reduced by the energy equivalent of the rest mass of an electron. This forms the *single escape peak* in the γ -energy distribution which is shown by the blue shaded area in figure 3.7. In case that both annihilation photons escape, the peak in the red shaded area in figure 3.7 is formed, which is shifted towards lower energies by the energy of two electron rest masses and is called *double escape peak*. The escape peaks are located on top of the Compton continuum.

The efficiency of a γ -detector is mainly dependent on its absorption capability, its capacity to convert the photon energy into the number of charges, and its collection efficiency. An important characteristic of a γ -detector is the Peak-to-Compton ratio [28].

In general, the peak-to-Compton ratio increases with the effective atomic number and the size of the detector. A detector with infinite size and complete charge collection would have an infinite peak-to-Compton ratio.

In reality however, the full-absorption probability of a detector is influenced by its geometry and material as well as the photon energy. Another crucial characteristic of a detector system is its energy resolution which is typically given as the full width at half maximum (*FWHM*) of a peak at a certain energy. Regarding the energy resolution, semiconductor detectors such as the high purity germanium (HPGe) detector, are far superior to scintillation detectors that provide high counting efficiency. Since not the counting efficiency but the energy resolution is more important for this work, a HPGe is used.

3.1.3 HPGe-detector

Semiconductor detectors are in principle diodes operated in reverse direction as illustrated in figure 3.8. Interaction of secondary electrons and positrons produced by γ -interaction excites electrons of the valence band to the conduction band and produces electron-hole-pairs. These pairs drift in the electric field caused by the electrode voltage and induct an electric signal which can be processed. Due to contacting, in the border area of the semiconductor the charge collection probability is deteriorated. Therefore, these regions are called dead layers, where in contrary the volume in which the produced charges are collected, is called sensitive volume. The amount of the created electron-hole-pairs, and consequently the signal height, is proportional to the energy deposit in the sensitive volume of the detector. Germanium has a band gap of 0.67 eV at room temperature. The narrow band gap leads to a high dark current at room temperature due to electrons which are excited from the valence band to the conduction band by the thermal energy. This makes it impossible to operate a HPGe detector at room temperature. Therefore, it is cooled down to liquid nitrogen temperature of 100 K. The detector used in this work is an N-type coaxial HPGe detector of type GAMMA-X purchased from Ortec [64]. The outer contact is an ultra thin ion-implanted boron contact with a thickness of 300 nm which

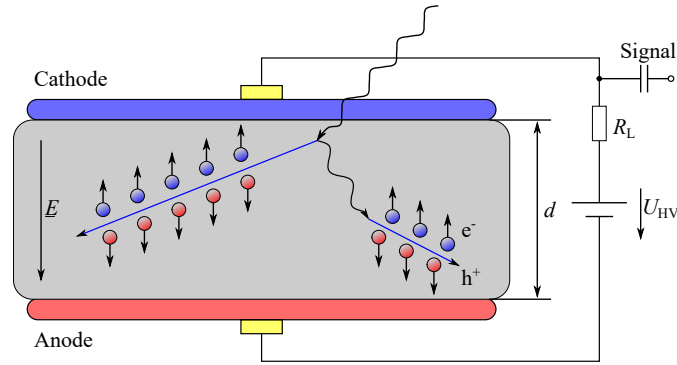


Figure 3.8: Principle of a semiconductor detector. Incident radiation produces electron–hole–pairs which drift in the electric field applied by the electrodes.

minimises the dead layer on radiation entry. A lithium diffused contact with thickness of $700\ \mu\text{m}$ [64] is used as inner contact. Charges produced within the dead layer are not collected and, hence, do not contribute to the detector output signal. Figure 3.9 shows a cut of the detector as used in this work. Due to the bore hole ($\varnothing = 13\ \text{mm}$), the detection probability for incident γ -quanta is reduced in the centre and has to be taken into account in the data analysis (see also section 5.3).

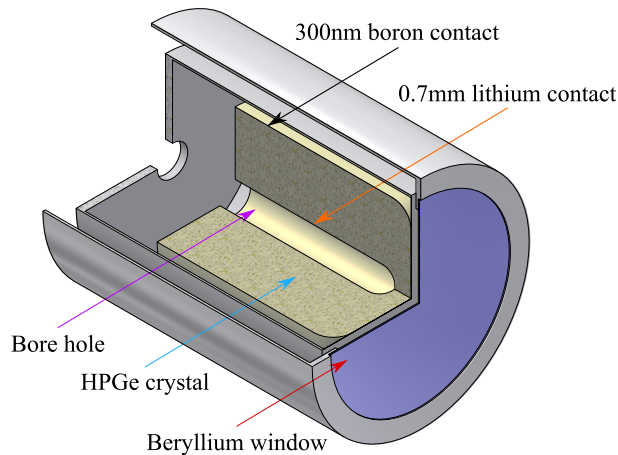


Figure 3.9: N-type γ -detector with borehole as used in this work.

A special feature of the Ortec GAMMA-X detectors is its high resistance against the damage caused by fast neutrons compared to conventional coaxial germanium detectors [64]. This is an essential property as neutron production cannot be excluded during the experiment.

Neutrons may be produced by nuclear reactions in the experimental apparatus. Fast neutrons produce negatively charged defects, namely hole trapping centres, within the germanium. Due to the N-type HPGe detector being based on the collection of electrons, the hole collection has only a minor contribution to the output signal. Therefore, the degradation in resolution by neutron damage [24] can be considered as small [71].

The detector is cooled mechanically using the Ortec X-Cooler III that is designed especially for Pop-Top detectors. It is free of liquid nitrogen and consists of a compressor

unit and a cooling head on which the detector capsule is mounted. Both units are connected by a hose enabling a flexible mounting of the cooling system on the experimental set-up.

3.2 Data acquisition

The heart of the data acquisition system is the desktop digitiser DT5780 of the company CAEN shown in figure 3.10. The acquisition software that was developed for this work is based on Cern's ROOT-framework which enables efficient data handling, also for high data rates.

The DT5780 is basically a 14-bit 100 MSmp/s digitiser with a field programmable gate array (FPGA) which allows on-line digital pulse height analysis (DPHA). It has two independent channels and, especially for usage with scintillation and semiconductor detectors, two programmable high voltage power supplies (up to 5 keV) plus two Sub-D connectors for powering the pre-amplifiers. The DPHA of the system assigns a time stamp and a channel number to the incoming signal in accordance with the collected charge in the detector which is proportional to the deposited energy. The advantage of a digitiser is that the system can also be used as a digital oscilloscope as it records the waveform of the input signal. This is a useful feature for the optimisation of the parameters for the DPHA. The digitiser also supports safety functions such as the disabling of the high voltage supply if the detector temperature exceeds a critical value. This provides an effective protection of the sensible HPGe detector, especially its field effect transistor (FET) which is located in the evacuated detector capsule.



Figure 3.10: Shown is a rear- and front-view of the desktop digitizer *CAEN* DT5780 which was used for data acquisition ¹.

¹http://www.caen.it/documents/work_EcommerceProduct/756/MCA_G.jpg

The software for data acquisition, data handling, presentation and the user interface was developed in the frame of this work for a Microsoft Windows[®] platform using Visual Studio 2012 (VC++2011) in the programming language C++. The software for the file container, graphical representation during the measurements and the data management was developed using the classes supplied by the ROOT [19] framework. It enables highly efficient data handling and automatic data analysis. The software is modularly designed allowing easy extensions and modifications afterwards. An overview over the modules and data exchange between these modules is given in figure 3.11.

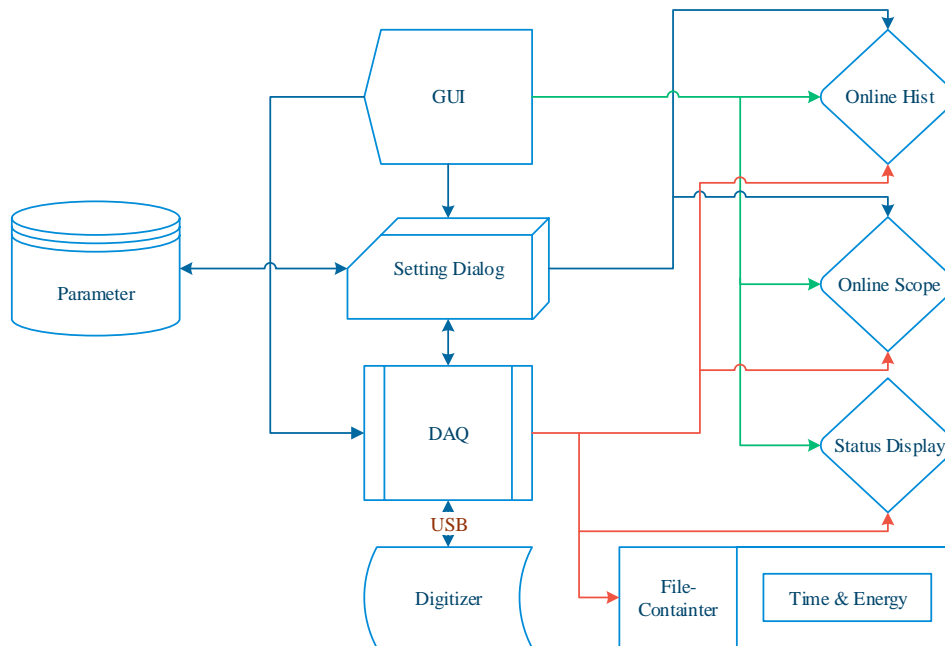


Figure 3.11: Simplified data stream diagram of the data acquisition software.

The class module **DAQ** manages the connection to the digitizer and the entire communication like update of settings for the signal processing, enabling or disabling the high voltage supply and also the acquisition and management of the incoming data. The digitiser supports the connection of peripheral by USB or PCI optical link bridge which is also supported by the class module DAQ. An uninterrupted data stream was realised by the run of different parts of the DAQ module on individual threads. The data acquired is directly written into a ROOT TTree structure wrapped in a TFile container with time stamp and channel number of the event.

The class DAQ was developed with the intention to provide modularity so that it can be used as a basis for other custom acquisition applications with hardware from CAEN. For this purpose, relevant register settings of the digitizer were wrapped into class methods with human readable parameters.

The class modules **Online Hist**, **Online Scope** and **Status Display** are mainly graphical representation classes which are not involved in processing the raw data, and

hence, only act as receivers. The graphical interfaces of the software are shown in figure 3.12.

Online Hist generates the frequency spectra in real time during the measurement. It shows the number of γ -counts as a function of the channel number. A monitoring of the temporal change of the spectra is possible at any time during the acquisition. To avoid a procedural interference with the data acquisition and utilise the capacity of multi-core processors, the frequency spectra is also generated in an own independent thread. Furthermore, a tool-box is available which enables fitting various functions to the recorded frequency spectra. The frequency spectra can be saved at any time to a file in various file formats. In addition, the x-axis of the frequency spectra can be calibrated by using a linear function.

The class module **Online Oscilloscope** enables the monitoring of the waveform of the input signal, the applied trapezoidal fit to the input signal. This feature is useful for adjusting the signal processing parameters of the DPFA to a specific connected detector to achieve its maximum performance and energy resolution.

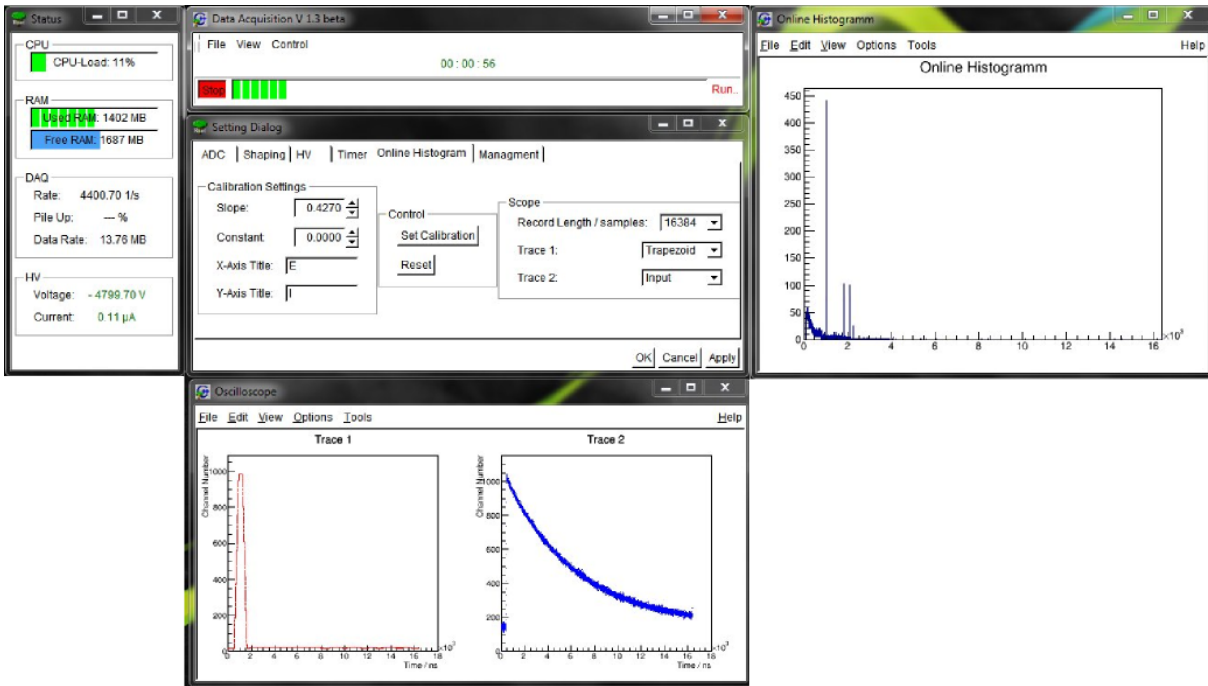


Figure 3.12: A screenshot of the graphical front end of the data acquisition software.

The class module **Setting Dialog** manages the settings of the digitiser, parameters for the analogue–digital converter, DPFA, high voltage supply, as well as settings for the on-line histogram and oscilloscope. All settings can be stored to a file which can be reloaded by the Setting Dialog. This ensures that measurements can be carried out with the same set of parameter values. The value of the high voltage can be set in steps of 100 mV. The voltage ramp for switch–on and shut–down is independently adjustable in steps ranging from 1 V/s to (50) V/s. For safety, a maximal allowable voltage and current can be set. If the current reaches the threshold, the high voltage power supply will be ramped down

to zero using the voltage ramp for shut-down. This also applies to a voltage shut-down process which starts if the detector temperature exceeds the manufacturer's predefined critical value. The high voltage power supply can be activated from the user menu in the main graphical user interface. During non-error initiated shut-down or switch-on, the numbers on the HV section of the Status Display are printed using blue font colour. If the adjusted value is reached, the font colours will switch to green. In the case of error the font-colour will switch to red and show the actual voltage during ramp down. The red font colour will be hold until the high voltage power supply is re-setted.

3.3 Energy calibration

The overall detector system, consisting of the HPGe-Detector, pre-amplifier and the digitiser, was calibrated using two standard sources which provide three characteristic γ -lines listed in Table 3.1. For the energy calibration, the γ -energies of the three isotopes were

Nuclide	Decay	E_γ/MeV
^{137}Cs	$^{137}\text{Cs} \xrightarrow{\beta^-} ^{137}\text{Ba}(11/2^-) \xrightarrow{\gamma} ^{137}\text{Ba}(3/2^+)$	0.662
^{60}Co	$^{60}\text{Co} \xrightarrow{\beta^-} ^{60}\text{Ni}(4^+) \xrightarrow{\gamma} ^{60}\text{Ni}(2^+)$	1.173
^{60}Co	$^{60}\text{Ni}(2^+) \xrightarrow{\gamma} ^{60}\text{Ni}(0^+)$	1.333

Table 3.1: List of γ -lines used for the calibration of the γ -detector system.

plotted versus the corresponding channel numbers of the peak positions. The calibration function was determined by a linear regression of the data points (see also figure 3.13). The obtained calibration function is only valid for a particular set of parameter values

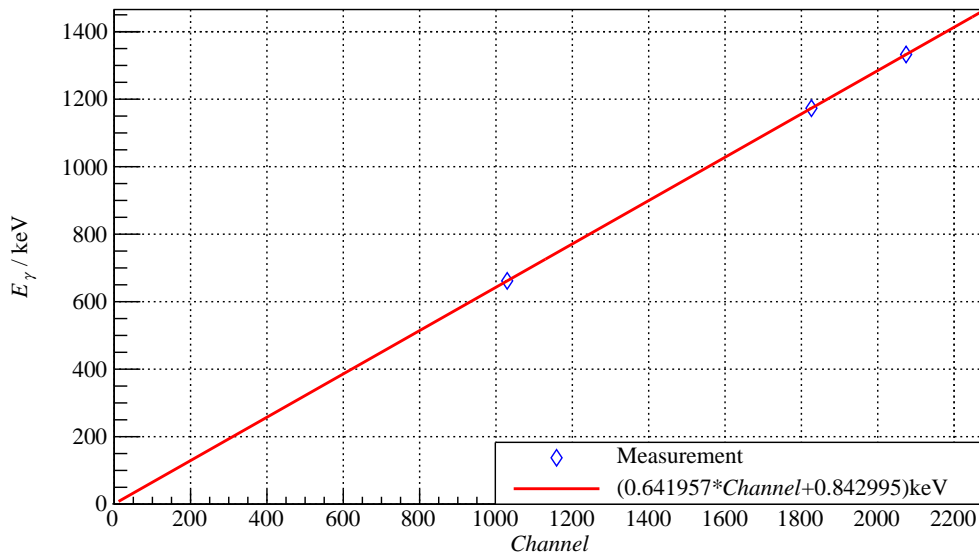


Figure 3.13: Calibration function of the γ -detector system at a bias voltage of 4.8 kV.

and therefore, the procedure has to be repeated if a parameter value changes. In table 3.2 the parameter values used in this work are listed. During the experiment, the γ -lines

Parameter	Value	Parameter	Value	Parameter	Value
Gain	1	Decimation	0	DC-Offset	-47,1%
Energy Norm Fac.	1	Trigger-Hold Off	12,8 μ s	Rise-Time	0,7 μ s
Trigger Smoothing	8	Input-Decay	58 μ s	Shaping-Time	4 μ s
Flat-Top-Time	3 μ s	Base-Line-Mean	4 Smp	Peaking-Delay	1,5 μ s
Peak Mean	16 Smp	Base-Line-Hold	100 ns	Peak-Hold Off	770 ns
Input-Range	1,4 V _{pp}	Record-Length	1024 Smp	Voltage	4800 V

Table 3.2: Parameter values used in the present experiment. All parameters are accessible via the graphical user interface shown in figure 3.12.

from ^{16}O nuclei could be observed and be used to check the energy calibration and its linearity.

3.4 Target

As explained in section 2.3, the determination of the stopping power by means of the IDSAM requires the measurement of two γ -energy spectra. The first one, called unattenuated γ -energy spectrum dN_a/dE_γ in the following, is needed to obtain $W(v_0)$ in equation 2.25 by using equation 2.26. The second spectrum dN_a/dE_γ , called attenuated γ -energy spectrum, contains the information on the stopping power of the target medium. For its measurement, the target system to slow down $^{12}\text{C}^*$ projectiles has to be constructed.

3.4.1 Vacuum target

The **unattenuated** γ -energy spectrum was measured using a sandwich target system which consists of 10 self-supporting carbon micro-leaf foils with a thickness of 20 nm each. The distance between the foils was chosen such that the relative fraction f of the $^{12}\text{C}^*$ projectiles produced in the previous foil and reach the next foil is lower than 10^{-4} . This fraction can be estimated from the lifetime τ of the excited state and the maximal velocity of the $^{12}\text{C}^*$ projectiles:

$$f \leq 1 - \exp \left[-\frac{d}{\tau v_{\max}} \right] \quad (3.14)$$

For the α -projectile energy of 12 MeV, v_{\max} amounts to about $3.3 \cdot 10^{-2} c$, resulting in $f = 10^{-4}$ for $d = 500 \mu\text{m}$ which was chosen as distance between two neighbouring foils.

The target shown in figure 3.14 contains two pure tantalum apertures which prevent the α -particles hitting other mechanical components. The first one, seen in α -beam direction has a smaller diameter than the second one. In this way, it is ensured that the α -particles passing through the first tantalum aperture are guided to the beam dump.

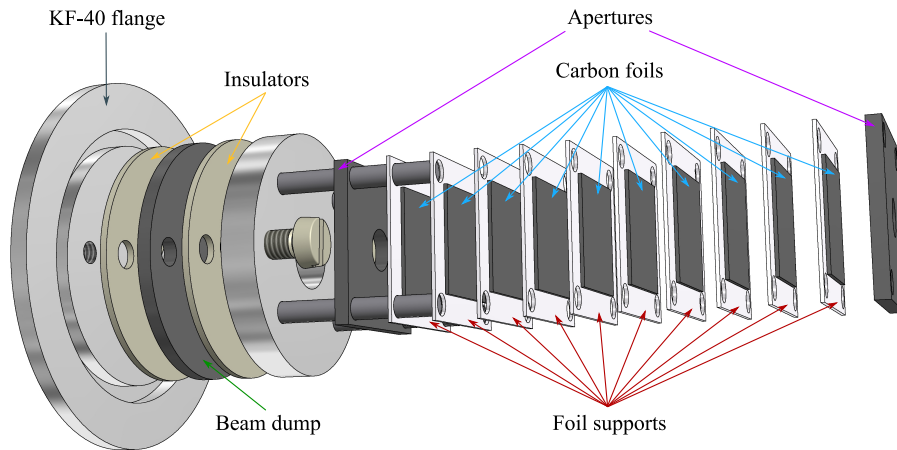


Figure 3.14: Sketch of the vacuum target used for measurement of the starting energy spectra.

The beam dump is also made from pure tantalum and is electrically isolated from the rest of the target. The second tantalum aperture is electrically connected to the foil support plates which were made of aluminium. Due to the separated feed-through of the beam dump, foil supports and the first tantalum aperture the currents on these components can be measured individually. The information on the currents are used to adjust the beam alignment and its focus.

3.4.2 Water target

The water target is the centre piece of the present experiment. It is used to measure the attenuated γ -energy spectra that contain the information on the stopping power of the target, i. e. the water. The following criteria were considered in the target construction: it has to provide a flange which can be attached to the beam line, enabling to keep the water reservoir at atmospheric pressure by sealing against the vacuum of the beam line. This was achieved by dividing the target system into two cylindrical components, the water target and the vacuum sealing component, which are then bolted together. The vacuum volume was sealed against the atmosphere by means of a Viton-O-ring. The housing of the water-filled target is made of aluminium. It has to be avoided that the α -particle beam hits any part of the housing. Otherwise, the large cross sections of aluminium for γ - and neutron production will lead to a high background (see also figure 3.16). Therefore, the surface of the aluminium housing was shielded against the incoming α -particle beam. For this purpose, an aperture system was inserted to guide the α -beam to the water volume (figure 3.15). The aperture system consists of four segments connected each to highly sensitive current amplifiers. By measuring the currents on the four segments, the information on the beam position can be obtained. The diameter of the aperture is 4 mm. If the beam hits the segments of the aperture, electrons may escape from the surface of the segments, leading to a wrong reading of the current onto the segments. To reduce the number of escaping electrons, a second tantalum aperture with a diameter of 8 mm was

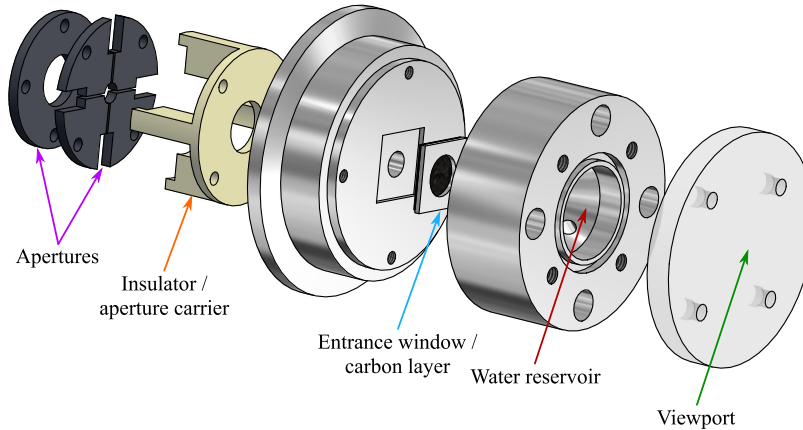


Figure 3.15: Exploded assembly drawing of the aperture system which contains the four-segmented measurable aperture facing towards the beam line.

placed in front of the four-segment aperture which is set to a negative potential of 300 V.

3.4.3 Entrance window

The entrance window is the most critical component of the water target. Therefore, different materials for the construction of the entrance window were investigated with respect to their physical and mechanical properties. It has not only the task to seal the water against vacuum but also to carry sufficient amount of carbon to produce enough $^{12}\text{C}^*$ -projectiles. Regarding the mechanical strength, the entrance window has to withstand the force caused by the atmospheric pressure. Several materials are available which have the required mechanical strength, such as polyethyleneterephthalat (DuPont Mylar) foil or HAVAR. However, the foil must meet additional requirements in the measurement.

One requirement is a small energy and angular straggling of the incident α -particles caused by scattering processes with the window material. These directly influence the reaction kinematics of α -particles with the carbon layer attached on the entrance window foil. Large straggling would destroy the applicability of the approximation needed for further analysis.

Another requirement is a low cross section for the production of background γ -quanta due to nuclear reactions with α -particles in the energy region of 12 MeV.

Furthermore, and most important, the cross sections for neutron production must be as low as possible. A high neutron background implies the production of γ -quanta by means of (n, γ) reactions in the surrounding material which would interfere the measurement. Additionally, the detector resolution would degenerate due to the production of hole trapping centres by fast neutron bombardment [73].

For the selection of an appropriate entrance window material, the cross sections of γ - and neutron production were calculated for different materials using the software TALYS

[48]. The investigation was restricted to γ -quanta and neutron production as these have a high probability to reach the detector or surrounding material and interact with it.

Aluminium is often used because of its easy processibility. Additionally, the angular and energy straggling of the traversing α -particles can be expected to be rather small. For the calculation, only the isotope ^{27}Al has to be considered because of its natural abundance of 100 %.

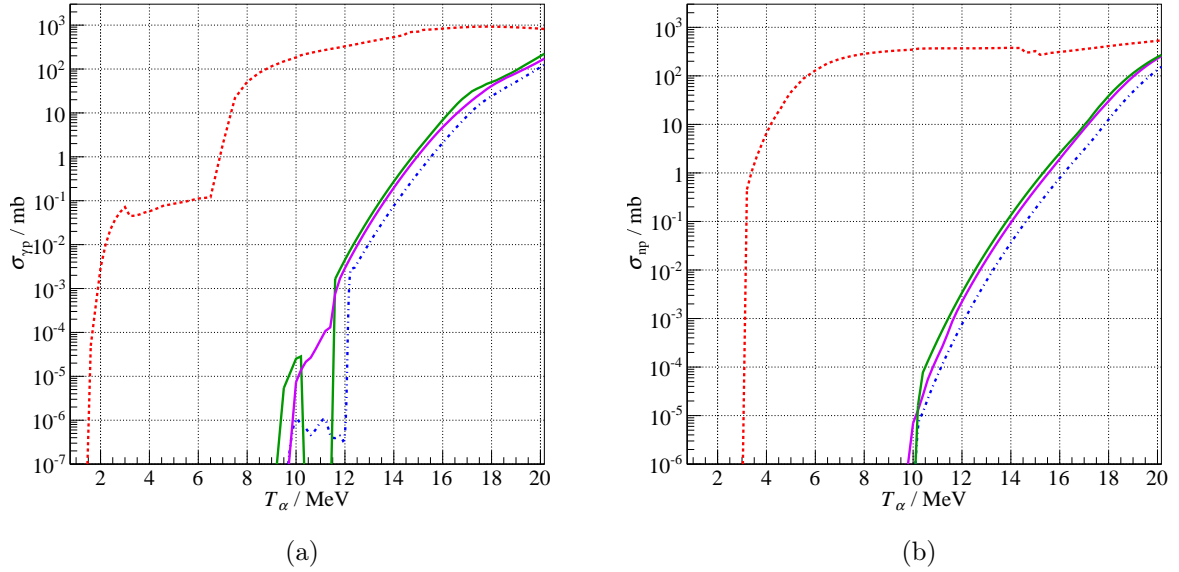


Figure 3.16: (a) Cross section for γ -production: aluminium (red dashed), tantalum (green solid), tungsten (violet) and platinum (blue dash dot) as function of the kinetic energy T_α of α -particles. (b) Neutron production cross section of aluminium, tantalum, tungsten and platinum.

Tantalum is often used as the material for beam-collimation apertures and beam dumps due to its relatively low γ - and neutron production cross section. However, this advantage is accompanied by higher elastic scattering cross section for α -particles and consequently, by larger angular straggling. The natural abundance of tantalum is also restricted to one isotope, ^{181}Ta .

Platinum should lead to an even lower production rate of γ -quanta and neutrons compared to tantalum, but at the expense of an increased energy and angular straggling.

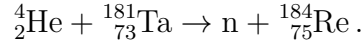
Another possible candidate for the window material is tungsten also due to its expected low cross sections for γ -quanta and neutron production as shown in figure 3.16. As in the case of platinum, natural tungsten consists of multiple isotopes which have to be considered in the calculation of cross sections for γ - and neutron production.

In the first step, the γ -quanta and neutron production of different materials for incident α -particles are evaluated. Figure 3.16 shows that the cross sections of aluminium are very high compared to those of other materials. Therefore, aluminium is not suited as material for the entrance window.

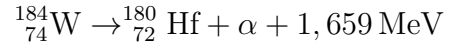
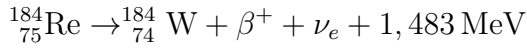
The cross sections of platinum and tantalum for the production of γ -quanta and neu-

trons are significantly lower compared to aluminium. The dip in the γ -quanta production cross section of platinum, which can be seen in figure 3.16(a), arises from the opening of the neutron emitting channel at that α -energy. Its nuclear reaction with α -particles yields reaction products which can be a radioactive isotope and contribute to the background radiation.

In case of the bombardment of tantalum with α -particles with an energy up to 12 MeV, the only relevant reaction is the production of rhenium ^{184}Re :



The threshold energy for this reaction is 10.081 MeV and the Q -value is -9.86332 MeV. At $T_\alpha = 12$ MeV, the cross section for the production of ^{184}Re is in the order of a few μbarn . The produced ^{184}Re is a radioactive isotope which decays by:



with a half-life of $T_{1/2} = 38$ d until the stable isotope ^{180}Hf is reached. Apart from the emission of α -particles during the decay to hafnium, there is positron emission during the decay process from $^{184}_{75}\text{Re}$ to the radioactive tungsten isotope $^{184}_{74}\text{W}$. The emitted α -particles and positrons will mostly not be detected but a large contribution to the background will occur due to the annihilation of the positrons with target electrons.

The production of unnatural isotopes by α -particles with energies below 12 MeV is negligible. Therefore, γ -quanta are mainly produced by the nuclear reaction of α -particles with the constituents of natural platinum. The reaction Q -values for the production of γ -quanta and neutrons are given in table 3.3 for different platinum isotopes. The same applies to the neutron production by nuclear reactions with the isotopes contained in natural platinum.

Isotope	Abundance / %	$Q_{\gamma p}$ / MeV	Q_{np} / MeV
^{190}Pt	0.01	-2.71638	-11.90880
^{192}Pt	0.79	-2.04050	-10.93900
^{194}Pt	32.90	-1.38281	-9.86794
^{195}Pt	33.80	-0.82500	-7.48787
^{196}Pt	25.30	-0.71841	-8.74694
^{198}Pt	7.20	-0.13528	-7.88937

Table 3.3: Q -values for γ -quanta and neutron production by α -particle bombardment of natural platinum isotopes calculated using TALYS [48].

For α -energies lower than 12 MeV, the cross sections for the production of unnatural isotopes lie between a few nano barn and several hundred μbarn . The mostly produced

isotope is ^{189}Os . It is stable and is produced in its ground and first excited state with similar probabilities. Additionally, the radioactive isotope ^{185}Os can be produced which decays to stable ^{182}W by α -particle emission. The bombardment of the isotope ^{182}W with α -particles can produce the isotope ^{185}Os which decays via electron capture to the stable isotope ^{185}Re . The abundances of tungsten isotopes and their corresponding Q -values for production of γ -quanta and neutrons are given in table 3.4.

Isotope	Abundance / %	$Q_{\gamma p}$ / MeV	Q_{np} / MeV
^{180}W	0.13	-2.9570	-11.6201
^{182}W	26.3	-2.82042	-11.0843
^{183}W	14.3	-2.72129	-9.01124
^{184}W	30.67	-2.14338	-10.1330
^{186}W	28.6	-1.37645	9.168755

Table 3.4: Q -values for γ - and neutron production by α -particle bombardment for the constituent isotopes of natural tungsten calculated by *TALYS*[48].

For the investigation of the angular and energy straggling of the α -particles after traversing the entrance window a simulation was carried out using the Geant4 toolkit [21]. The simulations were carried out for different materials of various thicknesses. The thickness of the material was chosen dependent on the minimal thickness that is available as a non-porous foil to ensure a vacuum-tight sealing. In the case of tantalum, a thickness of $3\ \mu\text{m}$, for platinum a thickness of $5\ \mu\text{m}$ and for tungsten a thickness of $9\ \mu\text{m}$ were chosen [38]. Due to its mechanical strength, an entrance window made of tantalum can be thinner than those made of platinum or tungsten.

The primary energy of the α -particles was set to $T_\alpha = 12\ \text{MeV}$. Whenever an α -particle crossed the border between the entrance window and the thin carbon layer attached to the backside of the entrance window, its energy and momentum was recorded. To save computation time, the calculation of the track was aborted as soon as the α -particle has been registered in the carbon layer. Additionally, the electron transport was switched off.

The scattering angle ϑ_α of α -particles was obtained from the recorded momentum vectors:

$$\vartheta_\alpha = \cos^{-1} \frac{p_{z,\alpha}}{|\underline{p}_\alpha|} \quad (3.15)$$

where $|\underline{p}_\alpha|$ and $p_{z,\alpha}$ is the total momentum and the z -component of the momentum, respectively. The incident α -beam axis coincides with the z -axis.

Figure 3.17 (a) shows the angular distributions of α -particles after traversing the different window materials. The cumulative, defined as the integral of the angular distributions from zero degree up to the actual angle, is depicted in figure 3.17(b). As it can be seen from figure 3.17 (a), the angular straggling of α -particles which traversed an entrance window made of tantalum is significantly smaller than of those that traversed an entrance window made of platinum or tungsten. This is also indicated by the cumulative

spectra shown in figure 3.17(b), where the probability for large scattering angles in the case of tantalum is much smaller than in the case of platinum and tungsten. For smaller angles, the cumulative spectra for α -particles which traversed the tantalum window show a larger slope and more pronounced peaking characteristics compared to those of tungsten and platinum.

Material	d / μm	$\Delta\vartheta_\alpha$ / degree	$E_{\alpha,Peak}$ / MeV	$FWHM(E_{\alpha,Peak})$ / keV
Tantalum	3.0	3.15	11.2	85.8
Platinum nat.	5.0	5.30	10.3	125.6
Wolfram nat.	9.0	7.10	9.2	200.0

Table 3.5: Summary of results from *Geant4* simulations.

The results of the investigation are summarised in table 3.5. The value $\Delta\vartheta_\alpha$ gives the angular interval into which 90% of the α -particles are scattered. Figure 3.18 shows the energy spectra of the α -particles after traversing the entrance window. The mean energy loss of 12 MeV α -particles in the tantalum, platinum and tungsten foil is, 0.8 MeV, 1.7 MeV and 2.8 MeV, respectively. As expected, the energy spectra are not only shifted towards lower energies but also broadened. Tungsten and platinum would be a good choice as material for the entrance window when taking into account only the production cross section for γ -quanta and neutrons. But with respect to the angular and energy straggling, tantalum is the best choice despite its higher cross sections for background production.

Figure 3.18 shows that, to obtain the same energy in the carbon layer, the energy of the primary α -particles in the case of platinum and tungsten has to be higher than

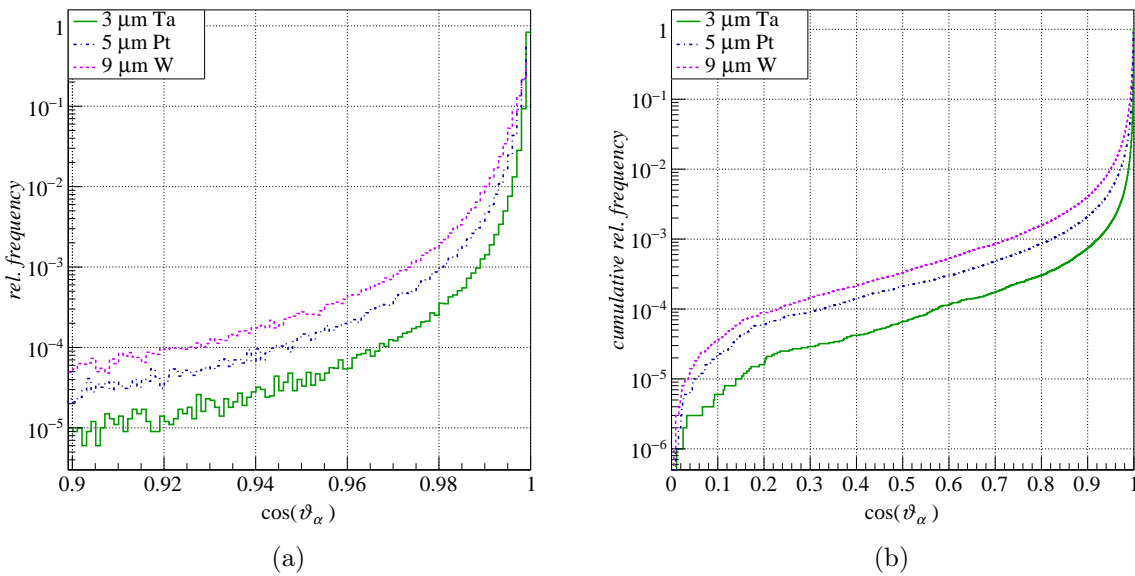


Figure 3.17: (a) Angular and (b) and cumulative angular distributions of α -particles with an incident energy of $T_\alpha = 12$ MeV.

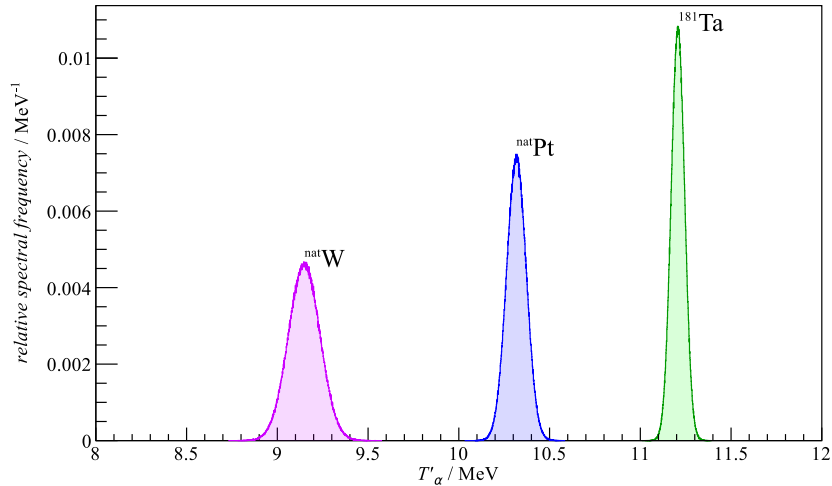


Figure 3.18: Energy spectra of α -particles of 12 MeV initial energy after traversing the entrance window made of (from left to right) 9 μm tungsten, 5 μm platinum and 3 μm tantalum.

in the case of tantalum. The use of tantalum would lead to a lower background, as the required α -reaction energy for the production of $^{12}\text{C}^*$ projectiles can still be obtained with a primary α -particle beam energy at which the cross section for the background production is negligibly small.

In addition, tantalum provides a higher tenacity compared to platinum (see table 3.6) which is also important, as the window has to withstand the atmospheric pressure against vacuum.

Material	tenacity / MPa	yield strength / MPa	hardness (Vickers)
Tantalum	760	705	200
Platinum	200–300	185	100

Table 3.6: Mechanical properties of tantalum and platinum [38].

In summary, the results of the simulations indicate that tantalum is the most suitable material for the entrance window.

3.4.4 Carbon layer

The thin carbon layer with a thickness of a few tens of nanometres has to be brought onto the backside of the entrance window interfacing the water target. The layer has to be thin enough so that the energy loss of $^{12}\text{C}^*$ projectiles in the layer is negligibly small.

In this work, several coating methods have been tried to bring a thin carbon layer onto tantalum. The first method uses carbon micro leafs supplied by *Goodfellow* [38]. The micro leafs are delivered on a glass support. They can be detached from the glass using distilled water. The micro leaf then floats on the water surface and can be caught up by the tantalum foil.

The second method is the deposition of amorphous carbon onto tantalum using a sputter technique. This was performed by the *Fraunhofer-Institut für Werkstoff- und Strahltechnik* [17].

The third method is the ion beam deposition of carbon ions onto tantalum using an ion beam source. This technique produces a diamond-like carbon (DLC) coating on the tantalum foil. An overview of this technique is given by Hofsäss *et al.* [42]. For the growth of a DLC coating, the ions were produced in a plasma source, accelerated to 30 keV, separated by mass and guided into the ultra high vacuum chamber where the entrance foil (here substrate) is located and electrically connected to a deceleration unit where the ions are decelerated down to about 600 eV [76]. DLC is a material which belongs to the class of amorphous carbon but also possess diamond-like properties owing to the presence of sp^3 bonds. The fraction of sp^3 bonds and the plasmon energy, which is connected to this fraction by the density of the valence-electrons, is dependent on the ion energy and the compressive stress of the thin film [43]. By vacuum annealing the compressive stress in the films can be almost completely removed, but the fraction of sp^3 bonds is preserved [43]. For the growth of the DLC thin films with thickness of 20 nm and 50 nm, an ion energy of 600 eV was used [44]. This gives a sp^3 fraction of about 60% and a plasmon energy of about 29.3 eV [43]. This ion energy was chosen due to the expected high yield of sp^3 bonds and only a moderate compressive stress. If this compressive stress exceeds a certain amount the coating could resolve from the substrate, crack or damage the entrance window. Another benefit from using this energy is that a thin layer (few atomic layers) of tantalum-carbide is formed and provides a very strong bond between the substrate and the DLC coating [44].

3.5 Target moving system

The correct beam position and incident angle of the α -particles onto the target has shown to be crucial for low background. Therefore, an on-line monitoring and also correction of the beam position relative to the target is necessary. As the beam guiding optics of the ion accelerator used for this work does not allow a quick and precise beam positioning into the target area, a target moving system was constructed to adjust the position of the water target relative to the incident direction of the α -beam. The flexible positioning is enabled by means of a bellows connecting the beam line to a movable carriage table on which the target is mounted. The positioning system is remote-controlled so that the target position can be manipulated from the outside of the experimental hall during the measurement.

The motion of the table is realised by two high torque DC motors and a rack-and-pinion drive. The mechanical layout is depicted in figure 3.19. The actual position of the carriage table is measured absolutely as a position-dependent resistance by linear

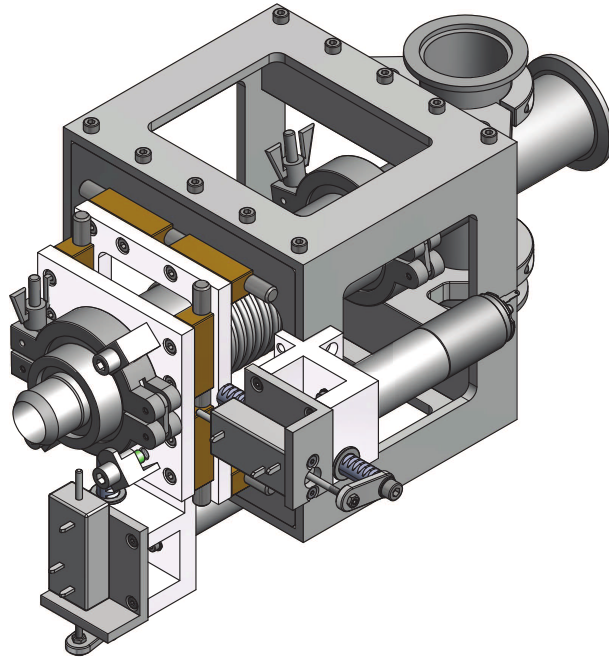


Figure 3.19: Target moving platform which can be mounted to the beam line and allows moving the target relative to the incident beam.

potentiometers. Inductive position sensors were not used due to possible disturbance by the fields of focusing and deflection magnets of the beam line. For safety and for the calibration of mechanical endpoints of the carriage table, limit switches were installed.

3.6 Electronics

For the measurement of the target aperture currents and the remote control of the target positioning system, several electronic and software modules have been developed. The software includes routines for the enclosed micro controllers and the interface on a personal computer. The modular design has several advantages such as the replacement of only defect modules in the case of failure or the possibility of the independent usage of individual parts of the system. To prevent interferences, all power circuits are strictly separated from control and measurement circuits. This is realised by a galvanic separation using opto-isolators. The system is subdivided into the following modules:

Amplifier Discrete amplifiers which can be configured independently.

Central Unit Unit which contains the interface and data acquisition.

Motor Control Unit (MCU) Controller board which executes the software for regulation of the position.

Power Section Unit which is controlled by the MCU and drives the DC motors.

The **amplifiers** for measuring the currents on the four segmented aperture and the target are based on the integrated circuit (IC) IVC 102 by Burr-Brown [20] shown in

figure 3.20. This IC is designed for the measurements of small currents like those of ion-chambers and photo diodes. It is also possible to use it for the amplification of the currents on the apertures and on the target irrespective of the polarity. Therefore, the measurement of both electron and ion currents are possible. The chip works as a switched integral amplifier based on operational amplifier (OP) using field effect transistors (FET). The concept of the IVC 102 is also called switched integrator trans-impedance amplifier. To ensure only a small current leakage, the TTL/CMOS compatible inputs are based on FET switches. For the integration of the current, the IVC 102 contains internal capacitors with the capacitance C_{int} . The output voltage U_O is given by

$$U_O = -\frac{1}{C_{\text{int}}} \int_0^{T_{\text{int}}} I_{\text{in}}(t) dt. \quad (3.16)$$

The advantage of using integration amplifiers in comparison to the conventional operational amplifier with a high feedback resistor is the decreased noise level as circuits with high resistances tend to be sensitive to thermal noise.

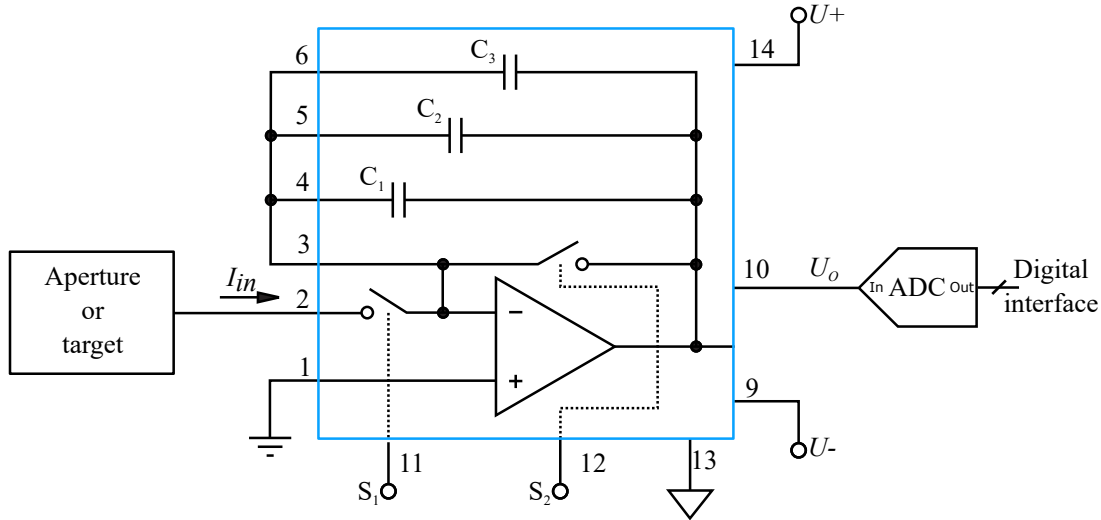


Figure 3.20: Schematic diagram of the IVC 102 adapted from [20].

The amplifiers were operated in the switched-input measurement (SIM) [20] mode which needs a more complex control of the switches S_1 and S_2 for the benefit of providing a hold of the output voltage after integration. This allows a more stable conversion by the analogue-to-digital converter ADC. During the hold time, the internal capacitors will not be charged but instead, the collected charge will be transferred from the sensor capacity to the internal capacitors as soon as the integration process starts by setting S_1 to logical low. In the case of high hold times this charge injection could lead to a saturation of the amplifier IC, what has to be prevented by choosing a current matching integration time. The transfer of charge from the sensor capacitance to the internal capacitors induces a step in the output voltage when switch S_1 is switched from high to low as depicted in

figure 3.21. By this no charge is lost which enables a precise measurement of the current.

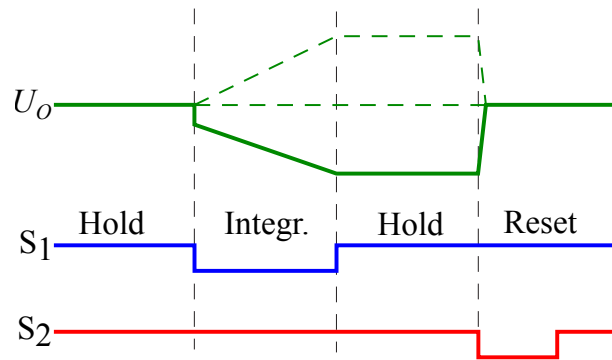


Figure 3.21: Schematic diagram of the timing of the IVC 102 operated in SIM adapted from [20].

The value of the output voltage is dependent on the capacity used for charge collection, which can be assumed to be constant during the operation (see also equation 3.16), and the integration time. The timing parameters are controlled by a micro controller (μC) to enable the selection of the integration time appropriate to the current. In addition, the value of the capacitor can be set, depending on the current range of interest. This is taken into account in the board layout shown in figure 3.22 by means of soldering pads which can be used to configure the internal capacitors.

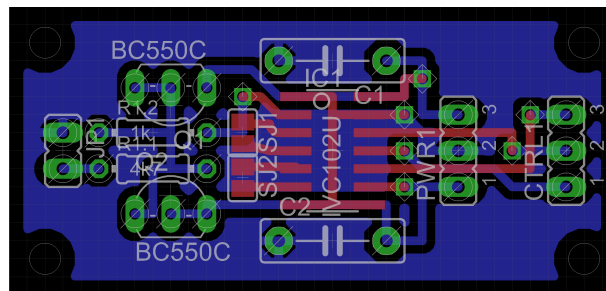


Figure 3.22: The board layout designed for an amplification module based on the IVC 102. The sensor can be connected to the input on the left hand side. The right hand side includes the connectors for power supply, control wires and output.

Each amplifier module contains an over-voltage protection which is connected in series between the sensor and the input of the IVC 102. This ensures that the voltage on the input of the IVC 102 never exceeds the supply voltage plus the voltage drop of a diode which is in general about 0.7 V. Such an overload protection needs fast diodes with inverse currents in the range of pA. Instead of using such kind of diodes, low level transistors like the BC550C [85] with comparable inverse currents and fast switching characteristics [78] can be used. In terms of reverse currents, a further improvement could be obtained using field effect transistors instead of bipolar transistors. The amplifier modules have easily detachable connectors for input signal, control, power supply and output signal enabling a fast exchange of the modules.

The **central unit** controls the modules and manages the data stream between the components. It holds a slave μC used to generate and receive trigger signals for synchronising the data acquisition by the ADC and the timing of the amplifiers. It is connected via the I²C bus to the master μC from which it receives the values for the timing. The master μC communicates with the peripheral components, handles and processes the raw data. It is connected by a Universal Serial Bus (USB) to Universal Asynchronous Receiver Transmitter (UART) bridge to a PC which communicates with the μC by means of a specifically developed software.

The μC platform used in this work is based on Arduino Nano 3.0 kits which are basically an Atmega 328 μC with a USB to UART bridge. Furthermore, the platform Arduino [77] is programmable with a language syntax similar to C++ and also provides an object-orientated approach.

The conversion of the analogue voltage from the amplifier modules into a digital signal is realised with the analogue digital converter (ADC) MAX127 [55] providing four different programmable input ranges ($[0\text{ V}, 5\text{ V}]$, $[0\text{ V}, 10\text{ V}]$, $[-5\text{ V}, 5\text{ V}]$ and $[-10\text{ V}, 10\text{ V}]$) at eight input channels with a resolution of 12 Bit and a sampling rate of 8 kSmp/s . The programming of the implemented features is done by set-up of the control byte sent from the master μC to the ADC. As the control byte, that contains the information on the active channel and its settings, is received, the acquisition starts. The format of the control byte is explained in detail in reference [55].

The time required for the communication and conversion has to be taken into account with respect to the integration time. To minimise the hold time, the sending of the control byte is done during the integration time so that the ADC conversion time perfectly matches the hold period. This has the advantage that the hold period can be chosen rather small and, hence, prevents saturation. For the adjustment of the timing of the readout, an output channel of the master μC was used for showing the time frame of communication. It is switched to high when sending the control byte and switched to low after the completion. The timing is illustrated in figure 3.23. After the 15-th of 18 clock cycles of the control bytes transmission from the μC to the ADC, the acquisition is started. This time frame is located at the end of the time interval t_{CR} . Therefore, the most stable acquisition is achieved if the negative edge of the time frame trigger of the master μC is located in the middle of the hold interval.

As described above, the position of the target relative to the beam line can be varied by the control of two DC motors (figure 3.19). The position is regulated by a control loop which compares a given value with the actual value from the linear potentiometers which were directly attached to the toothed rack of the drive.

The **Motor Control Unit** (MCU) is based on a plain Atmega328P μC with an Arduino boot loader. This enables the use of the C++ dialect of the Arduino project. The MCU establishes the connection of two position sensors, four end switches and can control

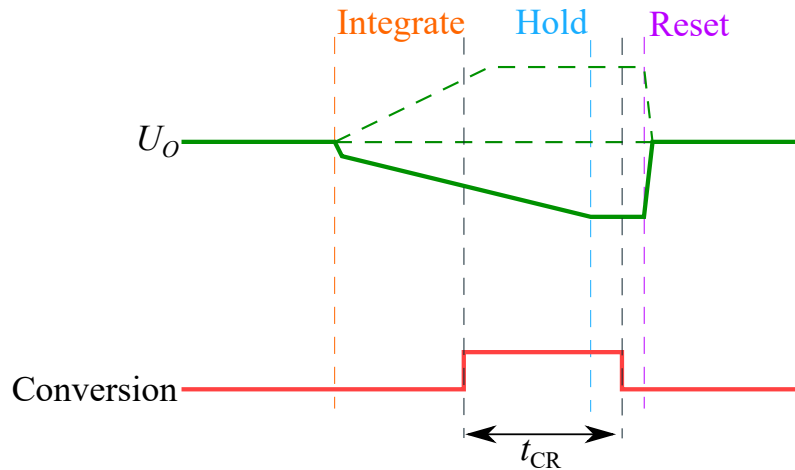


Figure 3.23: Timing of the readout of the ADC. The window t_{CR} is the time required to establish the communication between the μC and the ADC.

two drives independently at the same time. Each position sensor is equipped with an impedance converter to enable its connection to the input of the μC . The used operational amplifier LM358 [1] is not a rail-to-rail type and therefore is operated with a voltage of $V_{CC} = 12\text{ V}$. To match the voltage range of the internal ADC of the Atmega 328P, the position sensor circuit was designed with an output voltage interval of $U_{in} = [0\text{ V}, 5\text{ V}]$.

The output for each motor consists of two wires carrying the information of the direction and a pulse-width-modulated (PWM) signal for the velocity. The higher the difference between the set value and the actual value, the higher the velocity. If the set value is nearly reached, the system switches to a lower velocity for a precise positioning.

The system is self-learning; after the initial run called by the software, the mechanical endpoints are saved within the μC of the MCU. The digitised values from the position sensors can be converted into absolute positions which can be chosen individually from the software interface. The electronics for the control and motion of the motors are separated

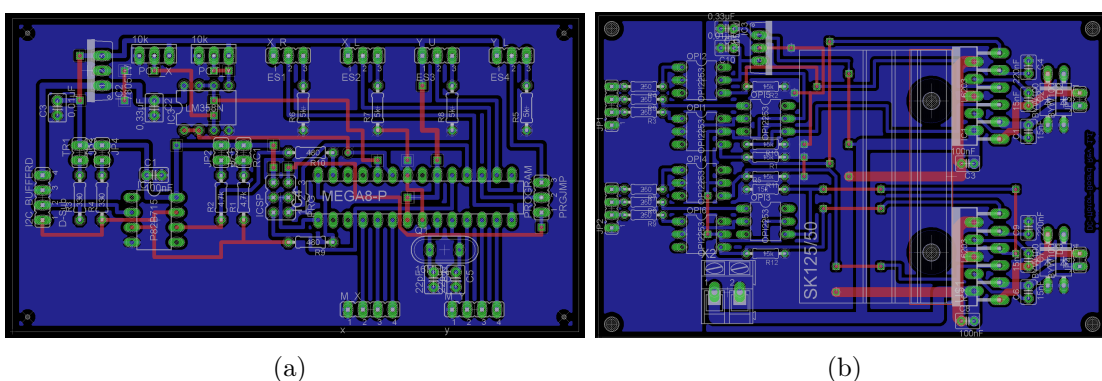


Figure 3.24: Motor Control Board with the control electronic (left) and the power section (right).

into two units. One unit contains the electronics for the readout of the position sensors, the μC and the communication to the central unit which is realised by buffer amplifiers [46]

for the I²C bus and is depicted in figure 3.24(a). The other unit, shown in figure 3.24(b), is electrically isolated from the control unit using opto-insulators. This unit contains the power amplifiers for driving the DC-Motors. Both units are grounded independently and, therefore, the noise produced by driving the motors does not interfere with the electronics used for measurements. The power amplifiers are based on the DMOS full bridge driver L6203 by SGS-Thomson [56] and are passively cooled by an aluminium heat sink.

3.7 Software

Minor variations in the beam position, that lead to major variations in the background contribution can be observed by monitoring the currents on the segments of the aperture and on the target using the interface shown in figure 3.25(a). The position of the target within the x-y-plane can be manipulated in the range of about ± 10 mm with a precision of 0.1 mm using the same interface mentioned above.

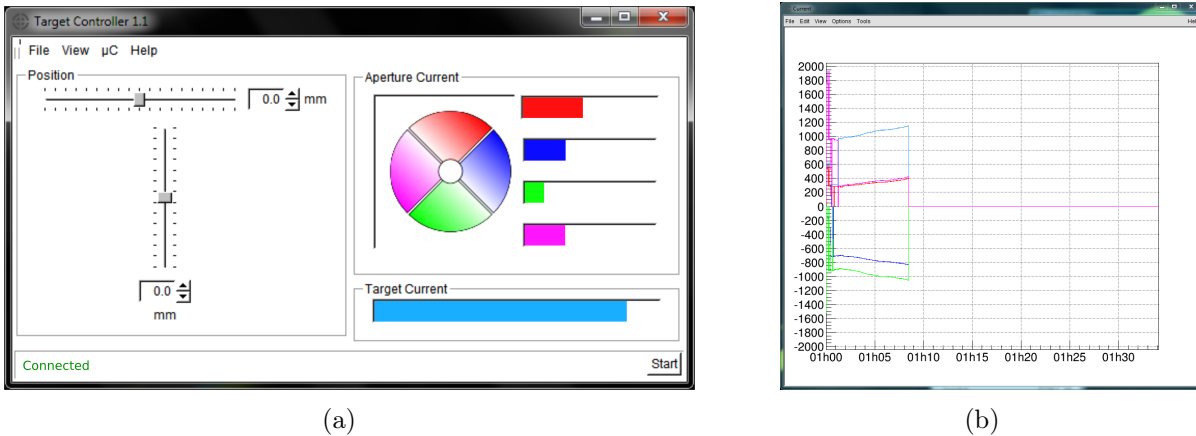
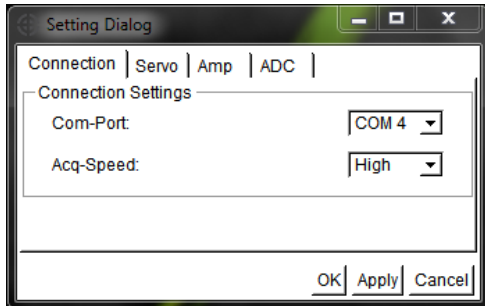


Figure 3.25: (a) Graphical user interface which was developed for recording and monitoring of the target and aperture currents. It allows remote control of the target position. (b) On-line monitoring of the temporal evolution of the currents.

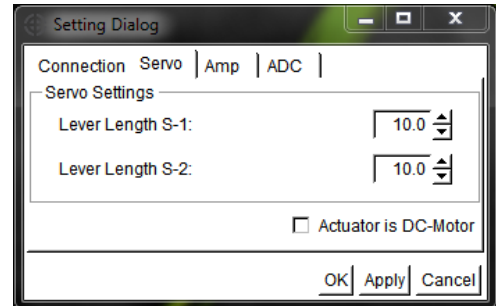
An additional graphical object of the software provides the representation of the currents as functions of the time (see also figure 3.25(b)). The data can be saved in ROOT data containers where the current of each individual aperture and the target are recorded together with the time stamp. The temporal development of the currents are recorded along with that of the γ -energy distribution. In this way, the part of the γ -energy distribution measured with irregular beam position can be separated out.

Hard- and software are prepared for the control of two different actuator systems. The first, more simple actuator system consists of special servomotors which receive the value of the angle as a PWM-coded signal. These actuators are inexpensive and widely available but often have low precision. The software calculates the angle value based on the linear position given by the user in the main interface and the lever length, configured in the Setting Dialog of the software.

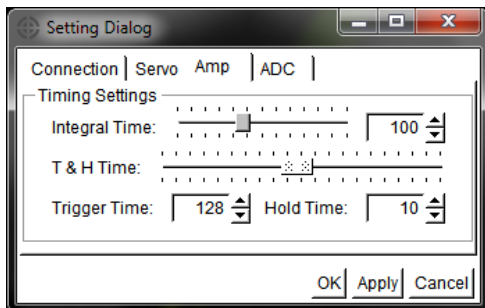
For precise positioning, a system with highly reduced gear DC-motors was developed as described in section 3.5. If this kind of actuators is chosen in the Setting Dialog, the software reconfigures the hardware for the communication with the additional hardware module.



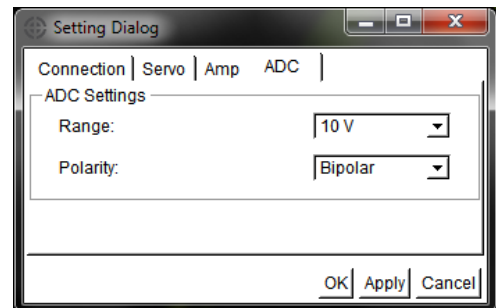
(a) Connection



(b) Actuator



(c) Amplifier



(d) ADC

Figure 3.26: Overview of the settings which allow the configuration of the hardware.

In addition, an interface for the DC-motors was developed and is used for triggering and monitoring of the reference run, where the movable platform is driven to its mechanical end points which were stored along with the zero point in the memory of the μC . The mechanical endpoints are equipped with limit switches connected as normally closed contact for wire breakage protection.

The amplifiers used for the measurement of the aperture currents can be configured in the Amp section of the settings. The height of the output signal and hence, the current range to be measured is adjusted by the integration time which can be set in the range between $10\ \mu\text{s}$ and $10\ \text{ms}$. It is saved as function of the time, which allows the calibration of the amplifiers in dependence on the integration time. The trigger and hold times provide the possibility to remotely configure the length of the plateau and the exact temporal position of the ADC sampling. These values are generally determined once for the combination of the used ADC and communication protocol.

The ADC can also be configured using the graphical user interface where the user can choose between two measurement ranges and uni- or bi-polar operation.

Chapter 4

Measurement

The determination of the stopping power using IDSAM is based on the solution of a Fredholm integral equation of the first kind. As mentioned in section 2.3, two γ -energy spectra have to be measured to obtain the stopping power of the target medium.

It is crucial that these γ -energy spectra are measured with the γ -detector placed at 0° relative to the incoming α -particle beam. Only in that case, the flight angle of the carbon nuclei and the emission angle of the γ -quantum are equal and the measured γ -energy spectra can be transformed into the angular and velocity spectra of the produced $^{12}\text{C}^*$ projectiles.

This chapter describes the measurements performed at the PTB Ion Accelerator Facility (PIAF). A detailed description of the experimental set-up will be given along with the resulting data with a special focus on the recorded γ -energy spectra, background contribution and durability of the carbon layer.

4.1 Unattenuated γ -energy spectra

The experimental set up for the measurement of the unattenuated γ -energy spectra is shown in figure 4.1. The measurement was carried out using the sandwich structured target explained in section 3.4.

To obtain an optimal signal-to-background ratio, several factors have to be taken into account. The most important factor is the α -beam energy. It has to be chosen such that the ratio of the cross section for the production of excited carbon nuclei to that of the γ -ray and neutron background is as high as possible. The cross section for the production of excited carbon projectiles shown in figure 4.2 exhibits a resonance-like structure at α -reaction energy $T_\alpha = 10.2\text{ MeV}$. This resonance-like feature leads to an excellent signal to background ratio, which was experimentally verified in this work.

In case of the water target (see also section 3.4), the α -reaction energy of 10.2 MeV was obtained using the primary α -particle beam energy of 11.57 MeV and a tantalum entrance window $5\ \mu\text{m}$ in thickness. The energy spread *FWHM* of the α -particles after traversing

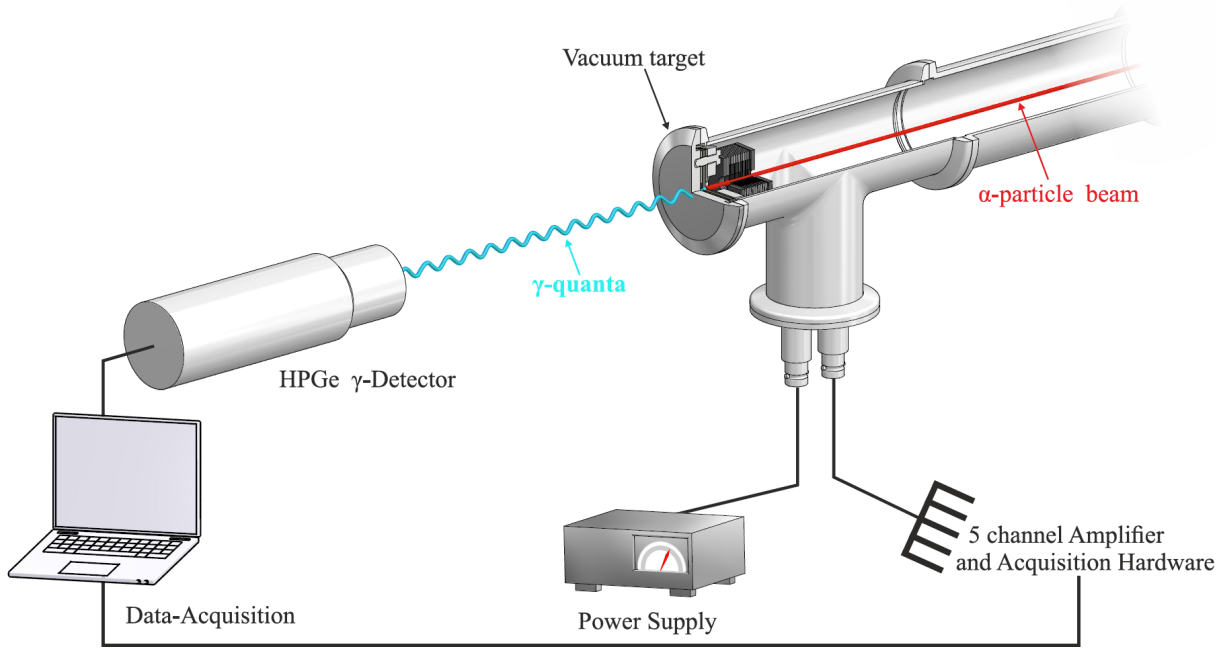


Figure 4.1: Schematic overview of the experimental set up for the measurement of the unattenuated Doppler-shifted γ -energy spectra. The design of the target is given in detail in section 3.4.1.

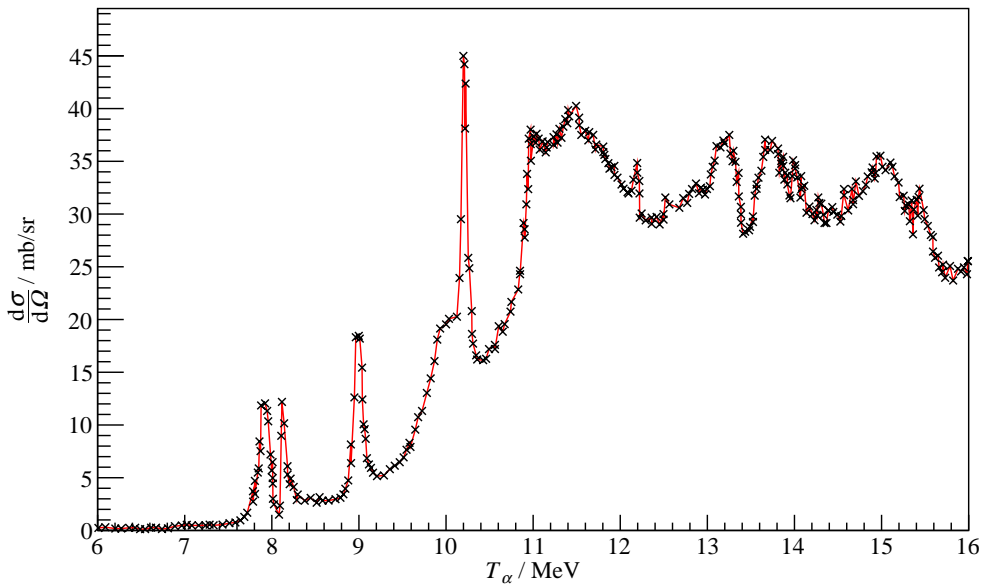


Figure 4.2: Differential cross section for the production of carbon nuclei in their first excited state [57].

the tantalum window amounted to 110 keV according to calculation using Geant4. Due to the energy straggling of the α -particles in the entrance window, the attenuated γ -energy spectra consist of contributions from different beam energies. Therefore, the dependence of the initial velocity distribution of $^{12}\text{C}^*$ projectiles on the α -beam energy has to be investigated. A strong dependence of the velocity distribution is disadvantageous, as

a small change of the α -beam energy, for instance caused by the energy straggling of the α -particle in the entrance window, would lead to a significant uncertainty in the start energy spectrum of the excited carbon nuclei. This dependence was investigated by measuring the unattenuated γ -energy spectra dN_u/dE_γ as function of α -beam energy. For this purpose, measurements were carried out for eight α -beam energies in the range of $T_\alpha = 10.1$ MeV up to 11.95 MeV. As an example, figure 4.3 shows the change of the unattenuated γ -energy spectra with the α -beam energies at around 10.2 MeV.

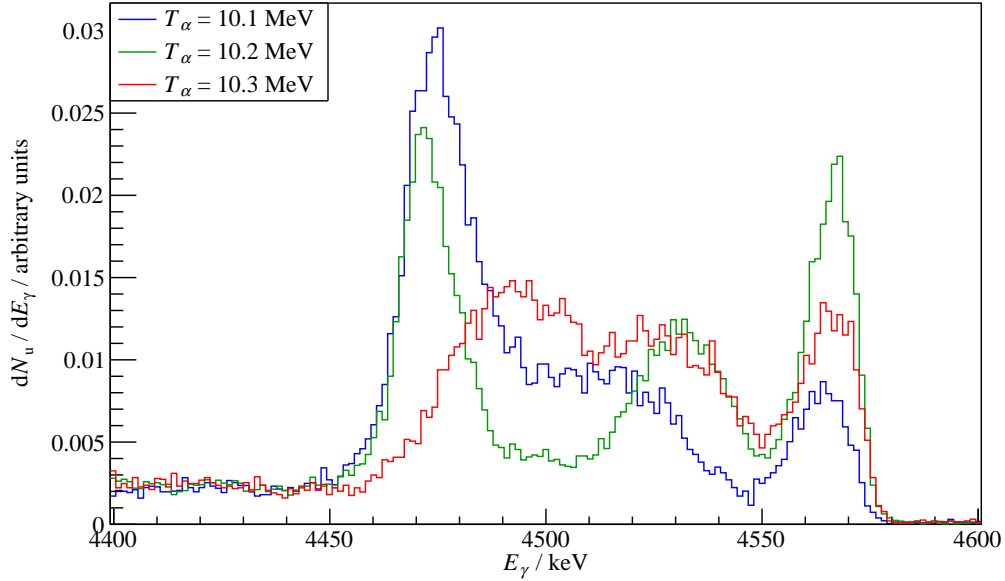


Figure 4.3: Different unattenuated γ -energy spectra contributing to the attenuated spectra due to the energy straggling of incident α -particles in the tantalum entrance window. It can be seen that the shape of the spectrum is strongly sensitive to the α beam energy.

At α -particle energies around the maximum of the cross section at 10.2 MeV, the shape of the unattenuated γ -energy spectra is strongly dependent on the α -beam energy. Due to the great alteration of the $^{12}\text{C}^*$ start energy spectra in dependence of the α -projectile energy, a measurement within the energy interval of $T_\alpha = [10 \text{ MeV}, 11 \text{ MeV}]$ is not favourable.

Only minor changes of the unattenuated γ -energy spectra with the α -beam energy were observed at energies around 11.5 MeV as shown in figure 4.4. It can be seen from figure 4.2 that the cross section for the production of $^{12}\text{C}^*$ nuclei is reasonably high in this energy region [57]. Therefore, the experimental determination of the stopping power of water for ^{12}C ions was carried out using a primary α -beam energy of 12.8 MeV resulting in a mean α -particle energy of 11.57 MeV after the entrance foil. At this energy, it can be ensured that the energy straggling of α -particles in the entrance window has only a negligibly small influence on $d\tilde{N}_u/dE_\gamma$.

The dependence of the spectral shape on the α -particle energy is governed by the spin of the populated state of the compound nuclei in the reaction $^{12}\text{C}(\alpha, \alpha')^{12}\text{C}^*$ and the

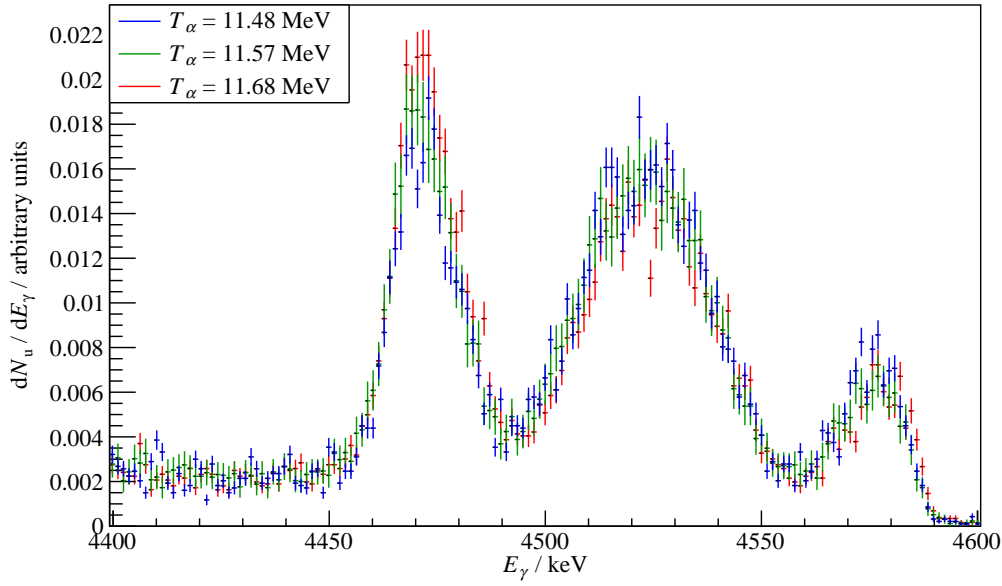


Figure 4.4: Unattenuated γ -energy spectra for the α -beam energies 11.48 MeV, 11.5 MeV and 11.68 MeV. The shape of these spectra show only minor changes.

γ -multiplicity of the emitted γ -quanta. The theoretical explanation of the shape of the unattenuated γ -energy spectra is given in appendix C.

4.2 Attenuated γ -energy spectra

The attenuated γ -energy spectra were measured using the water target described in section 3.4. As described above, excited $^{12}\text{C}^*$ projectiles are produced in the carbon layer coated on the backside of the tantalum entrance window and slow down in the water volume interfacing the carbon layer.

The distance between the water target and the surface of the γ -detector was the same as in the case of the measurement of the unattenuated γ -energy spectra. The position of the water target relative to the α -particle beam position was monitored and adjusted by means of the four-segment aperture. In the first step, the information on the current distribution of the four-segment aperture was used by the operator of the accelerator to align the α -beam. The fine adjustment of the water target was then carried out by activating the target positioning system. This is achieved by driving the moving platform until the beam current is registered on one of the aperture segments. By repetition for all directions in the x - y -plane the zero point can be determined. In this case the beam incidents at the centre of the target without scattering at the apertures leading to the highest possible signal-to-noise ratio. The beam current of the four-segmented aperture, the target current and the integration time set in the soft-/hardware are saved as a function of time in *ROOT* data containers for later analysis.

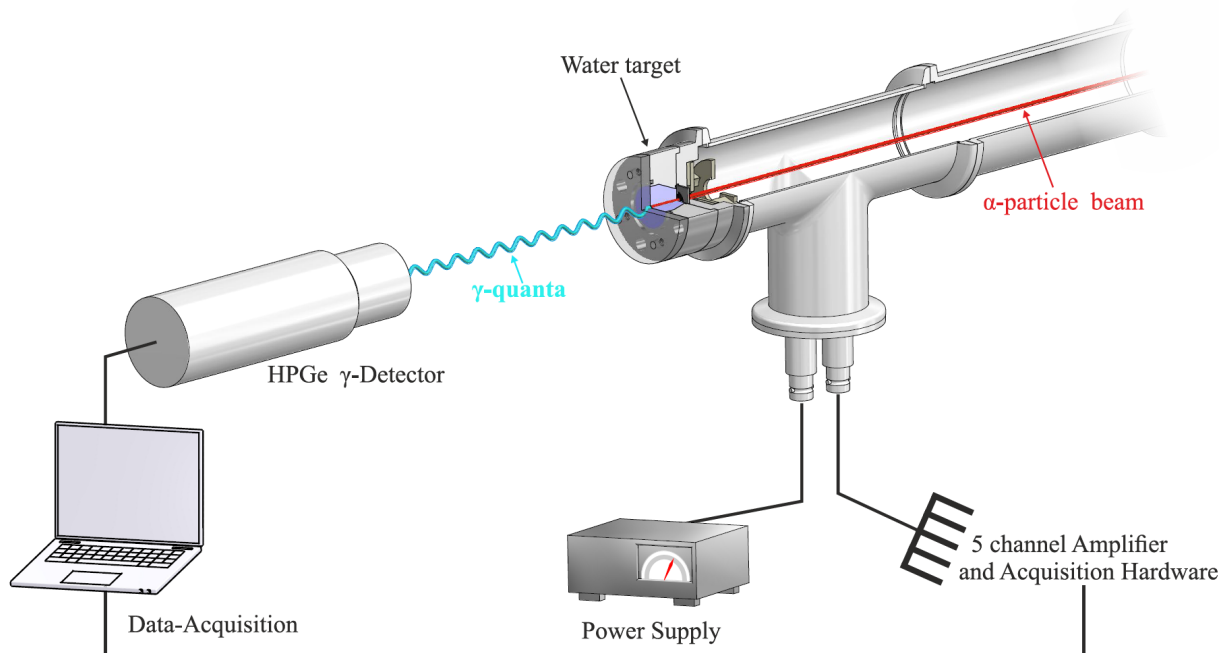


Figure 4.5: Experimental set up for the measurement of the attenuated γ -energy spectra using the water target. The distance between the detector and the target surface was 378 mm. The design of the target is given in detail in section 3.4.2.

To obtain the mean α -energy of 11.57 MeV in the carbon layer, the initial α -beam energy was set to 12.8 MeV. The spectra of α -particle energies after traversing the tantalum entrance window $5 \mu\text{m}$ in thickness, calculated using a Geant4 simulation, is shown in figure 4.6. An example of the optimisation of the target position relative to the α -

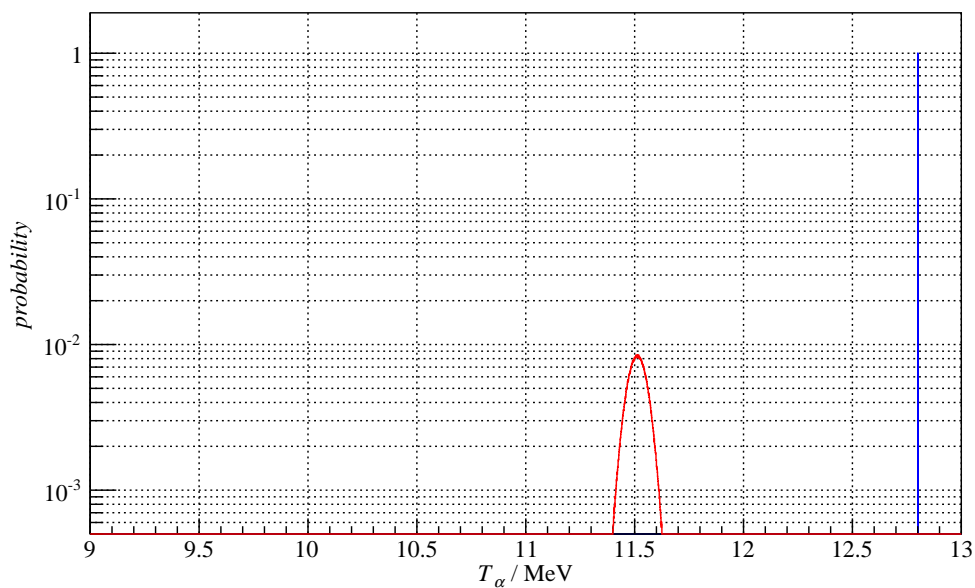


Figure 4.6: Energy spectra (red curve) of α -particles after traversing a tantalum foil with a thickness of $5 \mu\text{m}$ with a mean value located at 11.51 MeV. The blue line indicates the primary beam energy of 12.8 MeV.

beam is shown in figure 4.7. In both γ -energy spectra, the full absorption, single, and double escape peak of the oxygen line arising due to the decay of $^{16}\text{O}^*$ from the second excited to its ground state can be seen. Excited $^{16}\text{O}^*$ nuclei are produced by the reaction $^{16}\text{O}(\alpha, \alpha')^{16}\text{O}^*$. At energies around 4.5 MeV, the built-up of the Doppler-shifted γ -energy spectra from the excited carbon nuclei can be recognized. If the beam position is not optimally adjusted, a strong increase of count rates at energies below 3.5 MeV is observed. As they show no typical structures which were expected for γ -interactions with the detector material, they most likely arise from neutrons produced by the scattering of the beam at the aperture and then hitting the aluminium housing of the water target.

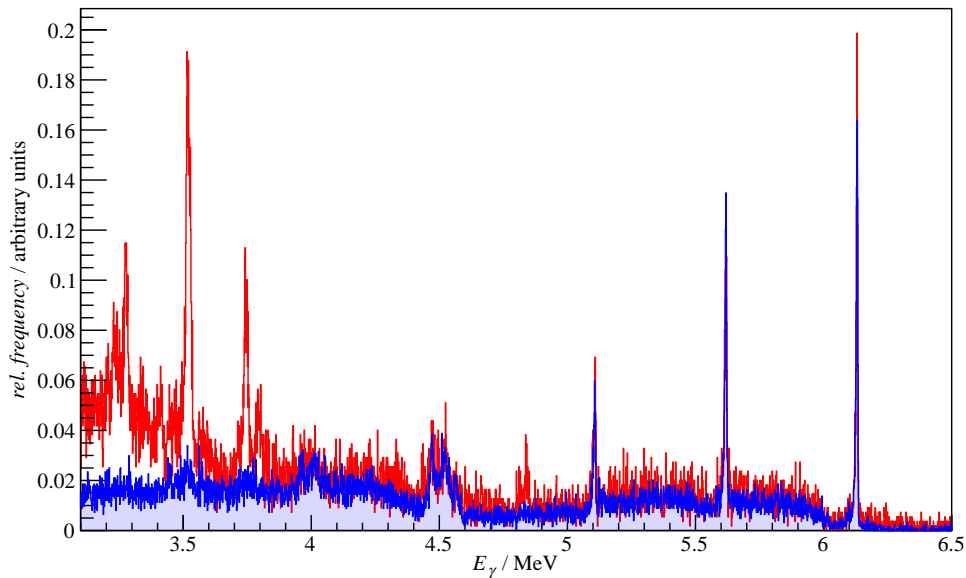


Figure 4.7: Attenuated γ -energy spectrum (red) which was recorded directly after the beam was focused and positioned using the beam-guiding instruments of the accelerator in comparison to that obtained after the optimisation of the beam position using the target positioning system developed in this work. Both spectra were normalised such that the area of the full absorption peak of oxygen is unity.

As it can be seen from figure 4.7, the abnormal structures at γ -energies around 3.5 MeV vanished after the optimisation of the beam position and the structure at about 4.5 MeV is more pronounced. This reduction of background was achieved by only minor corrections of the target position in the order of 0.2 mm which could be achieved much faster with the developed system than with the beam optics of the accelerator. After the optimisation of the target position, the attenuated γ -energy spectra were measured. The cumulative attenuated γ -energy spectrum after about 50 h with a beam current of about 30 nA is shown in figure 4.8. The attenuated γ -energy spectra are mainly interfered by the Compton-continuum of the oxygen line. As the Compton-continuum alters the shape of the attenuated γ -energy spectrum, it must be subtracted. The procedure applied to determine the energy-dependent background and its subtraction is given in more detail

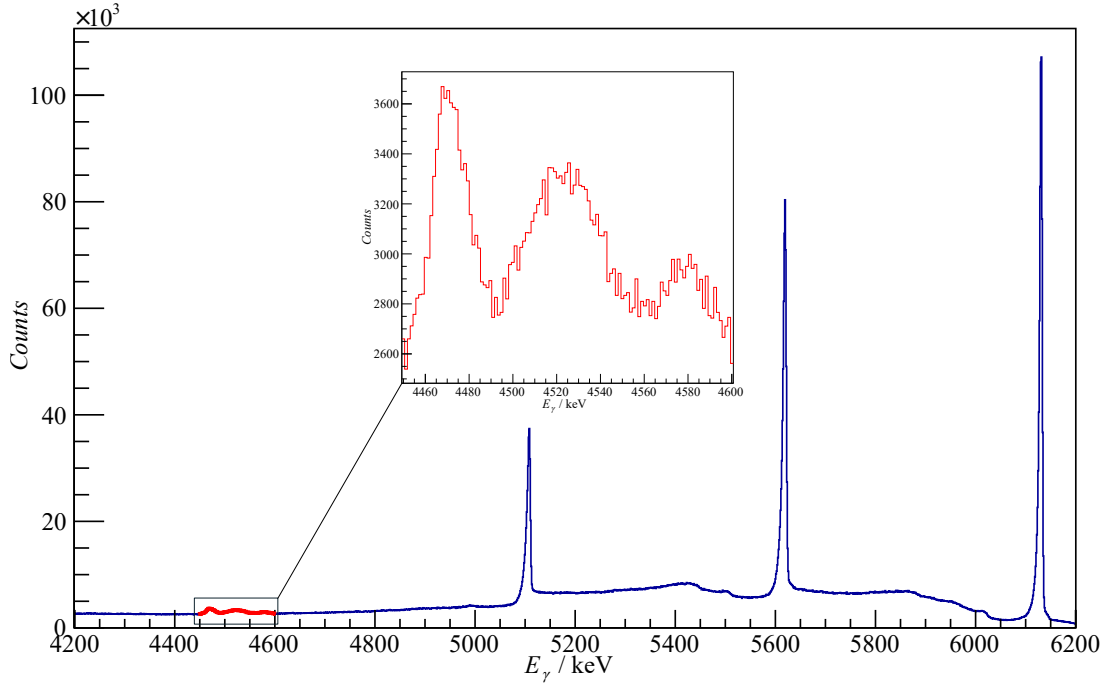


Figure 4.8: γ -energy spectrum after a measurement time of about 50 h. The α -beam current was about 30 nA. The spectrum in the in-box shows the attenuated Doppler-shifted γ -energy spectrum $d\tilde{N}_a/dE_\gamma$ of carbon nuclei decaying while being decelerated in water.

in section 5.1.

The use of the primary α -beam energy of 12.8 MeV leads to a decrease of the signal-to-noise ratio by a factor of ten compared to the primary α -beam energy of 11.57 MeV. This deterioration of the signal-to-noise ratio is mainly caused by the increased cross section of the reaction $^{16}\text{O}(\alpha, \alpha')^{16}\text{O}^*$ which is shown in figure 4.9. This cross section is increased by a factor of ten between an α -particle beam energy of 10.2 MeV and an α -particle beam energy of 11.51 MeV.

4.3 Durability of the carbon layer

For a stable measurement, the durability of the carbon layer is important as the exchange of the carbon layer is only possible through the detachment of the target system from the beam line. The heating of the tantalum entrance window due to the energy deposition by α -particles can cause water convection on the surface of the tantalum foil, potentially leading to a de-collation of the carbon layer. As mentioned in section 3.4.4, several carbon coating methods have been checked with respect to the de-collation behaviour during the measurement.

The best stability was achieved when coating the entrance window by means of ion beam deposition [76] producing a DLC coating. For the other two, the carbon layers were de-collating from the substrate.

The effective thickness of the carbon layer can be quantified by means of the count

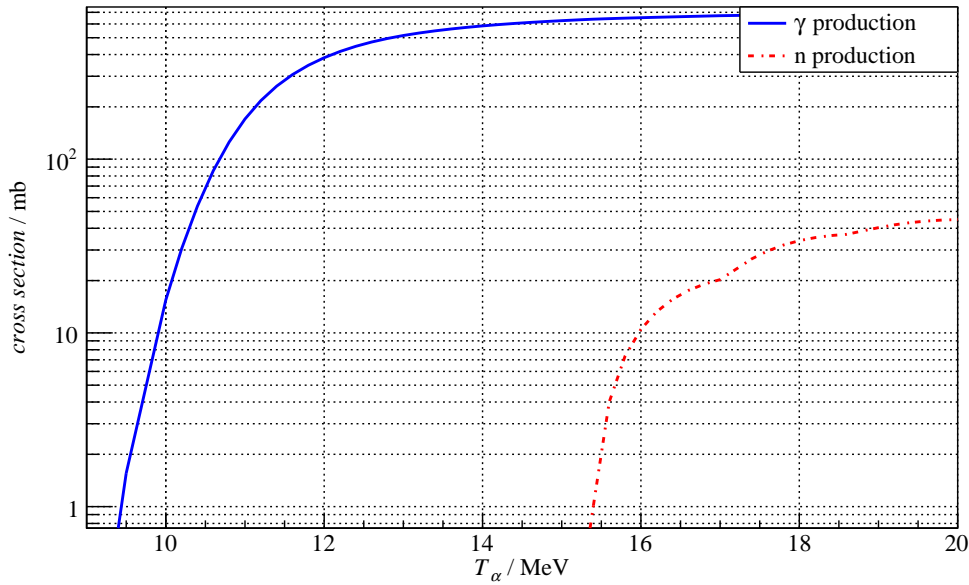


Figure 4.9: Cross section for the production of oxygen in the second excited state and for the neutron production by α -particles colliding with oxygen in dependence of the α -beam energy T_α calculated with TALYS [48].

rate in the attenuated γ -energy spectra in relation to the count rate in the full absorption peak of the oxygen line, as this quantity is proportional to the number of α -particles traversing the entrance window.

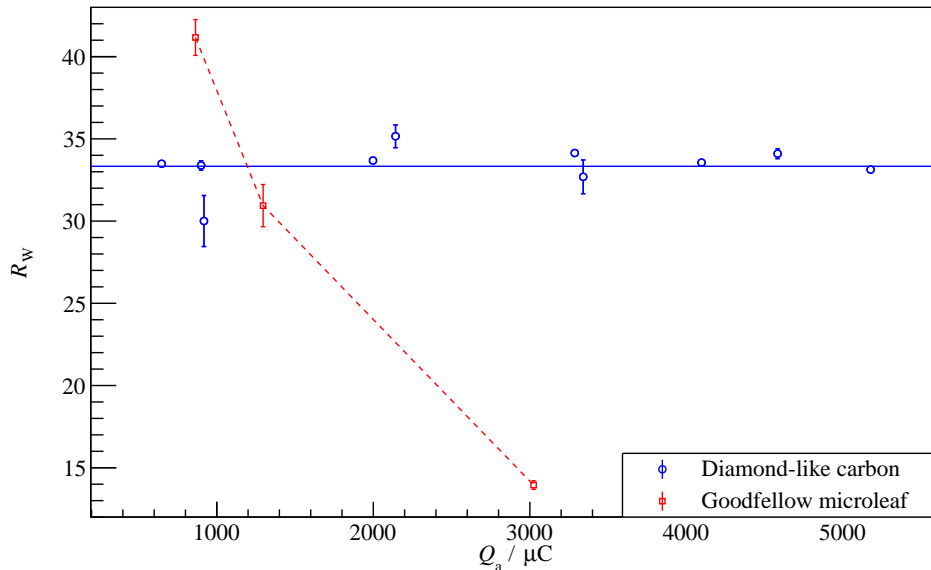


Figure 4.10: Ratio R_W of the integral counts in the attenuated γ -energy spectra in the energy range between 4.46 MeV and 4.59 MeV normalised to the area of the full absorption peak of the oxygen line as function of the accumulated charge Q_a for two carbon coating methods.

Figure 4.10 shows the ratio of the counts in the attenuated γ -energy spectra of decaying $^{12}\text{C}^*$ nuclei (integrated between 4.46 MeV and 4.59 MeV) to the area of the full

absorption peak of the oxygen line for two carbon coating methods. It can be seen from figure 4.10 that no decrease of the ratio can be observed in the case of the DLC coating produced by the accelerator-based ion deposition. On the contrary, the carbon layer produced with carbon micro-leaves shows a steep decrease during the measurement.

Chapter 5

Instrumentation effects

The experimental γ -energy spectra are influenced by several instrumentation factors. The recorded γ -energy spectra are superimposed by a background that mainly arises due to the Compton tail of energetically higher lying γ -lines. Additionally, they are broadened due to the finite energy resolution of the detection system. In the present work, the angle of the acceptance of the γ -detector amounted to $\pm 6^\circ$. Due to this finite opening angle of the detector, the detection angle of the γ -quanta is not sharply defined. In other words, the γ -quanta, whose emission angle is different from the flight angle of $^{12}\text{C}^*$ projectile, can also be detected, causing an additional broadening of the γ -energy spectra. Moreover, this effect leads to the violation of the unique relation between the γ -energy and the flight angle, required to obtain the flight angle spectra of the $^{12}\text{C}^*$ projectiles from the unattenuated spectra. The n-type detector used in this work has a bore hole in the centre so that the effective detector thickness and, consequently, the detection efficiency changes with the point of the incidence of the γ -quantum. In the following, the procedure of the background subtraction and the broadening of the γ -energy spectra due to the finite energy and angular resolution of the detector are described, taking into account the position-dependent detection efficiency.

5.1 Background correction

As described above, the background in the attenuated spectra mainly arises from the Compton continuum of the oxygen line. It is assumed that the Compton continuum of the oxygen line can be represented by an exponential function with four free parameters:

$$f_{\text{B}}(C) = a + b \exp \left[\frac{E_{\gamma} - C_0}{c} \right]. \quad (5.1)$$

The parameters in equation 5.1 were determined by means of the best fit of the equation to the experimental data between 4.59 MeV and 4.95 MeV, where the energy 4.59 MeV is the upper limit of the attenuated γ -energy spectra. The results of the best fit are listed

in table 5.1. Due to the statistical fluctuations of the experimental data, the parameter values are subject to rather high uncertainties. The results of the best fit is shown

Parameter	Value	Uncertainty
a	1054.63 keV ⁻¹	44.92 keV ⁻¹
b	256.84 keV ⁻¹	182.50 keV ⁻¹
C_0	7133.51 keV	39.37 keV
c	466.99 keV	39.37 keV

Table 5.1: Parameters determined by the best fit in the range of $4.590 \text{ keV} \leq E_\gamma \leq 4950 \text{ keV}$.

in figure 5.1(a). It can be assumed that the Compton continuum of the unattenuated and attenuated γ -energy spectra below $E_0 = 4.438 \text{ MeV}$ are equal in first order. This was used to check the correctness of the background subtraction. Figure 5.1(b) shows

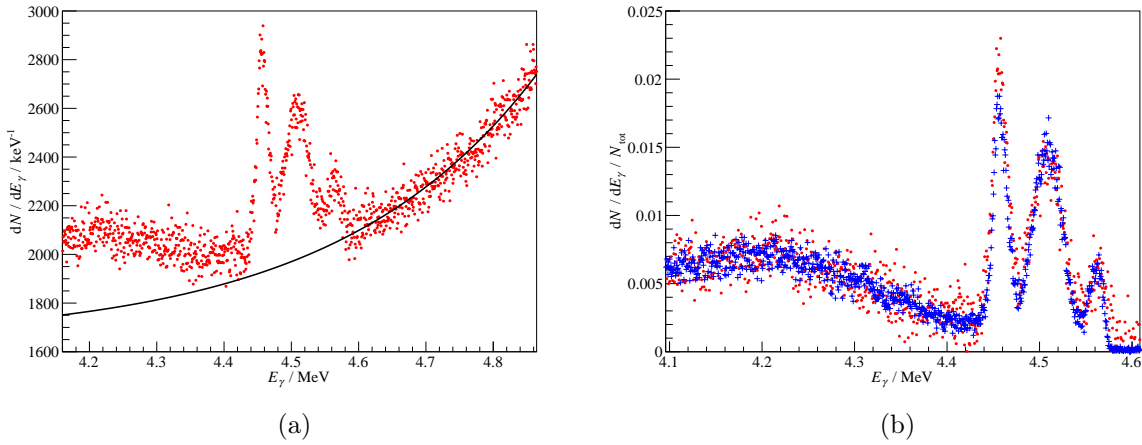


Figure 5.1: (a) Background arising due to the Compton tail of the oxygen line and the result of the best fit of equation 5.1 to the measured data. (b) Background-corrected attenuated γ -energy spectra (red) together with the unattenuated spectra (blue). The Compton-continua of both spectra are in good agreement.

both γ -energy spectra with Compton continua after the background subtraction. For comparison the integral of both γ -energy spectra was normalised to unity. As it can be seen, the Compton-continua of both γ -energy spectra are in good agreement.

5.2 System response function

The system response function can be obtained using a γ -source with an emission energy in the vicinity of the region of interest. This is provided by the γ -line of ^{66}Zn located at $E_\gamma = 4.8066 \text{ MeV}$. The energy is slightly higher than the energies of the region of interest. Nevertheless, the line of ^{66}Zn was used for the system response function as the calculation of the detector efficiency by Monte Carlo simulation [13] revealed that the variation of the detector response with E_γ , i. e. the ratio of the full absorption peak to the Compton continuum, is negligibly small.

The γ -source ^{66}Zn was produced by bombarding a solid copper target with α -particles with an energy of $T_\alpha = 20$ MeV. The nuclei ^{66}Ga , produced via the reaction $^{63}\text{Cu}(\alpha, n)^{66}\text{Ga}$, decay with a half-life of 9.49 h by β^+ -decays or electron capture processes. In 1.84 % of the cases it decays to the excited state of ^{66}Zn which subsequently decays to the ground state by emission of a γ -quantum of $E_\gamma = 4.8066$ MeV. The mean cross section for the production of ^{66}Ga is given by:

$$\bar{\sigma}_{\text{Ga}} = \int_{T_\alpha(\sigma=0)}^{T_{\alpha,0}} P(\sigma_{\text{Ga}}(T'_\alpha), x(T'_\alpha)) \frac{d\sigma_{\text{Ga}}}{dT_\alpha}(T'_\alpha) dT'_\alpha \quad (5.2)$$

where $T_{\alpha,0}$ is the primary energy of the α -particles and $P(\sigma_{\text{Ga}}(T_\alpha), x(T_\alpha))$ considers the beam attenuation in the target:

$$P(\sigma_{\text{Ga}}(T_\alpha), x(T_\alpha)) = \exp[-\sigma_{\text{Ga}}(T_\alpha)nx(T_\alpha)] , \quad (5.3)$$

with n denoting the number density of the target atoms.

The cross-section $d\sigma_{\text{Ga}}/dT_\alpha(T_\alpha)$ is available either in form of tables or can be calculated using programs such as TALYS [48].

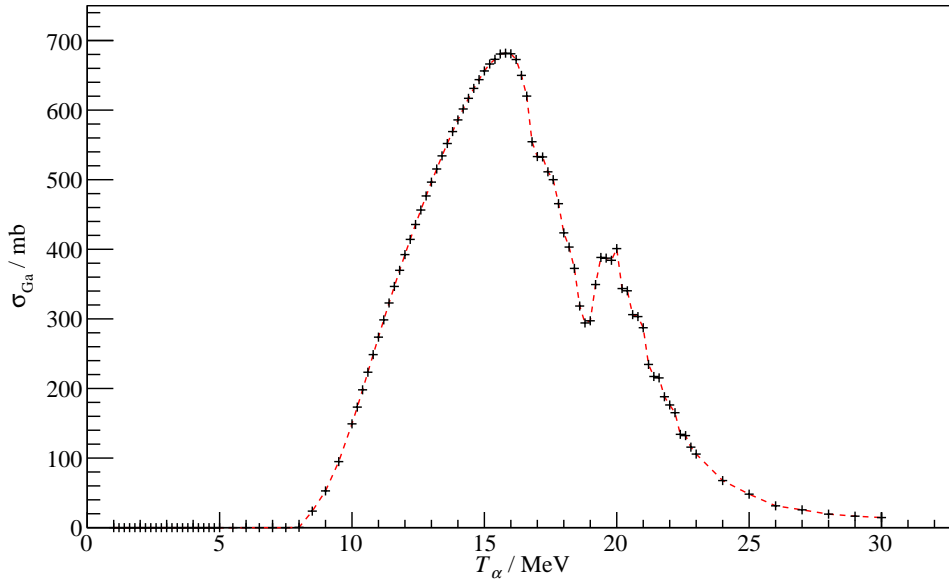


Figure 5.2: Cross section for the production of ^{66}Ga by bombardment of natural copper with α -particles as function of the α -particle energy T_α calculated using TALYS 1.6.

The production rate \dot{N}_{Ga} of ^{66}Ga was estimated using the mean cross section $\bar{\sigma}_{\text{Ga}}$ amounting to

$$\dot{N}_{\text{Ga}} = n \frac{I_\alpha}{2e} \bar{\sigma}_{\text{Ga}} d_{\text{Cu}} , \quad (5.4)$$

where I_α is the α -beam current which was about 10 nA and e is the elementary charge.

The effective thickness of the target d_{Cu} is obtained by the calculation of the depth in the target where the energy of the α -particle falls below the threshold energy of ^{66}Ga production. This production rate results in an activity of 324 kBq for the decay of ^{66}Ga to ^{66}Zn after one hour of bombardment. Due to the branching ratio of 1.84 %, the γ -ray count rate in a solid angle of 4π in the energy region of interest amounts to $5.96 \cdot 10^4 \text{s}^{-1}$. By considering the half time of the source, the geometry and the full absorption efficiency of the detector ($\approx 6.8\%$ [13]), the expected number of counts in the full absorption peak after a measurement of about 2.5 h would provide a sufficient count statistics of about 14500 counts in the peak (measured 12522 counts).

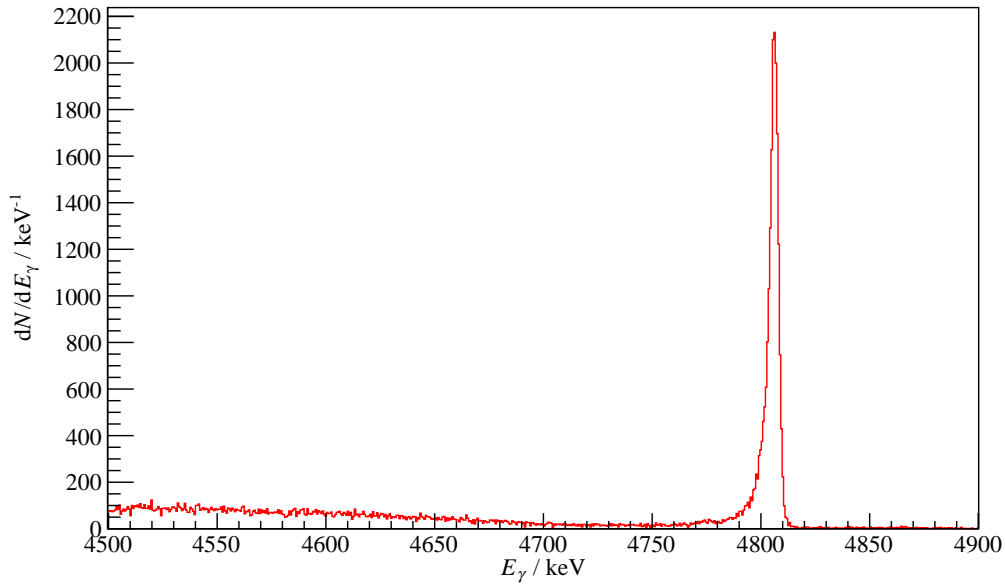


Figure 5.3: System response function recorded for $t = 2.41$ h. The integral value of the full-absorption peak gives 12522 counts. The asymmetric tailing is a property of the detector used and is caused by incomplete charge collection.

The system response function can be obtained by the normalisation of the area of the γ -energy spectra of ^{66}Zn shown in figure 5.3 to unity:

$$A(E_\gamma; E_{\gamma,0}) = \frac{dN}{dE_\gamma} \left(\int \frac{dN}{dE'_\gamma} dE'_\gamma \right)^{-1}, \quad (5.5)$$

where E_γ is the detected energy and $E_{\gamma,0}$ is the energy of the ^{66}Zn γ -line.

As it was mentioned above, Monte Carlo simulations of the detector response have been carried out for a number of γ -energies in the range relevant for this work. The simulations showed that the relative shapes of the full absorption peak and of the Compton continuum vary only negligibly with the energy of the primary γ -quanta. The energy separation between the Compton edge and the full absorption peak varies only from 241.5 keV to 242.6 keV for γ -quantum energies between 4.4 MeV and 4.8 MeV. Therefore, the approximation that the system response function depends only on the difference between

the γ -quantum energy $E_{\gamma,0}$ and the detected energy E_γ

$$A(E_\gamma; E_{\gamma,0}) = A(E_\gamma - E_{\gamma,0}) \quad (5.6)$$

will only introduce a negligible uncertainty contribution. The system response function can be taken from the measurement shown on figure 5.3.

5.3 Angular resolution

Due to the finite solid angle caused by the experimental set up, the γ -quantum emitted at an angle φ , which is not equal to the flight angle ϑ of the $^{12}\text{C}^*$ projectile, can be detected. In other words, γ -quanta emitted at different angles and, hence different energies, could belong to one flight angle of a $^{12}\text{C}^*$ projectile. As the equality $\varphi = \vartheta$ is required to uniquely transform the unattenuated γ -energy spectra dN_u/dE_γ into the start velocity spectra $W(v_0)$ of the $^{12}\text{C}^*$ projectiles, the finite energy spread due to the angular resolution of the detector has to be deconvoluted from the measured spectra $d\tilde{N}_u/dE_\gamma$.

In order to perform the deconvolution, the broadening function $G(\vartheta, \varphi)$ due to the finite detection angle has to be known. It can be obtained by the geometrical intersection of the γ -quanta emission cone and the detector front surface, where the origin of the cone is given by the position of the γ -source, the target. The cone axis is given by the flight angle ϑ of the $^{12}\text{C}^*$ projectile and its opening angle is defined by the emission angle φ of the γ -quantum (see also figure 5.4). The energy spread can be calculated on the basis of

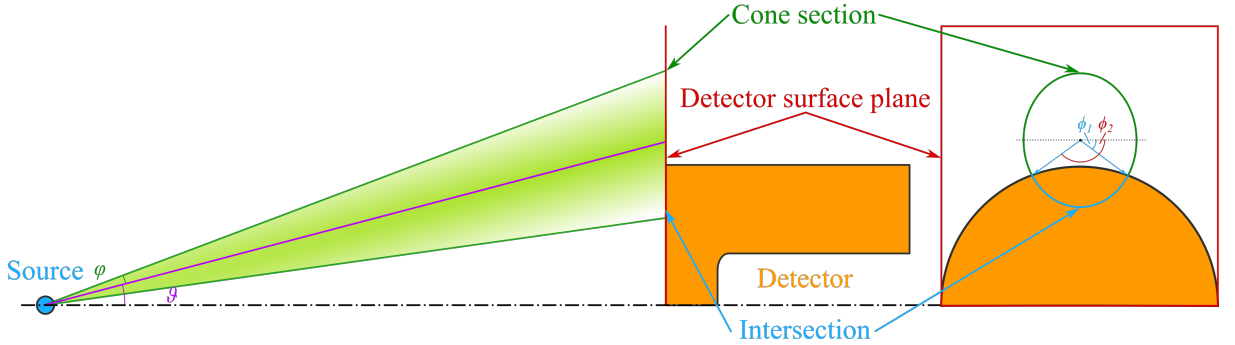


Figure 5.4: Sketch of the cone built by the flight angle ϑ of the $^{12}\text{C}^*$ projectiles and the γ -emission angle φ that defines the opening angle of the cone. The frontal view shows cone section in form of an ellipse on the detector surface plane.

a geometrical function which can be expressed by

$$G(\vartheta, \varphi) = a(\vartheta, \varphi) \int_{\phi_1}^{\phi_2} \eta_{\text{F}}(r(\phi')) \sqrt{1 - \varepsilon^2(\vartheta, \varphi) \sin^2 \phi'} d\phi' \quad (5.7)$$

where $a(\vartheta, \varphi)$ is the major semi-axis and $\varepsilon(\vartheta, \varphi)$ is the eccentricity of the ellipse formed by the intersection of the γ -quanta emission cone and the surface plane of the detector

which are parametrised by the flight angle ϑ of the $^{12}\text{C}^*$ projectile and the emission angle φ of the γ -quanta (see also figure 5.4). The integration is carried out over the angle interval $[\phi_1, \phi_2]$ around the centre of the ellipse in the interval where the ellipse is within the circular detector front area.

The explicit mathematical derivation of the formalism used in this work is given in appendix B.

In equation 5.7 the integration is weighted with the detection efficiency $\eta_F(r)$ which is taken to be radially symmetric. The reason for this is that in the case of an n-type coaxial detector as used in this work, the efficiency is reduced in the centre of the detector due to a bore hole.

Therefore, the probability of a full absorption is dependent on the radial coordinate and the angle of the incidence of the γ -quantum onto the detector.

If the detector is far away from the source, it can approximately be assumed that the incidence angle of the γ -quantum is perpendicular to the detector surface. In this case, the full absorption efficiency $\eta_F(r)$ is only a function of the radial distance from the detector centre r :

The function $\eta_F(r)$ was calculated [13] by means of simulation using EGSnrc [47] and is shown in figure 5.5.

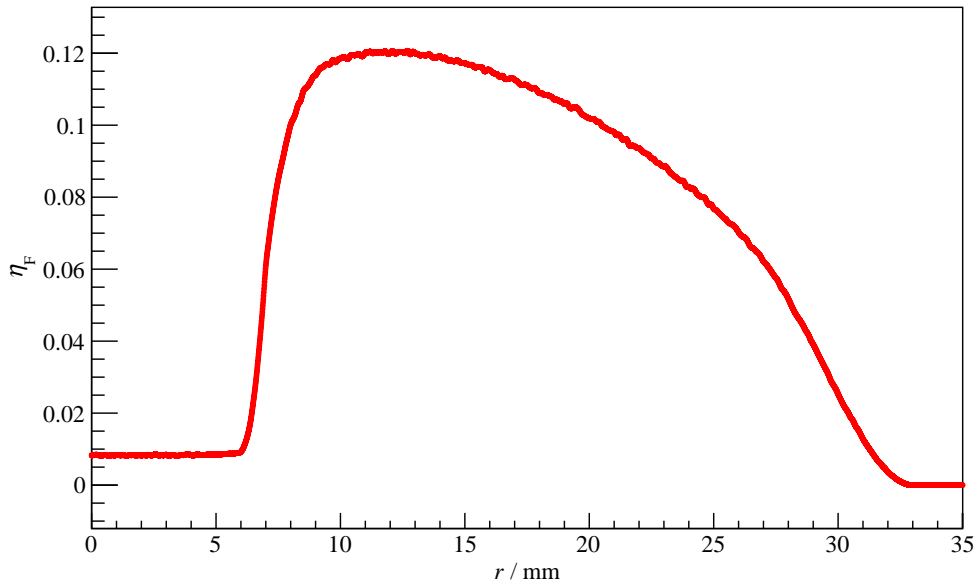


Figure 5.5: Radial-dependent detection efficiency calculated by Bittner [13] using EGSnrc.

Chapter 6

Data evaluation

This section deals with the derivation of the equations required for the data evaluation and describes how the instrumental effects influence the measured γ -energy spectra.

This section also describes the deconvolution of the unattenuated and attenuated γ -energy spectrum from the energy spread arising due to finite energy and angular resolution of the detector system. Two common deconvolution methods are briefly introduced and applied.

6.1 Experimental unattenuated γ -energy spectra

As described above, the system response function of the detector was experimentally determined by means of the γ -lines of ^{66}Zn . In the scope of this work, it can be assumed to be independent of the γ -energy and has a functional form of $A(E_\gamma - E'_\gamma)$.

In general, the function $B(E_\gamma, E'_\gamma)$ that describes the broadening of the γ -energy spectra due to the finite opening angle of the detector, can be obtained by summing up the detection probability function $\varrho(\vartheta, \varphi)$ over all the combinations of φ and ϑ resulting in the same γ -energy:

$$B(E_\gamma, E'_\gamma) = \iint_{D(v_0(\vartheta), \varphi) = E'_\gamma} \varrho(\vartheta, \varphi) d\vartheta d\varphi. \quad (6.1)$$

Equation $D(v_0(\vartheta), \varphi) = E'_\gamma$ defines the iso energy line in the two dimensional integration domain along which ϑ and φ result in E'_γ and denotes the Doppler equation where the start velocity v_0 is determined by the flight angle of the $^{12}\text{C}^*$ projectile, $v_0 = f(\vartheta)$. The broadening due to the finite opening angle of the detector is dependent on the flight angle ϑ of $^{12}\text{C}^*$ projectiles and therefore on the γ -energy. If the γ -energy spectrum is unfolded from the broadening due to the finite detector opening angle, the result is a γ -energy spectrum that would be obtained for φ being equal to ϑ .

In the present experiment, E_γ is a unique function of ϑ . Therefore, the integral on

the right hand side of equation 6.1 can be simply represented by a transformation of the function $G(\vartheta, \varphi)$, given in section 5.3, into energy space. It should be noted that the function $G(\vartheta, \varphi)$ includes the radially dependent detection efficiency. The derivation of the function $G(\vartheta, \varphi)$ is described in detail in Appendix B. A graphical representation of

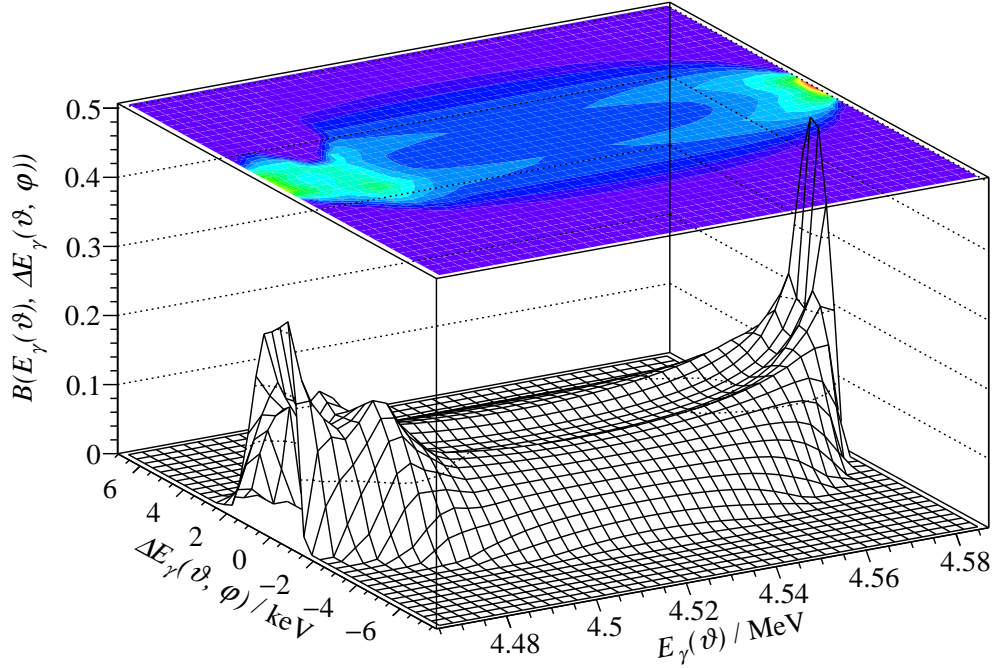


Figure 6.1: Energy spread due to finite detection angle: Graphical representation of equation 6.1.

the function $B(E_\gamma, \Delta E_\gamma)$, with the corresponding γ -energy shift $\Delta E_\gamma = E'_\gamma - E_\gamma$, is shown in figure 6.1.

The measured unattenuated γ -energy spectra $d\tilde{N}_u/dE_\gamma$ can be represented as a two-fold convolution of the true unattenuated spectra dN_u/dE_γ with the resolution functions $A(E_\gamma - E'_\gamma)$ given in equation 5.5 and $B(E_\gamma, E'_\gamma)$:

$$\frac{d\tilde{N}_u}{dE_\gamma} = \int A(E_\gamma - E'_\gamma) dE'_\gamma \int \frac{dN_u}{dE''_\gamma}(E''_\gamma) B(E'_\gamma, E''_\gamma) dE''_\gamma. \quad (6.2)$$

6.2 Experimental attenuated γ -energy spectra

The embedding of the function $G(\vartheta, \varphi)$ into the attenuated γ -energy spectrum is more complicated than in the case of the unattenuated γ -energy spectrum. In contrast to the unattenuated γ -energy spectrum, the γ -energy in the attenuated γ -energy spectrum cannot be uniquely assigned to a flight angle ϑ because the counts at a given γ -energy in the attenuated γ -energy spectrum consist of the contribution from slowing down $^{12}\text{C}^*$

projectiles with different flight angles and, hence, start velocities. The information on the contribution from $^{12}\text{C}^*$ projectiles with different flight angles can be obtained if the stopping power of the target medium is exactly known. In other words, the function $G(\vartheta, \varphi)$ can be converted to a convolution function $C(E_\gamma, E'_\gamma)$ on the γ -energy axis:

$$\int \frac{dN_a}{dE_\gamma}(E_\gamma)C(E_\gamma, E'_\gamma)dE_\gamma = \iint_{D(v_0(\vartheta), \varphi)=E'_\gamma} G(\vartheta, \varphi)W(\vartheta) \times g(v) \exp \left[- \int_{v(E'_\gamma, \varphi)}^{v_0(\vartheta)} g(u)du \right] d\vartheta d\varphi \quad (6.3)$$

The problem is, however, that the function

$$g(u) = \frac{m}{\tau S}$$

is not known at this stage as the stopping power S is just the quantity to be determined. Although $C(E_\gamma, E'_\gamma)$ could be determined iteratively, it was approximately determined using the stopping power of water for carbon ions calculated by means of SRIM2013 [99]. As the term $C(E_\gamma, E'_\gamma)$ itself is a correction term, the effect of the approximation on the uncertainty of the stopping power used in this approach is only of second order.

Once the function $C(E_\gamma, E'_\gamma)$ is known, the measured attenuated γ -energy spectra $d\tilde{N}_a/dE_\gamma$ can be expressed by:

$$\frac{d\tilde{N}_a}{dE_\gamma}(E_\gamma) = \int A(E_\gamma - E'_\gamma)dE'_\gamma \int \frac{dN_a}{dE''_\gamma}(E''_\gamma)C(E'_\gamma, E''_\gamma)dE''_\gamma. \quad (6.4)$$

6.3 Deconvolution

As the γ -energy spectra were measured in discrete channels, equation 6.2 can be expressed by

$$\underline{y}_u = \underline{\underline{M}}_B^A \cdot \underline{x}_u \quad (6.5)$$

where the vectors \underline{x}_u and \underline{y}_u represent dN_u/dE_γ and $d\tilde{N}_u/dE_\gamma$, respectively. The matrix $\underline{\underline{M}}_B^A = \underline{\underline{M}}_A^T \times \underline{\underline{M}}_B$ contains the matrices $\underline{\underline{M}}_A$ and $\underline{\underline{M}}_B$ which stand for the system response function $A(E_\gamma - E'_\gamma)$ and the angular resolution function $B(E_\gamma, E'_\gamma)$ of the detector system, respectively.

Analogous to the unattenuated γ -energy spectrum, the vectorial form of equation 6.4 can be written as:

$$\underline{y}_a = \underline{\underline{M}}_C^A \cdot \underline{x}_a, \quad (6.6)$$

where \underline{y}_a and \underline{x}_a are the discrete representation of the measured attenuated γ -energy spectrum $d\tilde{N}_a/dE_\gamma$ and of the true attenuated γ -energy spectrum dN_a/dE_γ , respectively.

If the matrices $\underline{\underline{M}}_{\text{B}}^{\text{A}}$ and $\underline{\underline{M}}_{\text{C}}^{\text{A}}$ were regular so that their inverses exist, the true γ -energy spectra could be obtained by:

$$\begin{aligned} \underline{x}_{\text{u}} &= \left(\underline{\underline{M}}_{\text{B}}^{\text{A}} \right)^{-1} \cdot \underline{y}_{\text{u}}, \\ \underline{x}_{\text{a}} &= \left(\underline{\underline{M}}_{\text{C}}^{\text{A}} \right)^{-1} \cdot \underline{y}_{\text{a}}. \end{aligned} \quad (6.7)$$

However, these matrices are usually not regular and cannot be inverted uniquely. The determination of the so-called pseudo-inverse often leads to singularities and therefore to large errors when involving high-dimensional matrices.

For the deconvolution of spectra involving a matrix with a deficient rank, there are several approaches available. One approach is the *boosted Gold-Deconvolution* which is based on the algorithm of Raymond Gold published in 1964 [36]. The resulting vector \underline{y} of a measurement can be written as:

$$\underline{y} = \underline{\underline{M}} \underline{x}, \quad (6.8)$$

where \underline{x} represents the true spectrum and $\underline{\underline{M}}$ is the matrix representation of the system response.

The boosted Gold-deconvolution technique is an iterative method where the vector elements of the k -th iteration can be calculated according to [36]:

$$x_i^{(k+1)} = \frac{y'_i}{\sum_{j=0}^{N-1} m'_{ij} x_i^{(k)}} x_i^{(k)} \quad (6.9)$$

with

$$\underline{y}' = \underline{\underline{M}}^{\text{T}} \underline{y}. \quad (6.10)$$

The matrix elements m'_{ij} are given by the matrix $\underline{\underline{M}}' = \underline{\underline{M}}^{\text{T}} \underline{\underline{M}}$.

Another common method is the minimisation of χ^2 where χ for the k -iteration is given by [8]:

$$\chi^{(k)} = \underline{y} - \underline{\underline{M}} \cdot \underline{x}^{(k)}. \quad (6.11)$$

The minimisation of χ^2 can be solved by an iterative method:

$$\underline{x}^{(k+1)} = \underline{x}^{(k)} - \nabla f(\underline{x}^{(k)}), \quad (6.12)$$

where $\nabla f(\underline{x}^{(k)})$ is the gradient at the k -th iteration:

$$\nabla f(\underline{x}^{(k)}) = -2 \underline{\underline{M}} (\underline{y} - \underline{x}^{(k)}). \quad (6.13)$$

The iteration process is terminated if the minimum of χ^2 is reached.

Due to the uncertainties of the experimental data, it is not reasonable to continue the iteration until χ^2 has reached the absolute minimum. Instead, the iteration process is

usually terminated when the iteration converges to $\chi_r = 1$ that is defined by

$$\chi_r = \frac{\chi^2}{N - 1 + u} \quad (6.14)$$

with the number N of the data points and the degree of freedom u .

Chapter 7

Results and discussion

In the following, the determination of the stopping power of water for carbon ions in the energy interval between 1 MeV and 6 MeV using the aforementioned methods and data is explained and presented.

The subsequent analysis of the uncertainty using analytical methods as well as Monte-Carlo based approaches is given in detail with a listing of the overall uncertainty of the stopping power including the individual contributions.

Furthermore, the obtained stopping power including the determined uncertainty is compared to available data, semi-empirical formulas and theory. The discrepancy in the data between the stopping cross section of water and that of water vapour is investigated on the basis of the mean excitation energy and the mean charge state of the projectile.

7.1 Stopping power

Analogous to section 6.1 and section 6.2, equation 2.25 can be written in its vectorial form:

$$\underline{x}_a = \underline{\underline{D}} \cdot \underline{x}_u, \quad (7.1)$$

where \underline{x}_a and \underline{x}_u are the true attenuated and unattenuated γ -energy spectrum, respectively. The elements of the matrix $\underline{\underline{D}}$ are given by:

$$d_{ij} = \frac{m}{\tau S(v_i)} \exp \left[\int_{v_j}^{v_i} \frac{m}{\tau S(v')} dv' \right] \quad (7.2)$$

and contain the unknown stopping power S . As an analytical solution of equation 7.1 is infeasible, the stopping power was determined numerically by solving equation 7.1 by means of minimisation of χ^2 . For this purpose the stopping power is represented as an energy dependent function with a set of parameters. The parameters were varied until χ^2 reaches the minimum.

For the representation of the stopping power, the approach of Paul and Shinner [66, 67] was employed. They used a parametrized Weibull function [60] and the stopping power for helium [45] to fit experimental data for heavier ions:

$$S = y_w(x(T, \underline{\zeta})) \frac{Z_p^2}{Z_{\text{He}}^2} S_{\text{He}}. \quad (7.3)$$

The function y_w is given by

$$y_w(T, \underline{\zeta}) = \zeta_1 + (1.01 - \zeta_1) \times \left(1 - \exp \left[- \left(\frac{\lg(T/A_p) + \zeta_3 (\ln 2)^{1/\kappa} - \zeta_2}{\zeta_3} \right) \right] \right) \times (1 - 0.001628 - 0.00315e^{-\lg(T/A_p)}), \quad (7.4)$$

where T is the kinetic energy of the projectile in MeV and A_p is the mass number of the projectile. ζ_1, ζ_2 , and ζ_3 are free parameters for the fit function. The quantity κ depends on the atomic number Z_p of the projectile and is given by $\kappa = 17.18 - 0.657Z_p$. The function y_w can be considered as a model for the energy dependent effective charge of the projectile $Z_{\text{eff}} = f(T)$ and was taken from references [69, 70].

As in the case of the unfolding procedure, the iteration in solving equation 7.1 was stopped if the square of the difference between the calculated and measured γ -energy spectrum converged to a minimum. In the ideal case, the relative χ^2 is then close to 1.

The degree of freedom u in equation 6.14 is given by the number of the free parameters. The global minimum of χ_r was determined by varying the values of the three parameters ζ_1, ζ_2 and ζ_3 over a range that results in physically reasonable energy dependence of the stopping power.

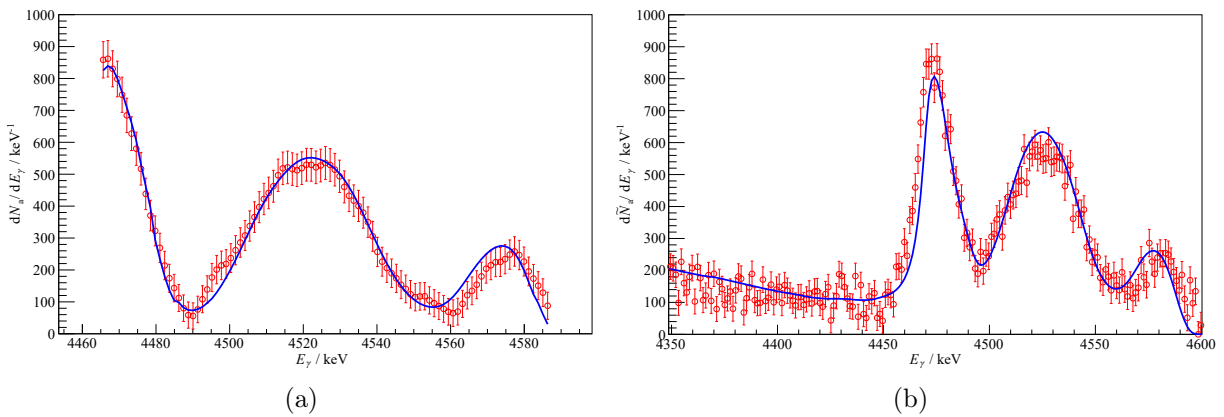


Figure 7.1: (a) Best fit (—) of the attenuated γ -energy spectrum in comparison to the measured attenuated γ -energy spectrum (\circ) restricted to the energy interval defined by the kinematics. (b) Calculated attenuated γ -energy spectrum convoluted with the energy and angular resolution function of the detector in comparison to the measured attenuated γ -energy spectrum.

Due to lateral straggling, the minimisation process has to be restricted to carbon pro-

jectile energies higher than that of the lower kinematic boundary. Figure 7.1(a) shows the γ -energy spectra with restriction to the energy interval defined by the kinematics which was obtained after the minimisation of χ^2 using the carbon projectile energy restriction of $T \geq 1$ MeV. The convolution of the calculated attenuated γ -energy spectrum with the energy and angular resolution function of the detector is shown in figure 7.1(b). The measured attenuated γ -energy spectrum was corrected for the background as described in section 5.1.

Figure 7.2 shows the stopping power determined in this work along with the data predicted by SRIM2013 [99], MSTAR [68], CASP [82] and as recommended by the ICRU report 73 [11].

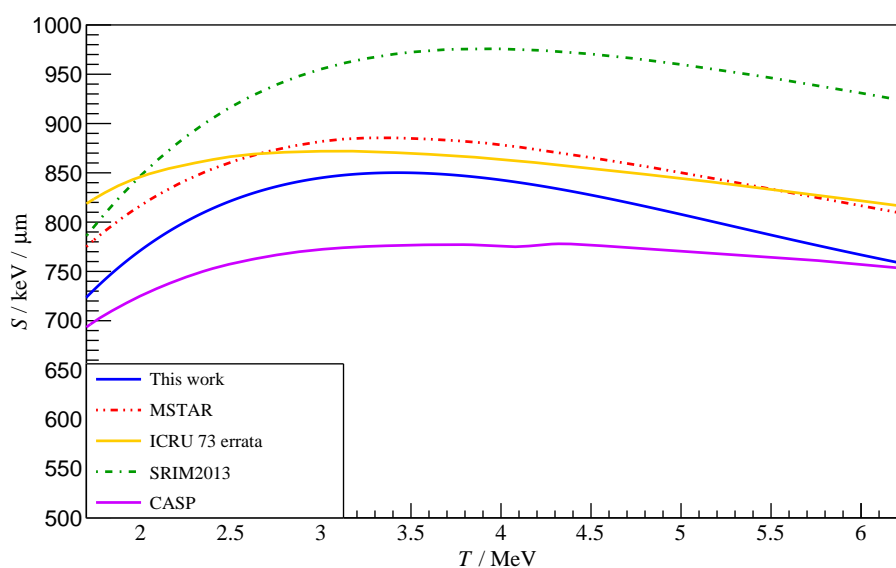


Figure 7.2: Stopping power of water for carbon ions determined in the present work in comparison to the stopping power as recommended by the ICRU [11], calculated with MSTAR [68], calculated with CASP [82] and predicted by SRIM2013 [99] for water.

7.2 Uncertainty analysis

The uncertainty of the stopping power was calculated according to [12]. Four sources mainly contribute to the uncertainty. Neglecting the potential covariance between the four dominant uncertainty sources, the overall uncertainty can be written as:

$$u_{S,\text{tot}} = \sqrt{u_{\sigma_u}^2 + u_{\sigma_a}^2 + u_p^2 + u_\tau^2}. \quad (7.5)$$

The uncertainty contribution u_τ due to the uncertainty of the lifetime $\tau = (60.9 \pm 3.5)$ fs is given by

$$\frac{dS}{d\tau} \Delta\tau = \frac{dS}{dg} \frac{dg}{d\tau} \Delta\tau. \quad (7.6)$$

Its relative contribution u_τ/u_S amounts to 5.7% and was determined numerically by performing data analysis with different values of τ .

The uncertainty u_{σ_u} of the unfolded unattenuated γ -energy spectrum arises due to the statistical uncertainty of the measured γ -energy spectrum and the uncertainty of the system response function. The uncertainty due to the statistical uncertainty of the measured γ -energy spectrum was estimated using the approach suggested by Gold and Bennet [37]. According to this approach, the variance vector of the unfolded γ -energy spectrum $\text{Var}_1(\underline{x}_u)$ is related to that of the measured γ -energy spectrum $\text{Var}_1(\underline{y}_u)$ via:

$$\text{Var}_1(\underline{y}_u) = \underline{\underline{M}}_B^{A'} \text{Var}_1(\underline{x}_u). \quad (7.7)$$

The elements of the matrix $\underline{\underline{M}}_B^{A'}$ are given by the square of the matrix elements of the matrix $\underline{\underline{M}}_B^A$ defined in equation 6.5. Equation 7.7 was iteratively solved using the method given in equation 6.9.

The uncertainty of x_u also contains uncertainty contributions due to the uncertainties of the elements of the matrix $\underline{\underline{M}}_B^A$ estimated using a Monte Carlo approach (in this work, the uncertainty of the matrix $\underline{\underline{M}}_B$ is disregarded). For this purpose, the system response function $A(E_\gamma)$ was modified within its uncertainty $\sigma_A(E_\gamma) = \sqrt{A(E_\gamma)}$ using Poisson statistics generated by a Mersenne–Twister random generator [54]. The results of the system response function variations is depicted in figure 7.3 where the frequency of the deviation between the varied energy bin content to its mean value is counted separately for ever bin. Different sets of matrices $\underline{\underline{M}}_{A,l}$ were then generated using the modified system response functions. After being multiplied by the matrix $\underline{\underline{M}}_B$, they are used to determine $x_{u,l}$ according to the numerical solution of equation 6.5. Then the variance given by the uncertainty of the system response function can be estimated by:

$$\text{Var}_2(x_u(E_{\gamma,i})) = \frac{1}{N_d - 1} \sum_{l=1}^{N_d} (x_{u,l}(E_{\gamma,i}) - \bar{X}_i)^2, \quad (7.8)$$

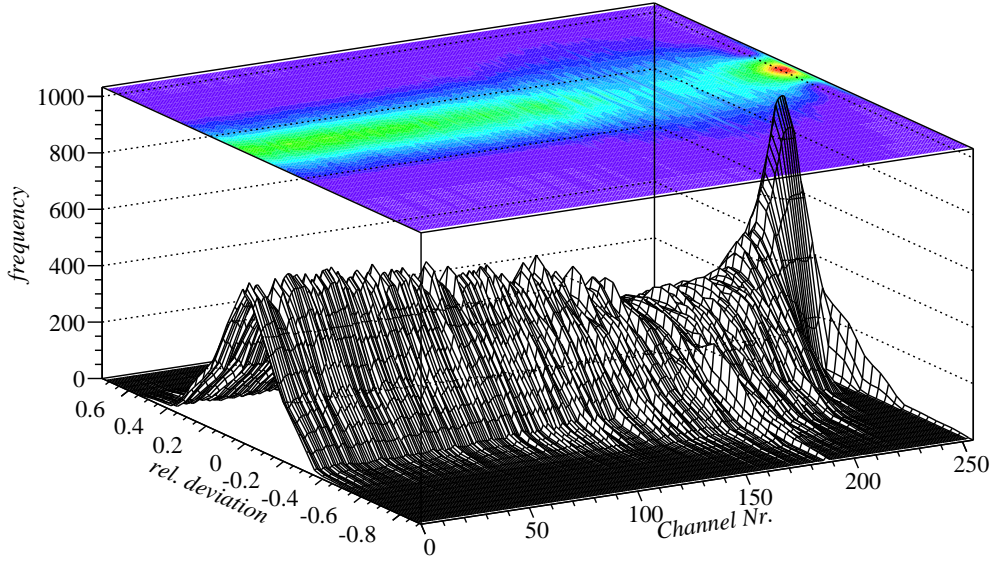


Figure 7.3: Distribution of the varied system response function for 1000 variations in total with a bin width of about 1.2 keV/channel. The frequency of the deviation between the varied energy bin content to its mean value is counted separately for every bin.

where $x_{u,l}$ is the deconvolution result using the varied system response function l , N_d is the number system response functions which were generated by the Monte Carlo approach, and \bar{X}_i is the arithmetic average of the number of events in each channel of the unfolded distribution. The total uncertainty $\sigma_u(E_{\gamma,i})$ of the counts for each individual γ -energy bin centred at $E_{\gamma,i}$ in the unfolded γ -energy spectrum was determined by:

$$\sigma_u(E_{\gamma,i}) = \sqrt{\text{Var}_1(x_u(E_{\gamma,i})) + \text{Var}_2(x_u(E_{\gamma,i}))}. \quad (7.9)$$

Figure 7.4 shows the unfolded unattenuated γ -energy spectrum including the uncertainties. Figure 7.5 shows the relative contribution of the uncertainties of the measured γ -energy spectrum and of the system response function to the total uncertainty of \underline{x}_u . It can be seen from figure 7.5 that the main contribution to the uncertainty of the unfolded unattenuated γ -energy spectrum arises due to the uncertainty of the iterative deconvolution.

To estimate the uncertainty propagation of the uncertainty of the unfolded unattenuated γ -energy spectrum into the uncertainty of the stopping power, the unattenuated spectra were again varied within the obtained uncertainty σ_u . Then the stopping power was determined for each of the varied unattenuated γ -energy spectra solving equation 7.1 iteratively as described above. This procedure was carried out for a number of varied unattenuated γ -energy spectra, 1000 in total. Figure 7.6 shows the frequency distribution as function of the deviation of the stopping power obtained using the varied unattenuated γ -energy spectra from that obtained with the unvaried unattenuated γ -energy spectrum.

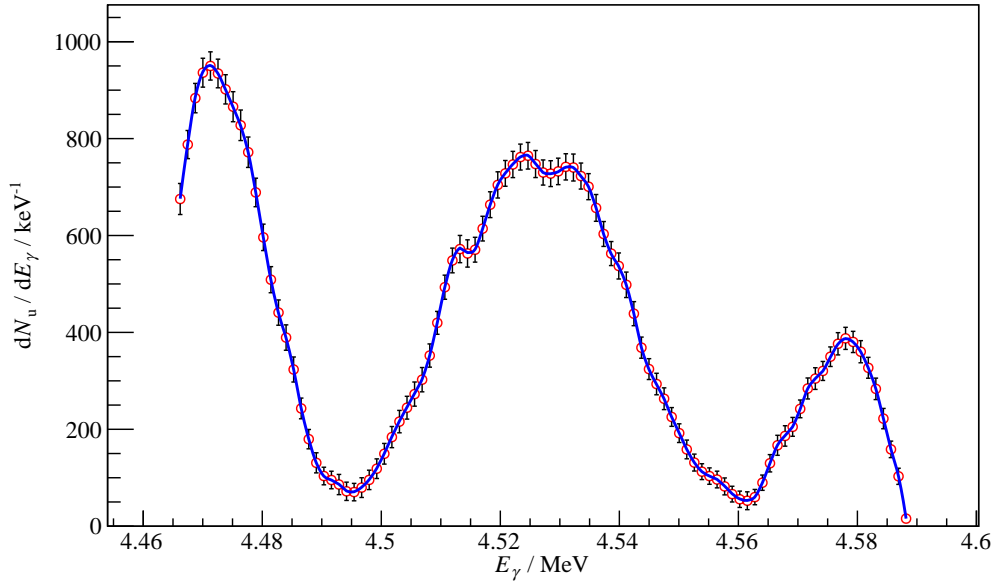


Figure 7.4: Unattenuated γ -energy spectrum with the total uncertainty calculated using equation 7.9 restricted to the energy interval defined by the kinematics. The continuous line represents the arithmetic average.

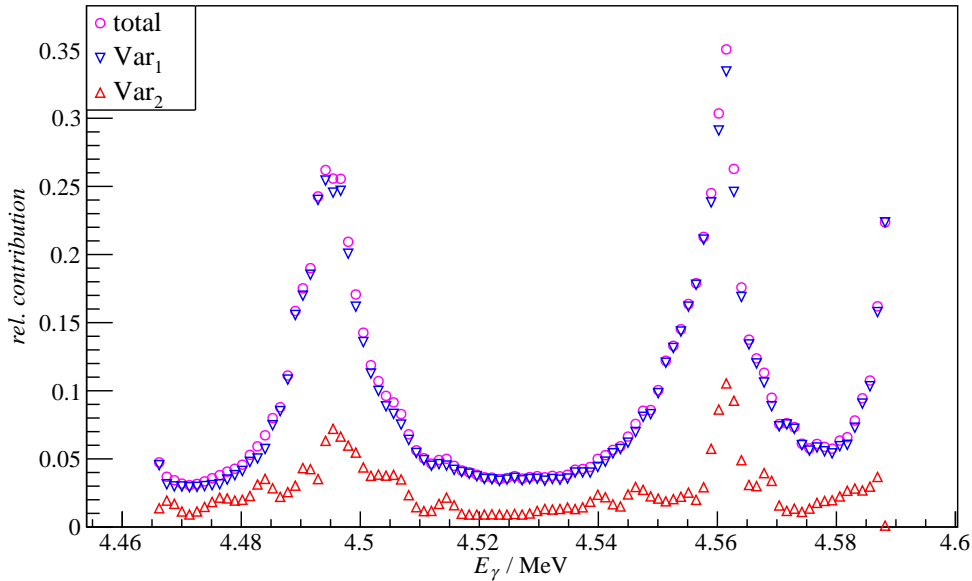


Figure 7.5: Uncertainty of the unfolded unattenuated γ -energy spectrum: relative contribution of the statistical uncertainty of the measured unattenuated γ -energy spectrum, relative contribution of the statistical uncertainty of the system response function.

The standard deviation of the frequency distribution gives the contribution u_{σ_u} of the uncertainty of the unfolded unattenuated γ -energy spectrum to the total uncertainty $u_{S,\text{tot}}$ of the stopping power.

The uncertainty contribution u_{σ_a} originating from that of the measured attenuated γ -energy spectrum was estimated in the same way as in the case of the estimation of the

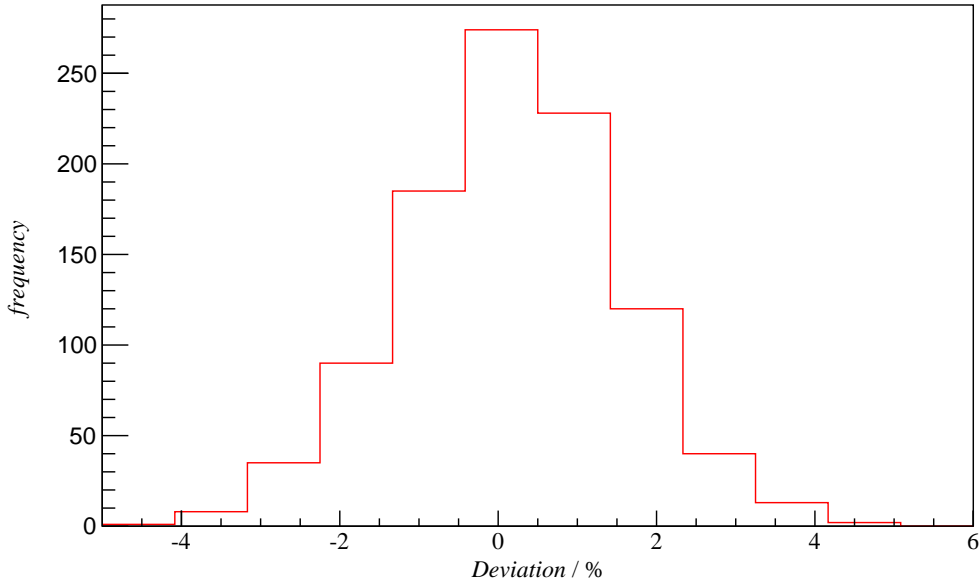


Figure 7.6: Frequency distribution of the mean relative deviation of the stopping powers caused by the uncertainty of the unfolded unattenuated γ -energy spectrum.

uncertainty contribution of the unattenuated spectrum.

The total uncertainty for channel i in the unfolded attenuated γ -energy spectrum is given by

$$\sigma_a(E_{\gamma,i}) = \sqrt{\text{Var}_1(x_a(E_{\gamma,i})) + \text{Var}_2(x_a E_{\gamma,i}) + \text{Var}_3(x_a(E_{\gamma,i}))}, \quad (7.10)$$

where $\text{Var}_1(x_a)$ is the variance arising due to the statistical uncertainty of the measured attenuated γ -energy spectrum determined using Gold's method [37], $\text{Var}_2(x_a)$ is the variance caused by the uncertainty of the energy resolution. In Addition, the contribution $\text{Var}_3(x_a)$ to the uncertainty caused by the background subtraction has to be taken into account.

The unfolded attenuated γ -energy spectrum along with its resulting standard deviation is shown in figure 7.7.

The individual contributions to the standard deviation are depicted in figure 7.8. It can be seen from figure 7.8 that the dominant contribution is again caused by the uncertainty of the unfolding procedure. It amounts to about 8.8%. The uncertainty of the background subtraction was estimated to be 8.7% and was determined from the number of counts of the background. The overall uncertainty of the attenuated γ -energy spectrum amounts to 12.6%. The total standard deviation σ_a was used for the construction of a set of modified attenuated γ -energy spectra using the same random generator and procedure as applied for the variation of the unattenuated spectra. The propagation of σ_a into the uncertainty u_{σ_a} of the stopping power was estimated again in a similar approach as in the case of the unattenuated γ -energy spectrum. Here, always the unvaried unattenuated γ -energy spectrum was used for determine the stopping power for the varied attenuated γ -energy

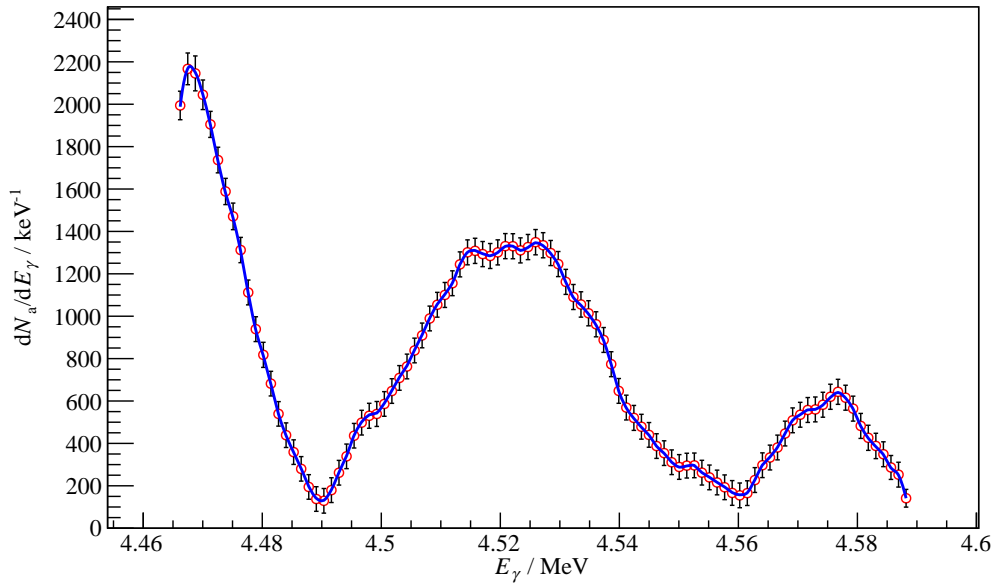


Figure 7.7: Unfolded attenuated γ -energy spectrum with the total uncertainty calculated restricted to the energy interval defined by the kinematics. The meaning of the symbols are analogous to those in fig 7.4.

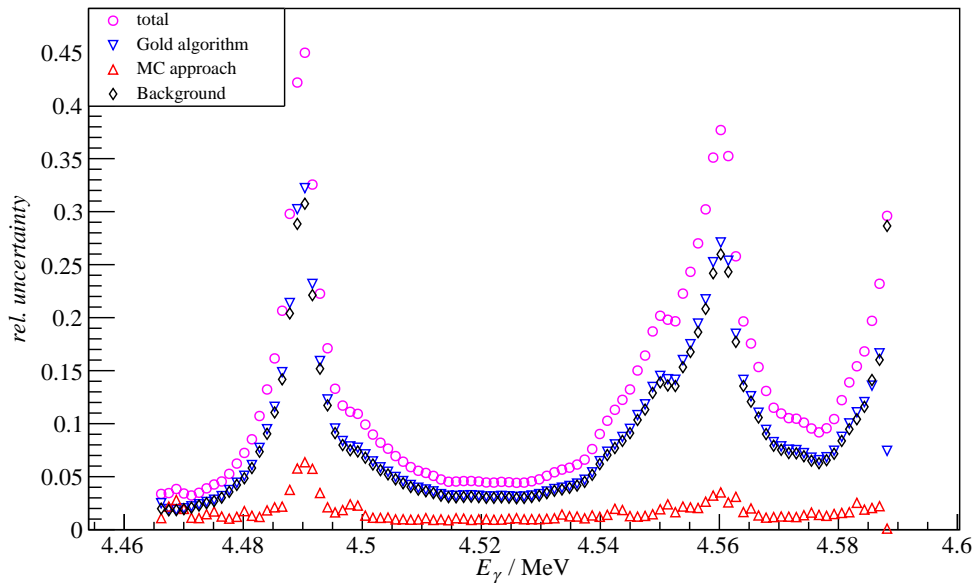


Figure 7.8: Uncertainty of the unfolded attenuated γ -energy spectrum: relative contribution of the statistical uncertainty of the measured attenuated spectrum and deconvolution process, relative contribution of the statistical uncertainty of the system response function, relative contribution by the background subtraction.

spectra. The result is depicted in figure 7.9.

As it can be expected due to the higher uncertainty of the attenuated γ -energy spectrum compared to that of the unattenuated spectrum, the deviation distribution shown in figure 7.9 appears to be broader. However, the standard deviation of the deviation dis-

tribution is considerably smaller than the mean uncertainty of the attenuated γ -energy spectrum. This means that σ_a does not fully propagate into u_{σ_a} .

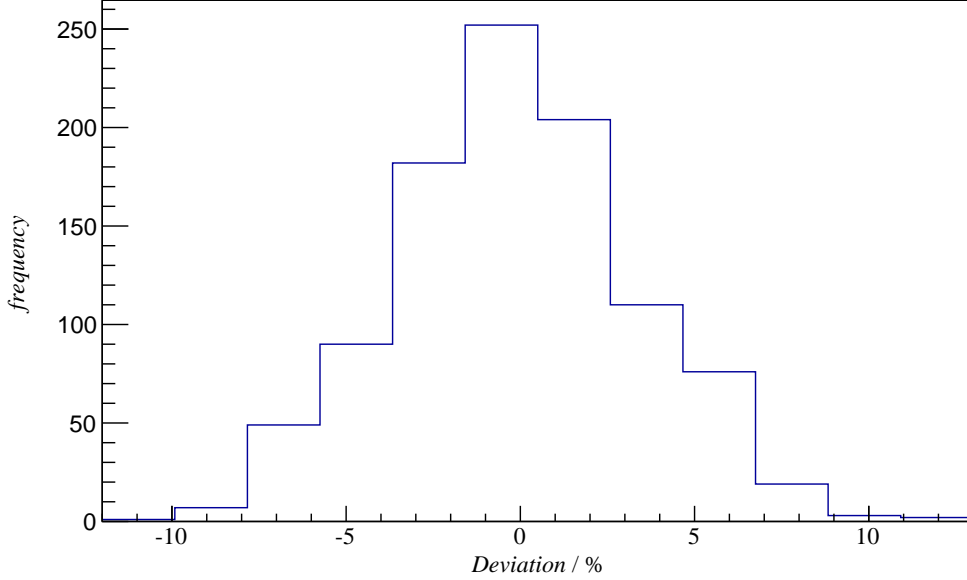


Figure 7.9: Frequency distribution of the mean relative deviation of the stopping powers arising due to the uncertainty of the unfolded attenuated γ -energy spectrum.

The last contribution to the total uncertainty of the stopping power comes from the uncertainty of the parameters $\underline{\zeta}$ used for the iterative solution of equation 7.1. It was determined by applying the method described in reference [3]. For this purpose, the covariance matrix $\underline{\underline{\Lambda}}(\underline{\zeta}_{\text{min}})$ was calculated at first and is given by [3]:

$$\underline{\underline{\Lambda}}(\underline{\zeta}_{\text{min}}) = s^2 \left(\underline{\underline{J}}(\underline{\zeta}_{\text{min}})^T \underline{\underline{J}}(\underline{\zeta}_{\text{min}}) \right)^{-1}. \quad (7.11)$$

The diagonal elements of the covariance matrix contain the variance of the parameters $\underline{\zeta} = (\zeta_1, \zeta_2, \zeta_3)$.

The Jacobian $\underline{\underline{J}}$ is defined by [3]:

$$\underline{\underline{J}}(\underline{\zeta}) = \begin{pmatrix} \frac{\partial f_1}{\partial \zeta_1} & \frac{\partial f_1}{\partial \zeta_2} & \frac{\partial f_1}{\partial \zeta_3} \\ \vdots & \vdots & \vdots \\ \frac{\partial f_N}{\partial \zeta_1} & \frac{\partial f_N}{\partial \zeta_2} & \frac{\partial f_N}{\partial \zeta_3} \end{pmatrix}, \quad (7.12)$$

where f is the calculated attenuated γ -energy spectrum according to the right hand side of equation 7.1. According to reference [3], the standard deviation s^2 can be estimated by

$$s^2 = \frac{\|\underline{G}\|_2^2}{N - m} \quad \text{with} \quad g_i = f_i - x_{a,i}, \quad (7.13)$$

where N is the length of the vector \underline{G} and m is the number of free parameters. The uncertainty of the parameters can be obtained from equation 7.11 and is given in table 7.1.

Parameter	Value	Uncertainty
ζ_1	0.137	0.051
ζ_2	-0.0189	0.56
ζ_3	11.59	2.08

Table 7.1: Table of fit parameters and their uncertainties.

The covariance matrix of the parameters given in equation 7.11 can be used for the generation of random parameter value sets containing their correlation. The vector of a random parameter value set can be written as

$$\underline{\zeta}_r = \underline{\Theta}\underline{\Xi} + \underline{\zeta}_{\chi_{\min}} \quad (7.14)$$

with a vector $\underline{\Xi}$ containing normal distributed values in the interval $[0, \dots, 1]$.

$\underline{\Theta}$ is the Cholesky decomposition $\underline{\Theta}\underline{\Theta}^T = \underline{\Lambda}$ with the matrix elements [35]:

$$\theta_{ij} = \begin{cases} 0 & \text{for } i < j \\ \sqrt{\lambda_{ij} - \sum_{k=1}^{i-1} \theta_{ik}^2} & \text{for } i = j \\ \frac{1}{\theta_{jj}} \left(\lambda_{ij} - \sum_{k=1}^{j-1} \theta_{ik}\theta_{jk} \right) & \text{for } i > j \end{cases} \quad (7.15)$$

The random parameter values are used to calculate the stopping power according to equation 7.3. Figure 7.10 shows the frequency distribution of the deviation of these stopping powers from the stopping power calculated with the parameter values $\underline{\zeta}_{\chi_{\min}}$. The figure was generated using 10^6 parameter values in total. The contribution u_P of the uncertainty of the parameters to the overall uncertainty of the stopping power was set equal to the standard deviation obtained from the distribution shown in figure 7.10.

The overall uncertainty of the stopping power was determined from the individual uncertainties according to equation 7.9 and is depicted in figure 7.11. Table 7.2 shows the resulting overall uncertainty along with the individual contributions.

As it can be seen from table 7.2, the main uncertainty contribution comes from the uncertainty of the parameters. This mainly arises because the calculated attenuated γ -energy spectrum only insufficiently matches the measured γ -energy spectrum.

A reason for the mismatch of the calculated attenuated γ -energy spectrum and the measured spectrum may be the inconsistency of the energy calibration in the two γ -energy spectra. It may arise due to the shift of the amplifier gain and consequently, due

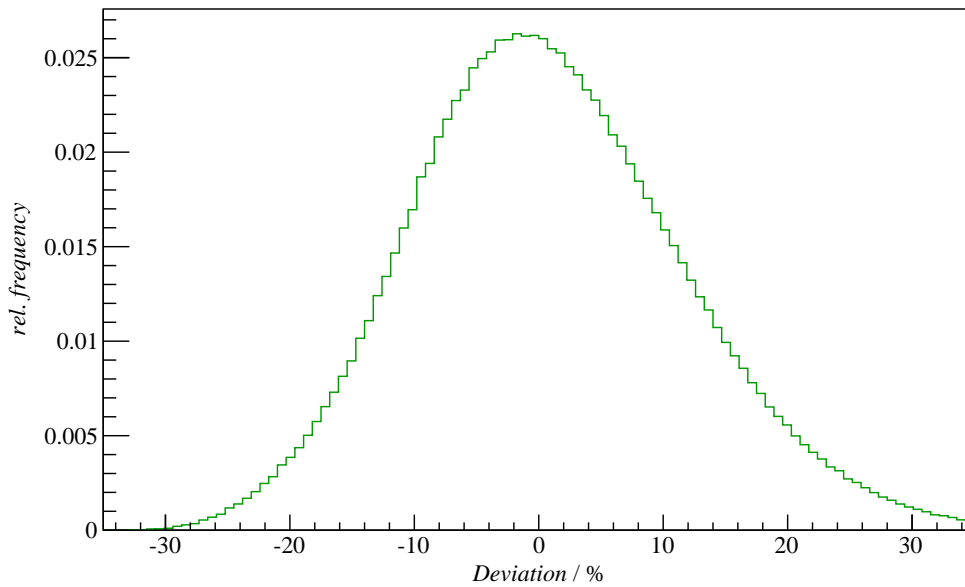


Figure 7.10: Frequency distribution of the deviation of the stopping powers generated by 10^6 parameter vectors according to equation 7.14.

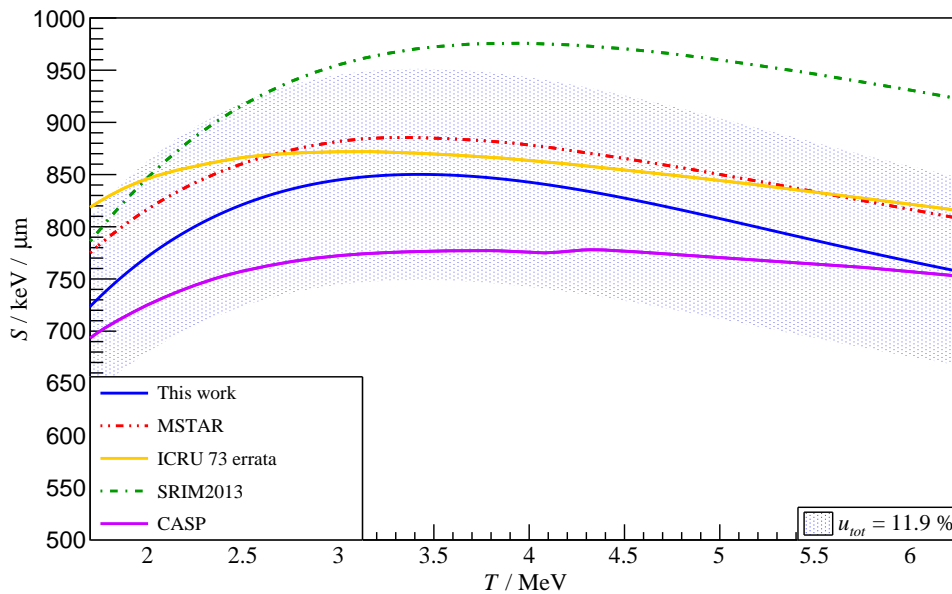


Figure 7.11: Stopping power of water for $^{12}\text{C}^*$ projectiles and its uncertainty represented by the blue band. The overall uncertainty amounts to $u_{S,\text{tot}} = 11.9\%$. For comparison the data recommended by ICRU report 73 [11] and the data predicted by MSTAR [68], CASP [82] and SRIM2013 [99] are shown.

to the change of the energy–channel relation during the measurement. While the shift of the amplifier gain was checked by means of the position of the oxygen lines in the case of the attenuated γ –energy spectrum, the unattenuated γ –energy spectrum has not been examined with respect to this shift due to the absence of appropriate γ –lines in the vicinity of the region of interest.

Contribution	rel. Standard deviation / %
Unattenuated distribution, deconvolution	1.2
Attenuated distribution, deconvolution	2.6
Parameters uncertainty and correlation	10.1
Uncertainty of lifetime	5.7
Total uncertainty	11.9

Table 7.2: Table of the uncertainty contributions.

An uncertainty contribution which was neglected is the slow-down of $^{12}\text{C}^*$ projectiles in the finite thickness of the carbon layer, which is negligible in the resolution used for determination of the stopping power in this work.

7.3 Discussion

As it can be seen from figure 7.2, the stopping power determined in this work is significantly lower than the data predicted by SRIM 2013 [99] and the ICRU [11]. The best agreement is achieved with the data calculated using the program MSTAR [68] developed by Paul et al.

One of the main sources of the uncertainties in calculating the stopping power is the inaccuracy of the mean excitation energy of the target. It has to be mentioned that the value for the mean excitation energy has often been changed by the ICRU. In the report 49 [45] published 1994, a value of 75 eV was given as the mean excitation energy of water. Based on the work of Bichsel and Hiraoka [10] this value was changed to 80 eV in the same report. The report 73 [11] published in 2005 recommended a mean excitation energy of water of 67.2 eV. However, the *National Institute of Standards and Technology* used a value of 75 eV for the calculation of stopping power and ranges of electrons, α -particles and protons [62] in water for a long time. Finally, in 2009, the ICRU adapted the value of 78 eV as done by the Geant4 consortium in 2010 [50].

In the framework of Born approximation the mean excitation energy can be determined from the energy loss function $\Im[-1/\epsilon(\hbar\omega)]$ by [32]:

$$\ln(\langle I \rangle) = \frac{\int_0^\infty d\omega \hbar\omega \ln(\hbar\omega) \Im \left[-\frac{1}{\epsilon(\hbar\omega)} \right]}{\int_0^\infty d\omega \hbar\omega \Im \left[-\frac{1}{\epsilon(\hbar\omega)} \right]}. \quad (7.16)$$

Figure 7.12 shows the energy loss function of water for excitation energies up to about 50 eV. The data displayed in figure 7.12 mainly refer to the ionisation of outer electrons, as the ionisation of inner shell electrons of water needs much higher energies than 50 eV. It is assumed that the energy loss function of water is equal to that of water vapour for excitation energies higher than 50 eV because inner shell electrons do not contribute to the

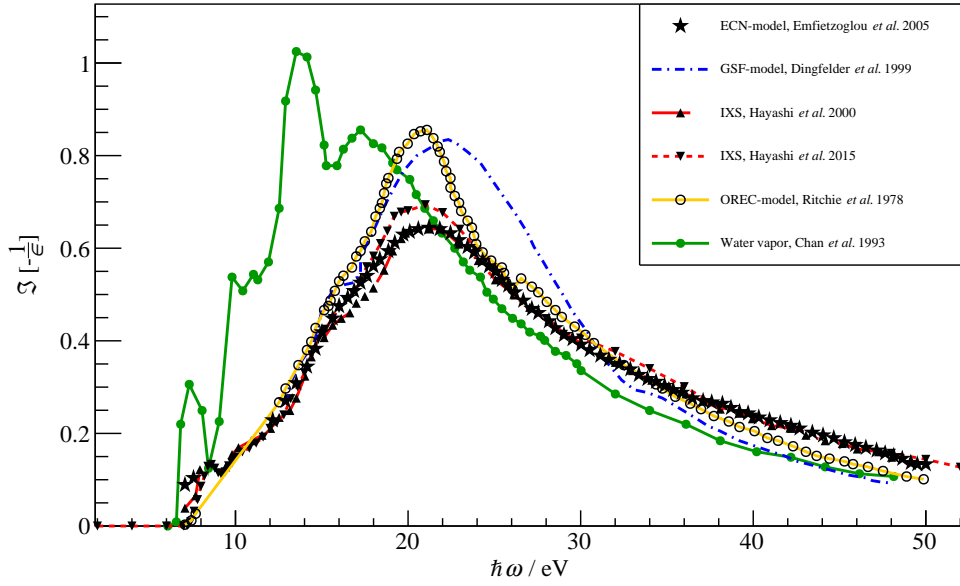


Figure 7.12: Energy loss function of water: Emfietzoglou–Cucinotta–Nikjoo (ECN) model based on inelastic X-ray scattering (IXS)[31], Dingfelder–GSF [26] and OREC dielectric model [75] based on optical reflectance. The experimental data from small-angle inelastic X-ray scattering by Hayashi *et al.* from 2000 [40] and 2015 [39] are also shown. The experimental data for water vapour were derived from measurements by Chan *et al.* [22].

chemical bonding. Using this assumption, the contribution of higher ionisation energies to $\langle I \rangle$ of water was determined in this work by the subtraction of $\langle I \rangle_{<50}$ using equation 7.16 and the data for water vapour shown in figure 7.12 from the mean excitation energy of water recommended by the ICRU. The sums $\langle I \rangle$ of the contribution $\langle I \rangle_{>50}$ and the contribution of ionisation energies below 50 eV are listed in table 7.3.

Source	$\langle I \rangle_c$
ECN–Model, Emfietzoglou <i>et al.</i> 2005	76.0
GSF–Model, Dingfelder <i>et al.</i> 1998	74.5
IXS, Hayashi <i>et al.</i> 2000	75.9
IXS, Hayashi <i>et al.</i> 2015	79.6
OREC–Model, Ritchie <i>et al.</i> 1978	74.9

Table 7.3: Mean excitation energies calculated using the energy loss functions shown in figure 7.12.

The calculated mean excitation energies $\langle I \rangle$ given in table 7.3 agree well with the value of 75 eV which is widely accepted. The calculation further reveals that the contribution to the mean excitation energy coming from excitation lower than 5 eV is significantly higher for water than that of water vapour. This tendency is suggested by the energy loss function in figure 7.12. It shows that the maximum of the energy loss function of water vapour is shifted more towards lower energies in comparison to that of water.

The most recent data of Hayashi *et al.* 2015 [39] provide energy loss functions of

water up to 100 eV. The mean excitation energy calculated up to this energy loss is in good agreement with the reported contribution of 46.7 eV by Abril *et al.* [2]. Also, there is a good agreement between the resulting mean excitation energy of 79.6 eV and the experimental value of 79 eV reported by Bichsel [10]. This value is in accordance with the value of 78 eV reported by the ICRU in 2009 [91].

Low mean excitation energy is connected with high stopping cross section, defined as the stopping power divided by the target number density, according to the Bethe–Bloch equation. Therefore, the stopping cross section of water for charged particles should be lower than that of water vapour in the Bethe–Bloch region. This behaviour is predicted by SRIM2013 according to which the stopping cross section of water in its liquid phase is about 5 % lower than that of water vapour.

The reduction of the stopping cross section due to the increased mean excitation energy is only about 2.5 % when using the recommended values of the ICRU for the mean ionisation energy of 78 eV and 69.1 eV for water and water vapour, respectively. The usage of the mean excitation energy of 81.8 eV [26] and of 79.7 eV for water [41] results in a reduction of the stopping cross section of about 3.5 % and 3.0 %, respectively, which does not explain the difference of 5% predicted by SRIM2013.

Interestingly, only SRIM2013 predicts the stopping cross section of water for carbon ions to be lower than that of water vapour for carbon ions. Xu *et al.* calculated the stopping sections of water for protons by applying the modified local plasma model [98] and compared the results with theoretical and experimental stopping cross sections of water vapour with the experimental results of D₂O–ice [97] and experimental results of water vapour [74]. An overview of the data is given in figure 7.13. The experimental data

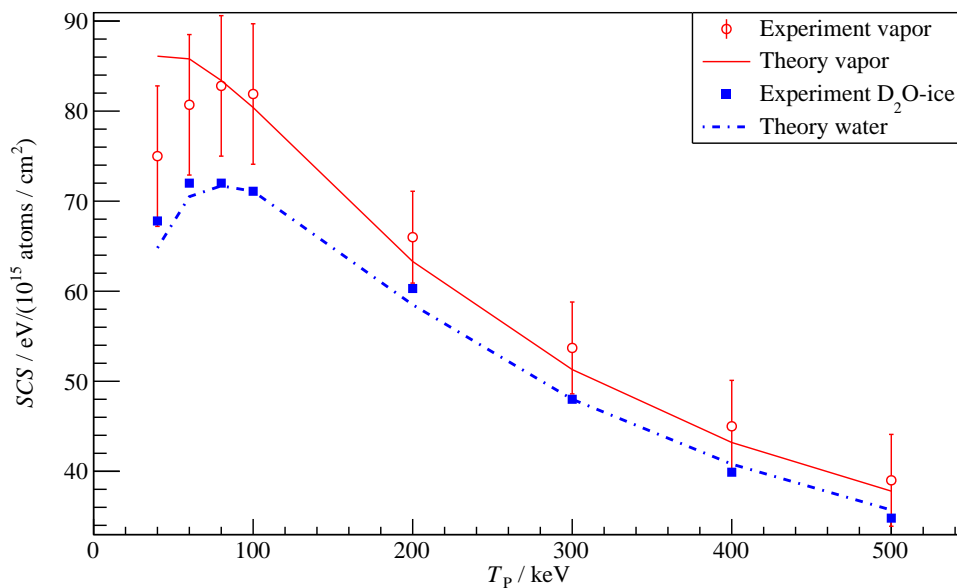


Figure 7.13: Stopping cross sections of water in different state of aggregation obtained using modified local plasma model and experimental data (adapted from Xu *et al.* [98]).

and the results of the theoretical model show a good agreement.

Figure 7.13 furthermore indicates that the stopping cross sections of different aggregation states are noticeably different. The theoretical calculation predicts that the stopping cross section of water in its liquid phase is lower than that of water vapour. According to figure 7.13, the experimental stopping cross section of D₂O–ice for protons is about 11 % lower than that of water vapour. Other experimental and theoretical data also indicate that the stopping cross section of water for protons is lower than that of water vapour. The semi-empirical calculation of Emfietzoglou *et al.* [30] which uses the dielectric response function formalism predicts that the stopping cross section of water is about 20 % lower than that of water vapour. Experiments by Shimizu *et al.* [87] state, in the case of protons, a reduction of the stopping cross section of about 11 % for water compared to water vapour. The experiments of Thwaites with α -particles [95] confirm the trend that the stopping cross section of water is lower than that of water vapour.

The effect that the stopping cross section of water is lower than that of water vapour seems to be more pronounced in the low velocity regime of the projectile, Ellis *et al.* [29] reported that at α -beam energies between 5 MeV and 8 MeV, the stopping cross sections of water and water vapour show no difference. This trend may be due to the so-called low-energy polarisation effect as reported by Palmer and Simons [65]. In terms of the local plasma model, the dependence of the stopping cross section on the state of aggregation can be explained by the change of the energy required to excite a plasmon due to the different degree of bonding tightness [98].

Figure 7.14 shows the stopping cross sections of water and water vapour for different projectiles calculated using MSTAR. MSTAR is based on a semi-empirical model that calculates the stopping power of water for carbon ions based on that of helium ions [45] in combination with a Weibull function [69, 70]. It can be seen that for α -particles and lithium ions in water the calculated stopping cross section is significant lower than in water vapour, which is consistent with the theoretical and experimental data above. For ions heavier than beryllium, the stopping cross section of water is predicted to be higher than of water vapour. This is probably caused by the higher mean charge state of the projectile in the liquid phase of water.

Figure 7.15 shows the stopping cross sections of water and water vapour calculated with MSTAR [70] in comparison to that determined in this work and to the prediction of SRIM2013. The stopping cross sections calculated with MSTAR are in the vicinity of those determined in this work and show a similar energy dependence. Both stopping cross sections are significant lower than those predicted by SRIM2013.

The stopping cross section of water for carbon ions recommended by the ICRU also lies below that calculated with SRIM2013, but higher than that of water vapour as shown in figure 7.16. It is about 12.8 % higher than the stopping cross section determined in this work and has a notably different energy dependency. Especially in the low energy region,

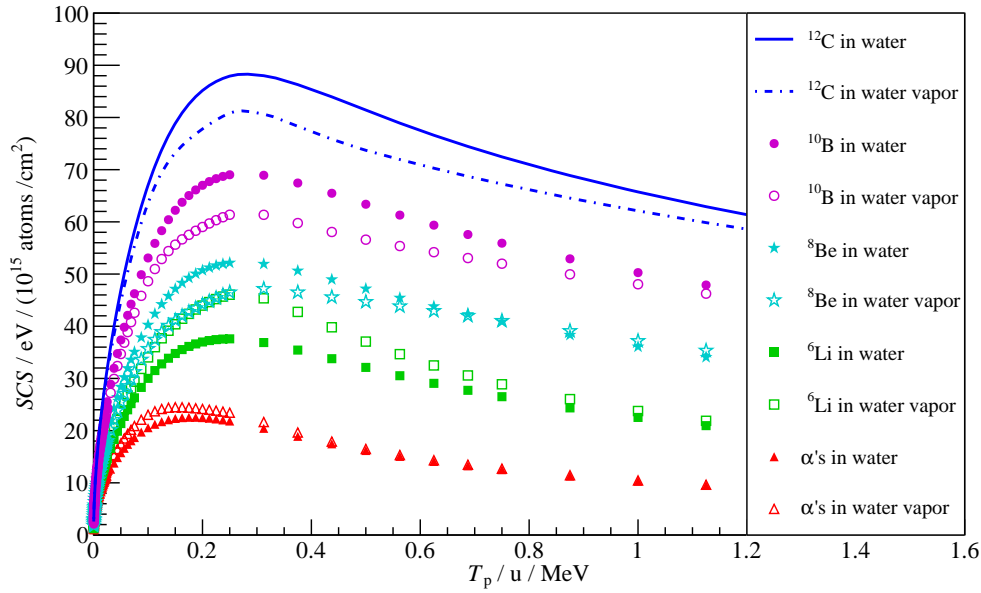


Figure 7.14: Stopping cross section of water and water vapour for different projectiles calculated with MSTAR [68] (${}^6\text{Li}$, ${}^8\text{Be}$, ${}^{10}\text{B}$ and ${}^{12}\text{C}$) and the recommended value of the ICRU for α particles [45].

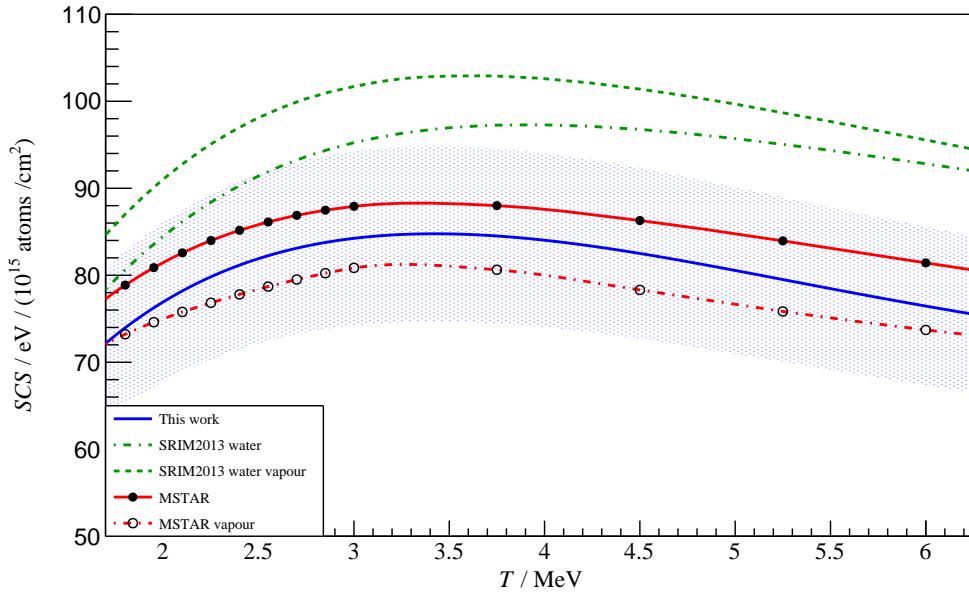


Figure 7.15: Stopping cross sections of water and water vapour for carbon ions calculated with MSTAR [68] in comparison to the stopping cross section determined in this work and predicted by SRIM2013 [99] as reference.

it shows a flatter energy dependence. It is noteworthy that the maximum of the stopping power recommended by the ICRU is significantly shifted to lower energies in comparison to other data sets.

The ICRU recommendations given in report 73 are generated using the computational program of **P**eter-**A**ndreas-**S**igmund-**S**chinner, (PASS) [89]. It is based on binary theory,

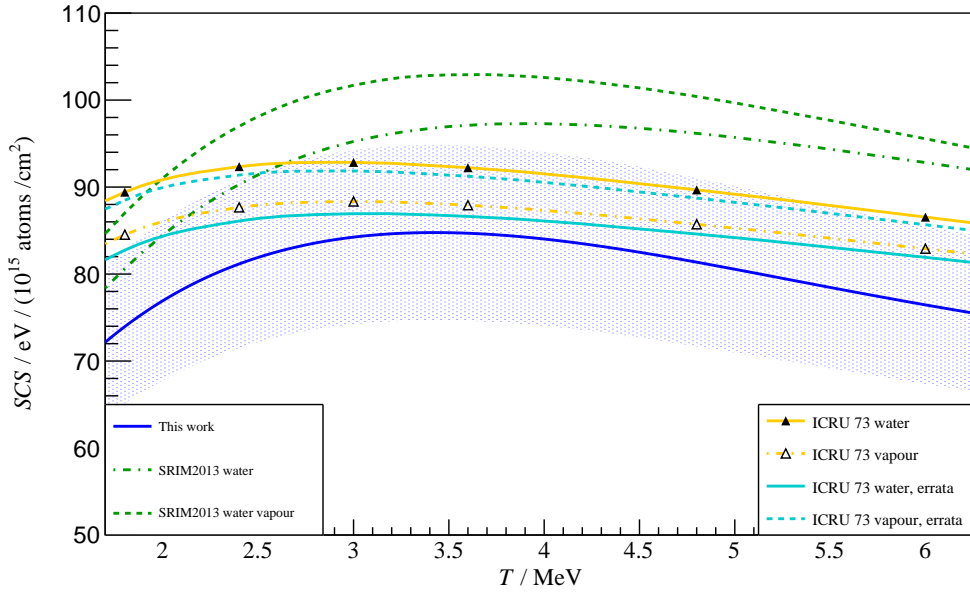


Figure 7.16: Stopping cross sections of water and water vapour for carbon ions calculated using the program *PASS* and the mean excitation energies recommended by ICRU report 73 [11] in comparison to the stopping cross sections determined in this work and predicted by SRIM2013 [99]. Additionally, the data calculated using the mean excitation energies published in the errata of the ICRU report 73 in 2009 are shown.

which was originally intended for determining the stopping power for heavy ions [90]. The binary theory takes into account charge-changing processes in the calculation of the stopping power. For the estimation of the projectile charge state, a Thomas–Fermi–type equation is used and is parametrised.

The ICRU corrected the previously reported value of the mean excitation energy of water and water vapour after the measurement of the mean excitation energy of water by Schardt *et al.* [79] using energetic protons and a revision of the tables given by Berkowitz [5], respectively. The corrected values for the water and vapour are $\langle I \rangle_W = 78.0 \text{ eV}$ and $\langle I \rangle_V = 69.1 \text{ eV}$, respectively [91]. As the mean excitation energy is an input parameter for the computer program *PASS*, the corrected values lead to a decrease of the stopping cross section of water and to an increase of the stopping cross section of water vapour.

The data calculated using the new mean excitation energies published in the Errata of the ICRU report 73[91] are more consistent with the stopping cross section measured in this work. It is also noteworthy that the stopping cross section of water vapour is higher than that of water according to the actual data recommended by the ICRU [91].

Another data set was calculated by using the program **C**onvolution **a**pproximation for **s**wift **P**articles (*CasP*) [82] which allows the numerical calculation of the energy transfer from the projectile to the target by ionisation and excitation of the target atoms. The model used in *CasP* is a non-linear theory including Bloch–terms and is called **U**nitary **C**onvolution **A**pproximation [82]. Like *PASS*, it is a purely theoretical approach in dif-

ference to SRIM, MSTAR and other semi-empirical models. It can be seen from figure 7.17 that the stopping cross section obtained using *CasP* gives the lowest value among the data predicted by SRIM2013, ICRU, MSTAR and measured in this work. As in the case of MSTAR and the recommendation of the ICRU, the stopping cross section of water vapour is lower than that of water. For the calculation of the stopping cross section, it determines the mean equilibrium charge state of the projectile by means of two distinct multi-parameter fit functions, one for solids and one for gas targets, which were based on the evaluation of experimental charge-state distributions [81].

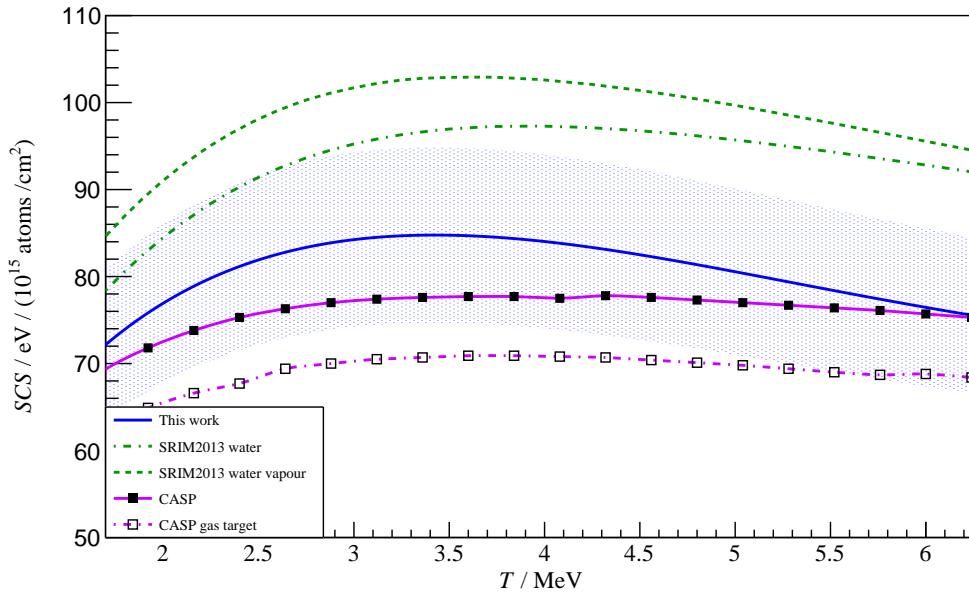


Figure 7.17: Stopping cross sections of water and water vapour calculated using *CasP*

It is noteworthy that the shift of the maximum towards lower energies which can be seen in the data calculated with *PASS* does not appear in the calculations using *CasP*. The maximum lies roughly at the same energy as measured in this work and calculated using MSTAR. This can be seen in figure 7.17. The version *CasP 5.2* also provides Barkas and shell correction.

Figure 7.18 shows the stopping cross section of water for carbon ions obtained from the track structure code calculation PARTRAC [84, 34]. Track structure codes perform the calculation step by step throughout until the particle is at rest. This calculation uses a scaling procedure on the effective charge state of the projectile and is described in detail in reference [83]. In the energy region between 2.5 MeV and 4.5 MeV, the stopping power data calculated with PARTRAC show a very good agreement with that obtained in this work. The energy dependence shows a very flat curvature, even lesser pronounced than that recommended by the ICRU.

In the energy region of the maximal stopping power, the effective charge is a crucial parameter because the stopping cross section varies with the square of the projectile

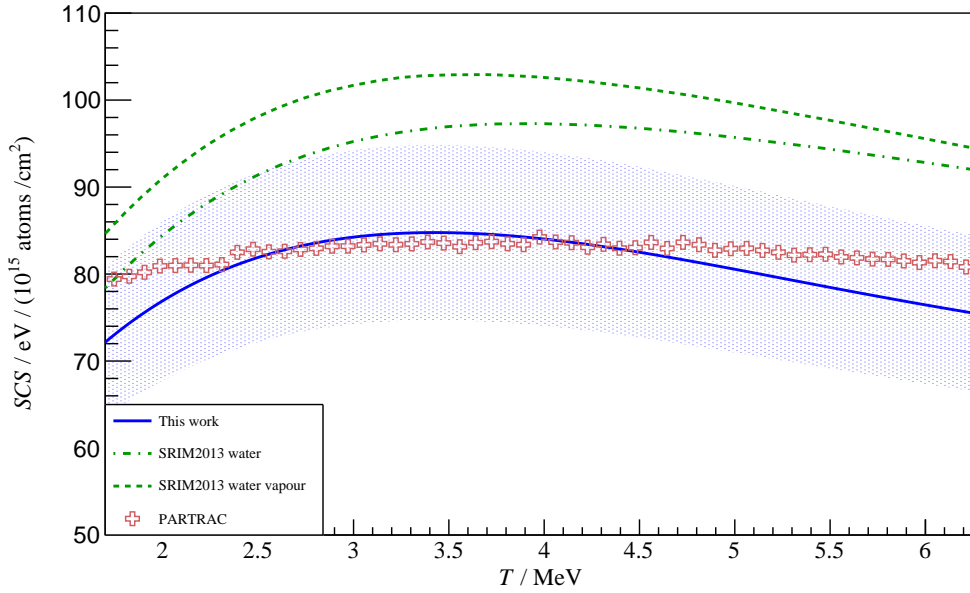


Figure 7.18: Stopping cross sections of water derived from track structure Monte Carlo code PARTRAC calculated by Werner Friedland [34]

charge. Using the Bethe–Bloch equation, the mean charge state of carbon ions can be roughly estimated from the experimental results of this work. For the estimation, the mean excitation energy of 78 eV recommended by the ICRU and the following scaling law were employed [51]:

$$-\left. \frac{dT}{dx} \right|_2(T) = -\left(\frac{Z_{\text{eff},2}}{Z_{\text{eff},1}} \right)^2 \left. \frac{dT}{dx} \right|_1 \left(\frac{M_1}{M_2} T \right), \quad (7.17)$$

where $Z_{\text{eff},1} = 2$, $Z_{\text{eff},2} = f(T)$, $\left. \frac{dT}{dx} \right|_1$ is the stopping power of water for α -particles and M_1/M_2 is the ratio of the projectile masses. The stopping power $\left. \frac{dT}{dx} \right|_2(T)$ is given by the results of this work. Figure 7.19 shows Z_{eff} obtained using equation 7.17. The charge state determined from the data in this work was fitted with the following function:

$$Z_{\text{eff}}(T) = a + b \ln(T) \quad \text{with} \quad [T] = \text{MeV}, \quad (7.18)$$

where the best fit was obtained for $a = 2.03 \pm 0.06$ and $b = 0.9 \pm 0.1$. Despite the fact that the projectile energies are below the energy region where the Bethe–Bloch formula can be applied, the resulting mean equilibrium charge state of the projectile is in a good agreement with other reported data. Interestingly, the mean charge state reported by Schiwietz and Grande [81] is about 14.4% higher while the stopping cross section calculated using *CasP* is lower than that determined in this work by about 4%. However, it has to be mentioned that the Bethe–Bloch theory implies a quadratic dependency of the stopping power on the projectile charge while *CasP* implies a non-quadratic dependency. The mean equilibrium charge state extracted from the charge distribution reported by

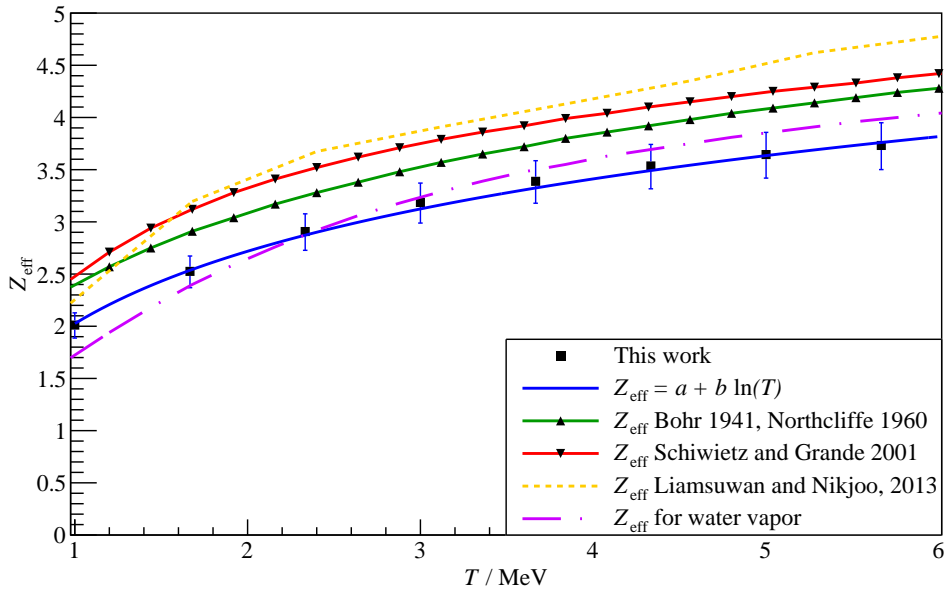


Figure 7.19: Mean equilibrium charge–state of the projectile: Bohr [15], revised by Northcliffe [61], Schiwietz and Grande [81], Liamsuwan [52] and this work.

Liamsuwan and Nikjoo is in the vicinity of the data reported by Schiwietz [81] in the energy region between 1.5 MeV and 4 MeV. The difference between both data increases with increasing projectile velocity. Liamsuwan and Nikjoo calculated the charge state distribution from the total cross section for charge changing processes such as electron capture (projectile captures an electron), electron loss (projectile loses an electron), transfer ionisation (projectile captures an electron, target is ionised) and loss ionisation (projectile loses an electron, target is ionised) [52].

7.4 Impact on radiation therapy

Due to their locally well defined dose distribution the usage of carbon ions for cancer therapy could be advantageous. They are especially useful for killing hypoxic cancer cells which are radio resistant due to the absence of oxygen radicals which contribute to radiation damages in a large scale.

Vice versa, an inaccuracy in the predicted path will result in serious damage to healthy tissues. For the estimation on how different energy dependent stopping powers may influence the depth dose distribution, the energy loss in dependence of the depth can be calculated and compared. In the case of heavier ions additionally an increase of the energy deposition at the distal end of the Bragg peak, caused by nuclear fragments, has to be considered. However, to some extent the energy loss of the projectile can be correlated to the energy deposition at depth and, hence, to the damage. The energy loss in the depth of the target can be calculated from the energy of the projectile at depth using equation 2.5.

Figure 7.20 shows the energy loss at depth of a carbon ion with $T_0 = 7$ MeV calculated using the stopping powers of water for carbon ions from SRIM2013 [99], MSTAR [68], recommendation from the ICRU [91], CASP [82] and this work.

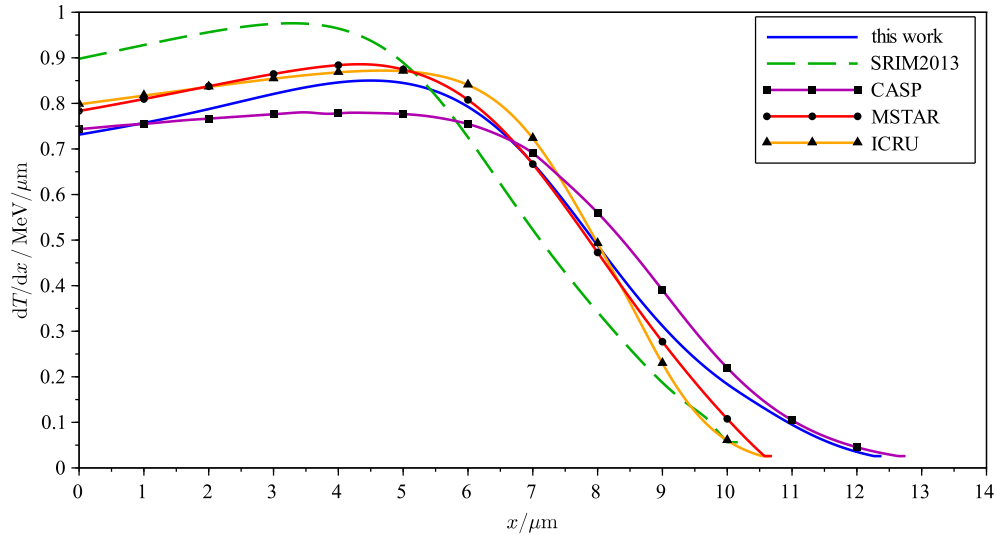


Figure 7.20: Energy loss of carbon ions as function of the depth in water.

The theoretical range of the carbon ion comparing the data from SRIM2013, prediction of MSTAR and the recommendation of the ICRU shows a deviation of about 5%. In contrast to the recommendation of the ICRU, the data obtained in this work would result in an increase of the range which amounts to 16%, where CASP gives an increased range of 19%. The accurate knowledge of the stopping power of water for ions is not only necessary for precise targeting of the target volume. The maximum of the energy loss should be placed in the PTV avoiding the radiation damage in healthy tissues located behind it. This is especially crucial at the distal end as in many cases radiation sensitive risk organs are located right behind the tumor volume (e.g. brain stem tumor). It is noteworthy that the differences in range shown in figure 7.20 (for $T_0 = 7$ MeV) could be much larger than indicated, as the depth at which the projectile is stopped is dependent on the stopping power from the primary energy (in the order of GeV) down to zero.

More important than the range of the carbon ions is the shape of the energy loss which is directly correlated to the shape of the stopping power. Regarding the distal end of the pathway at about $9.5 \mu\text{m}$, the energy loss of the projectile in case of the data from SRIM2013 and the recommendation of the ICRU is comparable and significantly lower than that of the data from MSTAR and especially of the data from this work and CASP. The increased energy loss of the projectile at the end of its path may lead to an increased biological effect. Radiological measurements indicate that the biological effectiveness of ions crucially depend on the LET which is equal to the stopping power in case of its unrestricted representation. The decrease of the energy loss may have two

effects: Firstly, decreased dose deposition in the PTV due to lower stopping power and, hence decreased biological damage. Secondly, increased dose deposition due to higher stopping power outside the PTV and therefore in the healthy tissue. This may lead to a reduced tumor control probability and at the same time to an increased normal tissue complication probability due to the altered shape of the stopping power.

Therefore, not only a highly accurate measurement of the stopping power is of necessity, but also the determination of its energy dependence. In this work it has been shown that the IDSAM is a suitable method for the measurement of the energy loss of ions in tissue in the region of therapeutic interest.

Chapter 8

Conclusion and outlook

An experimental set up was planned, built up and optimised for the measurement of the stopping power of liquid water for $^{12}\text{C}^*$ projectiles using the IDSAM. The mechanical and physical criteria for the target were examined and tested including the configuration of the electronic set up. A target positioning system was developed which allows the adjustment of the target relative to the beam direction during the measurements to achieve an optimal signal-to-background ratio which is decisive for the accurate determination of the stopping power. A system for the measurement of ion beam current with five discrete channels containing analogue and digital components, μC programming and communication with a PC was also developed. It enables the storage and visualisation of the measured data by a self-developed graphical user interface.

A precise target positioning is realised by an electro-mechanical design containing power electronics for driving two DC-motors and μC -based electronics that enable the control of the measurement and the regulation of the target position. The system was proven an indispensable part of the experiment because it allowed fast set up of the experiment with low background. The self-developed experimental apparatus and data acquisition system was successfully employed to measure the stopping power of water for carbon ions with energies up to 6 MeV.

The present result was compared to published stopping powers obtained by theoretical approaches, semi- and full-empirical and experimental data. Within the uncertainty, the present stopping cross section is consistent with the stopping cross sections predicted by MSTAR[68], ICRU report 73 errata [91] and CasP [82]. The stopping cross sections calculated with SRIM2013 [99] and those of the ICRU report 73 [11] are higher than the stopping cross section determined in this work. Noteworthy is the difference between the data of the ICRU report 73 and the ICRU report 73 errata. The ICRU report 73 errata considerably changed the value of the mean excitation energy of water and water vapour. The mean excitation energy was subject to great changes in the last decades and is still of great interest for many researchers. However, in the energy region of the maximal stopping power, the charge state has a larger effect on the stopping power but is not

accurately known.

The charge state determined in this work is in accordance with the data for water vapour, but noticeably lower than that obtained using the model of Schiwietz and Grande [81], Bohr [15], Northcliff [61] and the data given by Liamsuwan [52]. However, in comparison to the data given for solid targets the energy dependence is in good agreement.

An extensive uncertainty analysis was performed using analytical as well as Monte Carlo based methods. The overall uncertainty of the stopping power determined in this work amounts to 11.9%. The uncertainty is mainly caused by the discrepancy between the measured and the calculated attenuated γ -energy spectrum. The discrepancy probably arises due to an instability in the detection system which causes an energy shift of the spectrum. Additionally, the deterioration of the energy resolution due to background neutrons which was minimised as far as possible but could not be prevented completely, may alter the shape of the spectrum. This may lead to a different system response function for the attenuated and the unattenuated γ -energy spectrum and consequently, to an insufficient reproduction of the measured attenuated spectrum by calculation. The uncertainties arising due to this effect can be lowered in future experiments by checking the energy resolution function during the measurement. Furthermore, the background can be reduced by the usage of an anti-Compton shielding. The anti-Compton shielding will significantly increase the signal to noise ratio, as the attenuated γ -energy spectrum sits on the Compton continuum of the oxygen lines.

The mathematical model used for the representation of the stopping power revealed to be rather sensitive to small changes of the parameter values in a certain range. Hence, the development of a suitable mathematical model may allow to decrease the uncertainty by a considerable amount. Furthermore, a major reduction of the uncertainty can be achieved by measuring the attenuated and unattenuated γ -energy spectrum in one beam time. The energy calibration of the detector system should also be checked during the measurement. The ratio of the integral of the attenuated γ -energy spectrum and the oxygen line can also be used as a quality criterion because it should not change over time.

By realising these improvements and prolonging the measurement time to reduce the statistical uncertainty, the uncertainty could be decreased to a few per cents. It has to be mentioned that for the reduction of the overall uncertainty of the stopping power, a precise knowledge of the mean lifetime of the first excited state in ^{12}C is necessary, because it directly propagates into the uncertainty of the stopping power. The lifetime can be determined more accurately by using the Doppler-shift attenuation method employing a target of known stopping power.

In conclusion, it can be stated that the IDSAM is an appropriate method for the determination of the stopping power of water, or more general, of media which cannot be measured by means of transmission experiments. It also can be used for the quantification of the physical state effects.

Bibliography

- [1] *LMx58, LMx58x, LM2904, LM2904V dual operational amplifiers*. Texas Instruments, Post Office Box 655303, Dallas, Texas 75265, 2015.
- [2] I. Abril. Calculated electronic energy loss of swift proton and helium ion beams in liquid water. *9th International Conference on Applications of Nuclear Techniques, Crete, Greece*, 9, 2008.
- [3] R. C. Aster, B. Borchers, and C. H. Thurber. *Parameter estimation and inverse problems*. Elsevier, 2 edition, 2013.
- [4] W.Y. Baek, G.H. Both, D. Gassen, W. Neuwirth, and M. Zielinski. Energy loss of C-12 projectiles in different carbon modifications. *Physical Review*, 35:51–59, 1987.
- [5] Joseph Berkowitz. 5 - triatomic molecules. In Joseph Berkowitz, editor, *Atomic and Molecular Photoabsorption*, pages 181 – 236. Academic Press, London, 2002.
- [6] H. Bethe. Bremsformel für elektronen relativistischer geschwindigkeit. *Zeitschrift für Physik*, 76:293–299, 1932.
- [7] K. Bethge. *Kernphysik*. Springer-Verlag Berlin Heidelberg New York, 1996.
- [8] Philip R. Bevington and D. Keith Robinson. *Data Reduction and Error Analysis for the Physical Sciences*. K. A. Peterson, 2003.
- [9] H. Bichsel. Shell corrections in stopping powers. *Phys. Rev. A*, 65:052709, 2002.
- [10] H. Bichsel and T.Hiraoka. Energy loss of 70 mev protons in elements. *Nuclear Instruments and Methods in Physics Research Section B: Beam Interactions with Materials and Atoms*, 66(3):345 – 351, 1992.
- [11] R. Bimbot, H. Geissel, H. Paul, A. Schinner, and P. Sigmund. Stopping of ions heavier than helium. *Journal of the ICRU*, 5(1):0, 2005.
- [12] BIPM. GUM–guide to the expression of uncertainty in measurement. 2008.
- [13] M. Bittner. Simulation der ortsabhängigen Vollabsorptionszähleffizienz eines HPGe–Detektors mit Hilfe von EGSnrc. Master’s thesis, Technical University Brunswick, 2014.

- [14] N. Bohr. Transmutations of atomic nuclei. *Science*, 86(2225):161–165, 1937.
- [15] N. Bohr. Velocity-range relation for fission fragments. *Phys. Rev.*, 59:270–275, 1941.
- [16] W. Brandt and M. Kitagawa. Effective stopping-power charges of swift ions in condensed matter. *Physica B: Condensed Matter*, 25:5631–5637, 1982.
- [17] S. Braun. Coating of tantalum with amorphous carbon, private communication. Technical report, Fraunhofer-Institut für Werkstoff- und Strahltechnik, Winterbergstr. 28, 01277 Dresden, 2016.
- [18] K. Brown. *Reflections on relativity*. 2014. <http://www.mathpages.com/rr/rrtoc.htm>.
- [19] R. Brun and F. Rademakers. Root - an object oriented data analysis framework, proceedings aihnp'96 workshop, lausanne, sep. 1996, nucl. inst. & meth. in phys. res. a 389 (1997) 81-86, 2011. <http://root.cern.ch/>.
- [20] Burr-Brown. *IVC 102 Precision switched integrator transimpedance amplifier*. Texas Instruments, Post Office Box 655303, Dallas, Texas 75265, 1996.
- [21] Cern. Geant 4: A toolkit for the simulation of the passage of particles through matter. Internet, 2012.
- [22] W.F. Chan, G. Cooper, and C.E. Brion. The electronic spectrum of water in the discrete and continuum regions. absolute optical oscillator strengths for photoabsorption (6-200 ev). *Chemical Physics*, 178(1):387 – 400, 1993.
- [23] J. Choi and J. O. Kang. Basic of particle therapy ii: Relative biological effectiveness. *Radiation Oncology Journal*, 30(1):1–13, 2012.
- [24] L. S. Darken, R. C. Trammell, and T. W. Raudorf. Mechanism for fast neutron damage of ge(jp) detectors. *Nuclear Instruments and Methods*, 171:49–59, 1979.
- [25] S. Devons, G. Manning, and D. S. P. Bunbury. Measurement of γ -transition lifetimes by recoil methods. *Proceedings of the Physical Society*, 18:18–31, 1954.
- [26] M. Dingfelder, D. Hantke, M. Inokuti, and H. G. Paretzke. Electron inelastic-scattering cross sections in liquid water. *Radiation Physics and Chemistry*, 53(1):1 – 18, 1999.
- [27] G.H. Shortley E. U. Condon. *The theory of atomic spectra*. Press syndicate of the university of Cambridge, 1991.
- [28] EG&G ORTEC. *Information about Photon Detectors*. <http://physics.valpo.edu/physLinks/nuclearElectronics/PhotonDetectors.pdf>.

- [29] R. Hobart Ellis, H. H. Rossi, and G. Failla. Stopping power of water films. *Physical Review*, 97(4):1043–47, 1955.
- [30] D. Emfietzoglou, R. Garcia-Molina, I. Kyriakou, I. Abril, and H. Nikjoo. A dielectric response study of the electronic stopping power of liquid water for energetic protons and a new i -value for water. *Physics in Medicine and Biology*, 54(11):3451, 2009.
- [31] D. Emfietzoglou and H. Nikjoo. The effect of model approximations on single-collision distributions of low-energy electrons in liquid water. *Radiation Research*, 163(1):98–111, 2005.
- [32] U. Fano. Penetration of protons, alpha particles, and mesons. *Annual Review of Nuclear Science*, 13(1):1–66, 1963.
- [33] R. B. Firestone. *Table of isotopes*. Wiley-Interscience, 1996.
- [34] W. Friedland. Private communication, 2016.
- [35] J. E. Gentle. *Numerical linear Algebra for application in statistics*. Springer V, 1998.
- [36] R. Gold. *An Iterative Unfolding Method For Response Matrices*. Argonne National Laboratory, 1964.
- [37] R. Gold and E. F. Bennett. Error estimates for iterative unfolding. *Journal of Computational Physics*, 3(2):167 – 175, 1968.
- [38] Goodfellow. *HAVAR-Spec sheet*. Goodfellow, 2015.
- [39] H. Hayashi and N. Hiraoka. Accurate measurements of dielectric and optical function of liquid water and liquid benzene in the vuv region (1-100 ev) using small-angle inelastic x-ray scattering. *The Journal Of Physical chemistry B*, 119:5609–5623, 2015.
- [40] H. Hayashi, N. Watanabe, Y. Udagawa, and C.-C. Kao. The complete optical spectrum of liquid water measured by inelastic x-ray scattering. *Proc. Natl. Acad. Sci. USA*, 97:6264–6266, 2000.
- [41] T Hiraoka, K Kawashima, K Hoshino, and H Bichsel. Energy loss of 70 mev protons in tissue-substitute materials. *Physics in Medicine and Biology*, 39(6):983, 1994.
- [42] H. Hofsäss, H. Binder, T. Klumpp, and E. Recknagel. Doping and growth of diamond-like carbon films by ion beam deposition. *Diamond and Related Materials*, 3:137–142, 1993.

- [43] H. Hofsäss, H. Feldermann, R. Merk, M. Sebastian, and C. Ronning. Cylindrical spike model for the formation of diamond-like thin films by ion deposition. *Appl. Phys. A*, 66:153–181, 1998.
- [44] Prof. Dr. Hans Christian Hofsäss. Private communication, 2016.
- [45] ICRU. *ICRU Report 49, Stopping Powers and Ranges for Protons and Alpha Particles*. International Commission On Radiation Units And Measurements, 1994.
- [46] Texas Instruments. *P82B715 P²C Bus Extender*, 2007.
- [47] I. Kawrakow, E. Mainegra-Hing, D. W. O. Rogers, F. Tessier, and B. R. B. Walters. *The EGSnrc code system: Monte Carlo simulation of electron and photon transport*. NRC, 2013.
- [48] A.J. Koning, S. Hilaire, and M.C. Duijvestijn. “talys-1.0”, proceedings of the international conference on nuclear data for science and technology. *EDP Sciences*, pages 211–214, 2008. April 22-27, 2007, Nice, France, editors O.Bersillon, F.Gunsing, E.Bauge, R.Jacqmin, and S.Leray.
- [49] A. Kraus, J. P. Schiffer, F. W. Prosser, and L. C. Biedenharn. Angular correlation for the $(a, b\gamma)$ -type nuclear reaction. *Phys. Rev.*, 104:1667–1669, 1956.
- [50] A. Lechner, V.N. Ivanchenko, and J. Knobloch. Validation of recent geant4 physics models for application in carbon ion therapy. *Nuclear Instruments and Methods in Physics Research Section B: Beam Interactions with Materials and Atoms*, 268(14):2343 – 2354, 2010.
- [51] W. R. Leo. *Techniques for Nuclear and Particle Physics Experiments*. Springer Verlag Berlin, Heidelberg, New York, 1987. ISBN: 3-540-17386-2.
- [52] T. Liamsuwan and H. Nikjoo. Cross sections for bare and dressed carbon ions in water and neon. *Phys. Med. Biol*, 58:641–72, 2013.
- [53] J. Lindhard, M. Scharff, and H.E. Schiott. Range concepts and heavy ion ranges. (14), 1963.
- [54] M. Matsumoto and T. Nishimura. Mersenne twister. a 623-dimensionally equidistributed uniform pseudorandom number generator. *ACM Transactions on Modeling and Computer Simulation*, 8:3–30, 1998.
- [55] Maxim. *Maxim 127 MAXIM Multi-range, +5V, 12-Bit DAS with 2-Wire Serial Interface*. Maxim Integrated Products, Maxim Integrated Products, 120 San Gabriel Drive, Sunnyvale, CA 94086 408-737-7600, 1998.

- [56] SGS-Thomson Microelectronics. *DMOS Full Bridge Driver*. SGS-Thomson Microelectronics.
- [57] G. E. Mitchell, E. B. Carter, and R. H. Davis. Inelastic scattering of 6- to 19-mev alpha particles from carbon. *Physical Review*, 133:1434–1445, 1963.
- [58] G. Musiol, J. Ranft, R. Reif, and D. Seeliger. *Kern- und Elementarteilchenphysik*. VCH Verlagsgesellschaft, 1988.
- [59] W. Neuwirth, U. Hauser, and Kühn. Energy loss of charged particles in matter: Experimental method and velocity dependence of the energy loss of lithium ions. *Zeitschrift für Physik*, 220:241–264, 1969.
- [60] NIST/SEMATECH. *e-Handbook of Statistical Methods*. U.S. Department of Commerce, 2015. <http://www.itl.nist.gov/div898/handbook/>.
- [61] L. C. Northcliffe. Energy loss and effective charge of heavy ions in aluminium. *Phys. Rev.*, 120:1744–1757, 1960.
- [62] National Institute of Standards. *ASTAR-Manual*. <http://physics.nist.gov/PhysRefData/Star/Text/programs.html>.
- [63] National Research Council. Committee on Nuclear Science. *Studies in Penetration of Charged Particles in Matter*. Its Nuclear science series; report. National Academy of Science-National Research Council, 1964.
- [64] ORTEC. *GMX series coaxial HPGe detector product configuration guide*. ORTEC Advanced Measurement Technology, Oak Ridge Tennessee USA, 2012.
- [65] R. B. J. Palmer and H. A. B. Simons. The experimental determination of the range-energy relations for alpha particles in water and water vapour, and the stopping power of water and water vapour for alpha particles at energies below 8.78 mev. *Proceedings of the Physical Society*, 74(5):585, 1959.
- [66] H. Paul. *Modern practices in radiation therapy*, chapter The Stopping Power of Matter for Positive Ions, pages 113–132. INTECH, InTech Europe University Campus STeP Ri Slavka Krautzeka 83/A 51000 Rijeka, Croatia Phone: +385 (51) 770 447 Fax: +385 (51) 686 166 www.intechopen.com, 2012.
- [67] H. Paul. *The stopping power of matter for positive ions, modern practices in radiation therapy*. InTech, 2012.
- [68] H. Paul and A. Schinner. MSTAR version 3.12. <https://www-nds.iaea.org/stopping/MstarWWW/MSTARInstr.html>.

- [69] H. Paul and A. Schinner. An empirical approach to the stopping power of solids and gases for ions from ${}^3\text{Li}$ to ${}^{18}\text{Argon}$ Part I. *Nuclear Instruments and Methods in Physics Research Section B: Beam Interactions with Materials and Atoms*, 179(3):299 – 315, 2001.
- [70] H. Paul and A. Schinner. An empirical approach to the stopping power of solids and gases for ions from ${}^3\text{Li}$ to ${}^{18}\text{Argon}$ Part II. *Nuclear Instruments and Methods in Physics Research Section B: Beam Interactions with Materials and Atoms*, 195(1-2):166 – 174, 2002.
- [71] R. H. Pehl, N. W. Madden, J. H. Elliott, T. W. Raudorf, R. C. Trammell, and L. S. Darken. Radiation damage resistance of reverse electrode ge coaxial detectors. *IEEE TRANSACTIONS ON NUCLEAR SCIENCE*, 26:321–323, 1979.
- [72] V. K. Rasmussen, C. C. Laritsen, and T. Lauritsen. Doppler broadening of a gamma-ray line. *Physical Review*, 75:199–200, 1949.
- [73] T. W. Raudorf and R.H. Pehl. Effect of charge carrier trapping on germanium coaxial detector line shapes. *Nuclear Instruments & Methods in Physics Research, Section A: Accelerators, Spectrometers, Detectors, and Associated Equipment*, 255:538–551, 1987.
- [74] H. K. Reynolds, D. N. F. Dunbar, W. A. Wenzel, and W. Whaling. The stopping cross section of gases for protons, 30-600 kev. *Phys. Rev.*, 92:742–748, 1953.
- [75] R. H. Ritchie, R. N. Hamm, J. E. Turner, H. A. Wright, and W. E. Bolch. *Physical and Chemical Mechanisms in Molecular Radiation Biology*, chapter Radiation Interactions and Energy Transport in the Condensed Phase, pages 99–135. Springer US, Boston, MA, 1991.
- [76] C. Ronning and H. Hofsäss. Mass separated ion beam deposition: a unique technique to grow dlc, cbn and cn thin films. *Diamond Materials IV, The Electrochemical Society*, 4:359–364, 1995.
- [77] Arduino SA. Arduino project, 2015. <http://www.arduino.cc/>.
- [78] Thomas Schaerer. *Operationsverstärker und Instrumentationsverstärker*. Elektronik Kompendium, 2002.
- [79] D. Schardt, P. Steidl, M. Krämer, U. Weber, K. Parodi, and S. Brons. Precision bragg-curve measurements for light-ion beams in water. Scientific report, Gesellschaft f. Schwerionenforschung, Darmstadt, Germany, 2007.

- [80] W. Schauer. *Untersuchung zur Kernstruktur von ^{122}Te , Aufbau eines Mikrostreifen-Gas-Detektors für den Münchener Q3D-Magnetspektrographen*. Herbert Utz Verlag Wissenschaft, 1997.
- [81] G. Schiwietz and P. L. Grande. Improved charge-state formulas. *Nuclear Instruments and Methods in Physics Research Section B: Beam Interactions with Materials and Atoms*, 175–177:125 – 131, 2001. Twelfth International Conference of Ion Beam Modification of Materials.
- [82] G. Schiwietz and P. L. Grande. Introducing electron capture into the unitary-convolution-approximation energy-loss theory at low velocities. *Phys. Rev. A*, 84(5):052703, 2011.
- [83] E. Schmitt, W. Friedland, P. Kunderát, M. Dingfelder, and A. Ottolenghi. Cross-section scaling for track structure simulation of low-energy ions in liquid water. *Radiat Prot Dosimetry*, 166(1-4):15–18, 2015.
- [84] E. Schmitt, W. Friedland, P. Kunderát, and M. Dingfelder. Track-structure modelling for low-energy light ions in PARTRAC. In *MICROS 2013*, 2013.
- [85] ON Semiconductor. *BC549B,C and BC550B,C low noise Transistors*. Semiconductor Components Industries, LLC (SCILLC), P.O. Box 5163, Denver, Colorado 80217 USA, 2015.
- [86] W.t. Sharp, J.M. Kennedy, B.J. Sears, and M.G. Hoyle. *Tables of coefficients for angular distribution analysis, Report No. 97*. Atomic energy of Canada: Ltd, Chalk River, 1954.
- [87] M. Shimizu, T. Hayakawa, M. Kaneda, H. Tsuchida, and A. Itoh. Stopping cross-sections of liquid water for 0.3 – 2 MeV protons. *Vacuum*, 84(8):1002 – 1004, 2010.
- [88] M. Shimizu, M. Kaneda, T. Hayakawa, H. Tsuchida, and A. Itoh. Stopping cross sections of liquid water for MeV energy protons. *Nuclear Instruments and Methods in Physics Research B*, 267:2667–2670, 2009.
- [89] P. Sigmund and A. Schinner. binary theory of electronic stopping. *Nucl. Instrum. Methods B*, 195(64), 2002.
- [90] P. Sigmund and A. Schinner. binary theory of light-ion stopping. *Nucl. Instrum. Methods B*, 193(49), 2002.
- [91] P. Sigmund, A. Schinner, and H. Paul. Errata and addenda for ICRU report 73, stopping of ions heavier than helium. *ICRU Journal*, 5(1), 2009. <http://icru.org/testing/reports/errata-and-addenda-icru-report-73-stopping-of-ions-heavier-than-helium>.

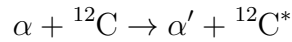
- [92] T. Siiskonen, H. Kettunen, K. Peräjärvi, A. Javanainen, M. Rossi, W. H. Trzaska, J. Turunen, and A. Virtanen. Energy loss measurement of protons in liquid water. *Physics in Medicine and Biology*, 56:2367–2374, 2011.
- [93] A. Simon and T. A. Welton. Production of polarized particles in nuclear reactions. *Phys. Rev.*, 90:1036–1043, 1953.
- [94] J.R. Taylor. *Scattering Theory*. John Wiley and Sons, 1972.
- [95] D. I. Thwaites. Stopping cross-sections of liquid water and water vapour for alpha particles within the energy region 0.3 to 5.5 mev. *Phys. Med. Biol*, 26(1):71–80, 1981.
- [96] D.R. Tilley, H.R. Weller, and C.M. Cheves. Energy levels of light nuclei $a = 16$. *Triangle Universities*, 2000.
- [97] W. A. Wenzel and W. Whaling. The stopping cross section of d_2O ice. *Phys. Rev.*, 87:499–503, 1952.
- [98] Y. J. Xu, G. S. Khandelwal, and J. W. Wilson. Proton stopping cross sections of liquid water. *Phys. Rev. A*, 32(1):629–632, 1985.
- [99] J. F. Ziegler. Stopping and range of ions in matter (SRIM2013), 2013. <http://www.srim.org/>.
- [100] J.F. Ziegler. The stopping of energetic light ions in elemental matter. *J. Appl. Phys. / Rev. Appl. Phys*, 85:1249 – 1272, 1999.

Appendix A

Kinematics of the scattering processes

In this work, the γ -detector was positioned at 0° relative to the α -beam axis so that only those γ -quanta whose emission angle φ is equal to the flight angle ϑ of $^{12}\text{C}^*$ could be detected.

As the nuclear reaction



used in the present work is of two-particle kinematics, the initial velocity of the carbon nuclei is a function of their flight angle:

$$v_0 = f(\vartheta). \quad (\text{A.1})$$

In the following, this function is derived using the energy and momentum conservation law. The energy balance of the reaction is given by

$$m_\alpha c^2 + T_\alpha + mc^2 + T = m'_\alpha c^2 + T'_\alpha + m'c^2 + T', \quad (\text{A.2})$$

where T and T' is the kinetic energy of the carbon nucleus and T_α and T'_α is the kinetic energy of the α -particle before and after the reaction, respectively. In the non-relativistic case ($v_0 \ll c$), the mass of the alpha particle is conserved and therefore $m_\alpha = m'_\alpha$. Furthermore, the carbon nucleus is assumed to be in rest before the collision: $T = 0$. The velocity can be separated into a horizontal component v_z along the α -beam axis and a perpendicular component v_y . Due to the conservation of the momentum, the y -component has to be zero:

$$v_z = \sqrt{2m_\alpha T_\alpha} = \sqrt{2m'T'} \cos \vartheta + \sqrt{2m'_\alpha T'_\alpha} \cos \vartheta_\alpha, \quad (\text{A.3a})$$

$$v_y = 0 \rightarrow \sqrt{2m'T'} \sin \vartheta = \sqrt{2m'_\alpha T'_\alpha} \sin \vartheta_\alpha. \quad (\text{A.3b})$$

The relation $\cos^2 \vartheta_\alpha = 1 - \sin^2 \vartheta_\alpha$ and the substitution of A.3b into A.3a lead to

$$m'_\alpha T'_\alpha = m_\alpha T_\alpha - 2\sqrt{m_\alpha T_\alpha m'T'} \cos \vartheta + m'T'. \quad (\text{A.4})$$

The mass difference between m' and m in equation A.2 corresponds to the reaction Q -value:

$$\begin{aligned} T'_\alpha &= T_\alpha - T' + (m - m')c^2 \\ &= T_\alpha - T' + Q. \end{aligned} \quad (\text{A.5})$$

The energy of the incoming α -particle therefore is shared between the scattered α -particle, the carbon nucleus and the excitation energy Q . The substitution of equation A.5 into equation A.4 gives

$$0 = T' - 2 \frac{\sqrt{m_\alpha T_\alpha m}}{m_\alpha + m} \cos \vartheta \sqrt{T'} - \frac{m_\alpha Q}{m_\alpha + m}. \quad (\text{A.6})$$

Equation A.6 can be considered as a quadratic equation with $T' = x^2$, resulting in two solutions for

$$[T'(\vartheta)]_{1,2} = \left[\frac{\sqrt{m_\alpha T_\alpha m}}{m_\alpha + m} \cos \vartheta \pm \sqrt{\frac{m_\alpha T_\alpha m}{(m_\alpha + m)^2} \cos^2 \vartheta + \frac{m_\alpha Q}{m_\alpha m}} \right]^2. \quad (\text{A.7})$$

The two solutions of equation A.7 provide the maximum and minimum energy transfer to the carbon nucleus at a scattering angle of $\vartheta = 0^\circ$. The solution of equation A.7 is valid as long as the expression contained in the second square root of equation A.7 is ≥ 0 . This condition can be used to derive the maximum flight angle of the carbon nuclei:

$$\begin{aligned} 0 &= \frac{m_\alpha T_\alpha m}{(m_\alpha + m)^2} \cos^2 \vartheta + \frac{Q m_\alpha}{m_\alpha + m} \\ \Rightarrow \vartheta_{\max} &= \arccos \left(\sqrt{-\frac{Q}{T_\alpha} - \frac{Q m_\alpha}{m T_\alpha}} \right). \end{aligned} \quad (\text{A.8})$$

Appendix B

Angular resolution

The γ -emission angle φ defines the half opening angle of a cone around the flight angle ϑ of the $^{12}\text{C}^*$ projectile (see also figure B.1).

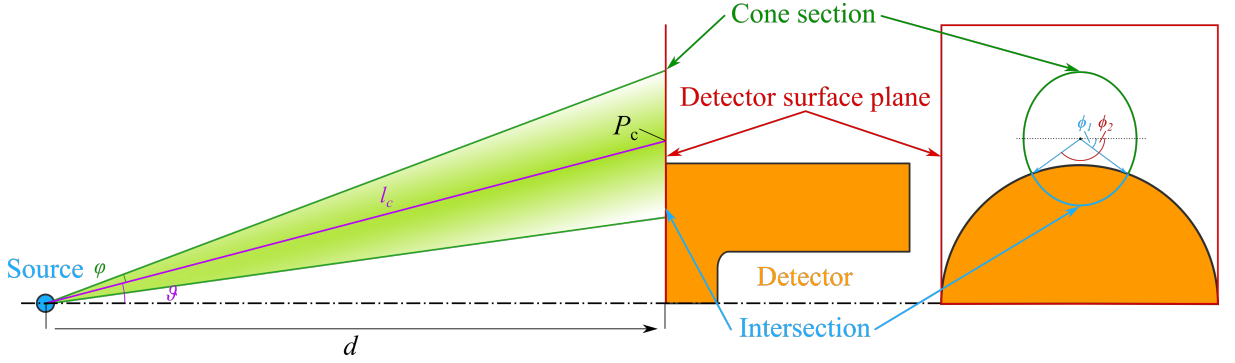


Figure B.1: Sketch of the cone built by the flight angle ϑ of the $^{12}\text{C}^*$ projectiles and the γ -emission angle φ that defines the half opening angle of the cone. The frontal view shows the ellipse on the detector surface plane.

For $\varphi + \vartheta < \pi/2$, the envelope of the cone intersecting with the detector surface plane is an ellipse. The ellipse has a parameter representation is given by

$$\underline{E} = \begin{pmatrix} b \sin \phi \\ P_{e,y} + a \cos \phi \\ d \end{pmatrix}. \quad (\text{B.1})$$

The quantities a and b are the semi-axes of the ellipse. The quantity d is the distance between the source and the detector and $P_{e,y}$ is the distance between the ellipse centre and the detector centre:

$$P_{e,y} = \frac{1}{2}d (\tan(\vartheta + \varphi) + \tan(\vartheta - \varphi)). \quad (\text{B.2})$$

In case the ellipse is completely within the circular detector front face, the parameter ϕ would cover the interval $[0, 2\pi]$. In most cases, this is not the case and the perimeter of the ellipse intersects the circumference of the circular boundary of the detector front

surface. Here, the range of ϕ depends on the flight angle ϑ and the opening angle φ . The major semi-axis a for a given distance between the source and the detector surface d , flight angle ϑ of the $^{12}\text{C}^*$ projectile and emission angle φ of the γ -quanta is:

$$a = \frac{1}{2}d(\tan(\vartheta + \varphi) - \tan(\vartheta - \varphi)). \quad (\text{B.3})$$

For the calculation of the minor semi-axis b a cone base with the radius r'_c has to be considered which intersects with the detector surface plane at the centre of the ellipse P_e as shown in figure B.2.

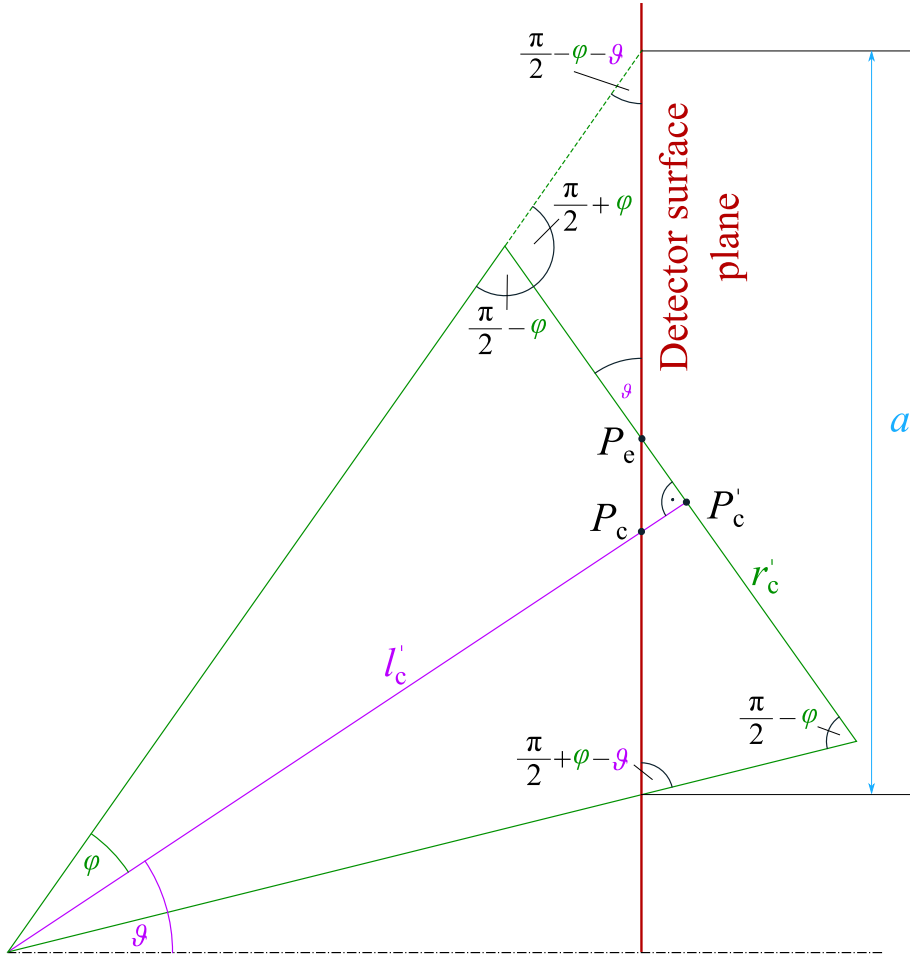


Figure B.2: Side view of the cone which intersects with the detector surface plane at the centre of the ellipse P_e .

The height of this cone is given by

$$l'_c = l_c + \overline{P_c P_e} \sin \vartheta. \quad (\text{B.4})$$

The distance l_c between the origin of the cone and the point P_c where the cone central axis intersects with the detector surface plane, is given by the distance of the source d

and the flight angle ϑ of the $^{12}\text{C}^*$ projectile:

$$l_c = \frac{d}{\cos \vartheta}. \quad (\text{B.5})$$

The distance between the points where the cone central axis and the ellipse centre intersects with the detector surface plane is given by:

$$\overline{P_c P_e} = P_{e,y} - P_{c,y}, \quad (\text{B.6})$$

with

$$P_{c,y} = d \tan \vartheta \quad (\text{B.7})$$

and $P_{e,y}$ given by equation B.2. Using equation B.2 and equation B.4 gives

$$l'_c = \frac{l_c}{1 - \tan^2 \varphi \tan^2 \vartheta}. \quad (\text{B.8})$$

The intersection of the cone with the detector front surface plane at the point P_e , where the minor axis of the ellipse is defined, results in a cone which base is a circle with a radius given by

$$r'_c = l'_c \tan \varphi. \quad (\text{B.9})$$

At the same time (see also figures B.2, B.3):

$$r_c'^2 = b^2 + \overline{P'_c P_e}^2 \quad (\text{B.10})$$

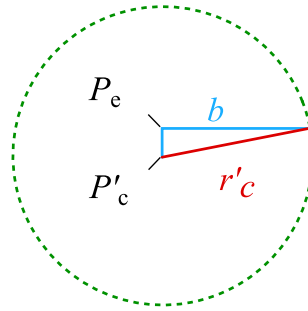


Figure B.3: View of the cone base which intersects with the detector surface plane at the centre of the ellipse P_e showing the minor semi-axis b and its associated quantities.

For the calculation of the minor semi-axis b , $\overline{P'_c P_e}$ has to be determined first. It is given by:

$$\overline{P'_c P_e} = \overline{P_c P_e} \cos \vartheta. \quad (\text{B.11})$$

Combination and rearrangement of equations B.9, B.10 and B.11 gives for the minor semi-axis:

$$b = \sqrt{((\overline{P_c P_e} \sin \vartheta + l_c) \tan \varphi)^2 - (\overline{P_c P_e} \cos \vartheta)^2} \quad (\text{B.12})$$

The angle ϕ appearing in equation B.1 can take values $\phi = [0, 2\pi]$ if all ellipse coordinates satisfy the equation:

$$r_D \geq \sqrt{(b \cos \phi)^2 + (a \sin \phi + \overline{P_c P_e})^2} \quad \forall \phi \in [0, 2\pi]. \quad (\text{B.13})$$

If not, the valid range of ϕ has to be calculated. It defines an ellipse segment on the detector surface. The limits of ϕ can be determined by equating the parameter representation of the detector–front perimeter with that of the ellipse. Here, only the x and y component have to be considered as $z = d$ is constant. This results in two equations:

$$\begin{aligned} \text{I} \quad r_D \cos \Phi &= b \cos \phi \\ \text{II} \quad r_D \sin \Phi &= a \sin \phi + \overline{P_c P_e} \end{aligned} \quad (\text{B.14})$$

leading to

$$r_D^2 = (a \sin \phi + \overline{P_c P_e})^2 + b^2 \cos^2 \phi \quad (\text{B.15})$$

Further rearrangement results in the quadratic equation

$$0 = \sin^2 \phi + 2 \frac{a \overline{P_c P_e}}{a^2 - b^2} \sin \phi + \frac{\overline{P_c P_e}^2 + b^2 - r_D^2}{a^2 - b^2}, \quad (\text{B.16})$$

which provides the solution of the angle ϕ at which the ellipse cuts the detector boundaries. These solutions define the integration limits on the arc of the ellipse:

$$u_{1,2} = -\frac{a \overline{P_c P_e}}{a^2 - b^2} \pm \sqrt{\left(\frac{a \overline{P_c P_e}}{a^2 - b^2}\right)^2 - \frac{\overline{P_c P_e}^2 + b^2 - r_D^2}{a^2 - b^2}}, \quad (\text{B.17})$$

where only solutions are valid which are between -1 and 1 due to the definition range of the arcsine function, see equation B.16. It can be shown that

$$-\frac{a \overline{P_c P_e}}{a^2 - b^2} = \frac{1}{\tan \vartheta \tan \varphi}. \quad (\text{B.18})$$

The requirement that $(\vartheta + \varphi) < \pi/2$ implies that $\tan \vartheta \tan \varphi < 1$ and hence the value u_2 will always give values < -1 . Therefore, only the other solution u_1 can give values ϕ in equation B.16 if $-1 \leq u_1 \leq 1$. These values are given by:

$$\phi_1 = \arcsin u_1 \quad \text{and} \quad \phi_2 = \pi - \arcsin u_1 \quad (\text{B.19})$$

The matrix elements of $\underline{\underline{M}}_B$ (see also section 6.3) can be calculated by:

$$m_{ij,B} = G_{ij}(\phi_{ij,1}, \phi_{ij,2}, \eta_F(r), \varepsilon(a_{ij}, b_{ij})) \Delta \varphi_j \quad (\text{B.20})$$

where ε is the numerical eccentricity:

$$\varepsilon = \sqrt{1 - \frac{b^2}{a^2}} \quad \text{and} \quad a, b = f(\vartheta, \varphi, d), \quad (\text{B.21})$$

where the coefficients a and b have to be parametrised for each matrix element $m_{ij,B}$. In equation B.20, $\eta_F(r)$ is the radially dependent detection efficiency shown in figure 5.5. The quantity $\Delta\varphi_j$ is the bin width in the angular spectra $dN/d\varphi$ and Λ_{ij} is the arc of the ellipse which is projected onto the detector surface weighed with the radial dependent detection efficiency:

$$G_{ij} = a_{ij} \int_{\phi_{ij,1}}^{\phi_{ij,2}} \eta_F(r(\phi')) \sqrt{1 - \varepsilon^2 \sin^2 \phi'} d\phi'. \quad (\text{B.22})$$

As the integral given in equation B.22 is an elliptical integral and cannot be solved analytically it has to be solved using a series expansion or a numerical approach which was used in this work.

In the case that the γ -emission angle is not a valid solution for a given γ -energy or if the ellipse does not cut the detector surface the matrix element $m_{ij,B} = 0$.

Appendix C

Angular correlation

Measurements have shown (see section 4.1 page 45) that the unattenuated γ -energy spectra and consequently, the start velocity distribution of $^{12}\text{C}^*$ projectiles strongly depend on the primary energy of α -projectiles in a certain energy range. To keep the uncertainties arising due to the instability of α -beam energy as small as possible, it is advantageous to use primary α -particle energies at which the energy dependence of the flight angle distribution is negligible. Therefore, it is crucial to determine if the alteration of the spectral shape is caused by experimental artefacts and inaccuracies, or if they can be explained by a physical model. In this section, the dependence on the primary α -particle energy of the unattenuated γ -energy spectra is theoretically studied.

C.1 Angular distribution of $^{12}\text{C}^*$ projectiles in the centre of mass system

Using the non relativistic form of Doppler equation

$$E_\gamma = E_0 \left(1 + \frac{v_z}{c}\right) \rightarrow dE_\gamma = \frac{1}{c} E_0 dv_z \quad (\text{C.1})$$

the Doppler-shifted γ -energy distribution dN/dE_γ can be converted into the velocity distribution of $^{12}\text{C}^*$ projectiles:

$$\frac{dN}{dE_\gamma} = \frac{c}{E_0} \frac{dN}{dv_z} \quad (\text{C.2})$$

where v_z is the z -component of the velocity vector in the lab frame. It can be written as the sum of the velocities v_s of the centre of mass and the z component $v_{z,s}$ of the velocity of $^{12}\text{C}^*$ projectiles in the centre of mass system:

$$v_z = v_s + v_{z,s} \quad (\text{C.3})$$

As there is no external force, the velocity of the centre of mass is constant. Therefore, $dv_z = dv_{z,s}$ and $v_{z,s} = |v| \cos \vartheta$ where it is assumed that $^{12}\text{C}^*$ projectiles are produced with the same velocity $|v|$ in the centre of mass system. The insertion of these relations into equation C.2 gives

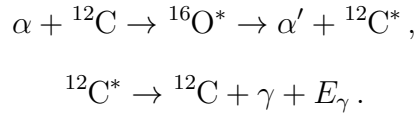
$$\frac{dN}{dE_\gamma} = \frac{c}{E_0|v|} \frac{dN}{d \cos \vartheta} = \frac{c}{E_0|v|} \sin(\vartheta)^{-1} \frac{dN}{d\vartheta}. \quad (\text{C.4})$$

It should be noted that ϑ is here is the flight angle of $^{12}\text{C}^*$ projectiles in the centre of mass system. With $d\Omega = 2\pi \sin \vartheta d\vartheta$, the measured Doppler-shifted γ -energy distribution can be transformed into the angular distribution of the carbon nuclei in the centre of mass system:

$$\frac{dN}{d\Omega} = \frac{1}{2c\pi} E_0|v| \frac{dN}{dE_\gamma}. \quad (\text{C.5})$$

C.2 Energy levels of the compound nucleus

The reaction which is used for the production of the excited carbon nuclei occurs via a compound nucleus [7]:



The reaction stages are illustrated in figure C.1. In the case of a compound nucleus reaction the decay of the nucleus is independent on its creation [14].

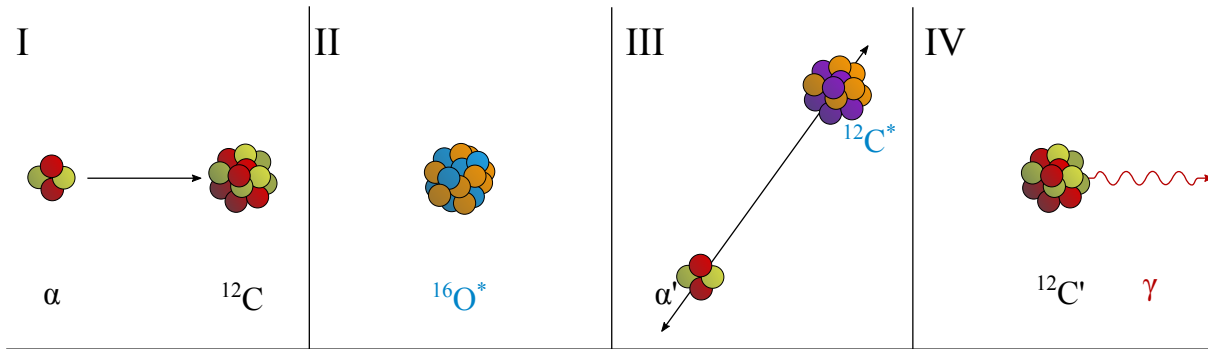


Figure C.1: Illustration of compound reaction: I: Collision of the α -projectile with the carbon target, II: formation of an excited oxygen compound nucleus, III: decay of the compound system, where the carbon nucleus remains in its first excited state. IV: Decay of the excited carbon nucleus into the ground state by a γ -decay.

The angular momentum of the excited compound nucleus and its parity play the decisive role for the angular distribution of the $^{12}\text{C}^*$ projectiles. In the case of the reaction ${}^{12}\text{C}(\alpha, \alpha'){}^{12}\text{C}^*$, the total angular momentum of the compound nucleus ${}^{16}\text{O}^*$ in the centre of mass system is given by the spin of the excited state in ${}^{16}\text{O}^*$. Since α -particles as well as ${}^{12}\text{C}$ have no spin, the spin of ${}^{16}\text{O}^*$ can only arise from the angular momenta of the

reaction partners. Each energy level of $^{16}\text{O}^*$ is associated with a distinct spin.

The excitation energy of the compound system is given by

$$E_{\text{ex}} = T_{\alpha,s} - Q \quad (\text{C.6})$$

where Q is the reaction energy and $T_{\alpha,s}$ is the kinetic energy of the reaction partners in the centre of mass system given by:

$$T_{\alpha,s} = T_{\alpha} \frac{m}{m + m_{\alpha}}, \quad (\text{C.7})$$

where T_{α} is the kinetic energy of the incident α -particle in the laboratory system. The reaction energy Q can be derived from the mass defect of the formed system:

$$Q = [(A_{16\text{O}} - Z_{16\text{O}})m_n + Z_{16\text{O}}m_p - m_{16\text{O}}]c^2 = -7.161 \text{ MeV}, \quad (\text{C.8})$$

where m_p and m_n are the mass of proton and neutron, respectively. The quantity $m_{16\text{O}}$ is the mass of the compound system in its ground state, $A_{16\text{O}}$ is the mass number and $Z_{16\text{O}}$ is the atomic number of the compound system.

By comparison of the excitation energy given by equation C.6 and the level energies shown in table C.1 the possible levels which can be occupied were chosen. For an isolated

$E_{\text{ex}} / \text{MeV}$	$\Delta E_{\text{ex}} / \text{keV}$	J^{π}	Γ / keV	$\Delta\Gamma / \text{keV}$
14.100	100	3^{-}	750	200
14.302	3	4^{-}	34	12
14.399	2	5^{+}	27	5
14.620	20	4^{+}	490	15
14.660	20	5^{-}	670	15
14.815	2	6^{+}	70	8
14.926	2	2^{+}	54	5
15.097	5	0^{+}	166	30
15.196	3	2^{-}	63	4
15.260	50	2^{+}	300	100
15.408	2	3^{-}	132	7
15.785	5	3^{+}	40	10
15.828	30	3^{-}	700	120
16.200	90	1^{-}	580	60
16.209	2	1^{+}	19	3
16.275	7	6^{+}	420	20
16.352	8	2^{+}	61	8
16.442	2	2^{+}	25	2
16.817	2	3^{+}	28	3
16.844	21	4^{+}	570	60
16.930	50	2^{+}	280	—

Table C.1: Section of the energy levels of ^{16}O adapted from [96].

system, the parity π is conserved. It is given by:

$$\pi = (-1)^{\Delta\ell + \Delta s} \quad (\text{C.9})$$

with the orbital angular momentum transfer $\Delta\ell$ and the contribution of the spin flip Δs . The parity is called natural if $\Delta s = 0$, else it is called not natural. For interaction of spinless reaction partners such as α -particle and ^{12}C , only natural parities can be occupied [80].

As the flight-angle distribution of $^{12}\text{C}^*$ projectiles described by equation C.5 is obtained by observing the γ -quanta in a given direction and the direction of motion of $^{12}\text{C}^*$ projectiles is opposite to that of the α -particles in the centre of mass system, the flight angle distribution of $^{12}\text{C}^*$ projectiles reflects the α - γ angle correlation function $W(\vartheta, \varphi)$. Here, ϑ is the flight angle of $^{12}\text{C}^*$ projectiles and φ is the gamma emission angle which is the same in the centre of mass system and laboratory system. The function $W(\vartheta, \varphi)$ was calculated using the formalism of Kraus *et al.* [49]:

$$\begin{aligned} W(\vartheta, \varphi) = & \sum_k \frac{1}{2} \frac{\lambda_p^2}{2\varsigma + 1} S(\varsigma\ell_1, \varsigma'_1\ell'_1; J_1\Pi_1) S^*(\varsigma\ell_2, \varsigma'_2\ell'_2; J_2\Pi_2) \\ & \times \langle J_{t,f} | \hat{H}(L_1) | J'_{t,1} \rangle \langle J_{t,f} | \hat{H}(L_2) | J'_{t,2} \rangle^* \\ & \times (-1)^t (-2)(2J_{t,f} + 1) i^p \langle \ell'_1\ell'_2 00 | \Lambda 0 \rangle W_R(\varsigma'_1 J'_{t,1} \varsigma'_2 J'_{t,2}; I'_p \Delta) W_R(J'_{t,1} L_1 J'_{t,2} L_2; J_{t,f} \Delta) \\ & \times \sqrt{(2J_1 + 1)(2J_2 + 1)(2\ell'_1 + 1)(2\ell'_2 + 1)(2\varsigma'_1 + 1)(2\varsigma'_2 + 1)(2L_1 + 1)(2L_2 + 1)} \\ & \times Z(\ell_1 J_1 \ell_2 J_2; \varsigma \Gamma) X \begin{pmatrix} J_1 & \varsigma'_1 & \ell'_1 \\ J_2 & \varsigma'_2 & \ell'_2 \\ \Gamma & \Delta & \Lambda \end{pmatrix} \langle L_1 L_2 1 - 1 | \Delta 0 \rangle Y_\Lambda^\eta(\vartheta, \phi) \langle \Lambda \Delta \eta - \eta | \Gamma 0 \rangle Y_\Delta^{-\eta}(\varphi, \Phi), \end{aligned} \quad (\text{C.10})$$

with W_R denoting the Racah coefficient. In equation C.10, ς is the incoming channel spin that is zero in the present case and ς' designates the outgoing channel spin. The outgoing channel spin can have values $|J - I'_p| \leq \varsigma' \leq J + I'_p$ where J is the spin of the compound nucleus and I'_p is the spin of the α -particle. As I'_p is zero, the outgoing channel spin is given by the spin of the compound nucleus. The letter ℓ stands for the relative angular momentum of the reaction partners. L is the multiplicity of the γ -quantum which is 2 in the case of the first excited state of ^{12}C . The term S designates the S matrix for the reaction whose square of the absolute value is proportional to the reaction cross section. The first S matrix in equation C.10 describes the reaction amplitude for the incoming channel spin ς_1 with relative angular momentum ℓ_1 and the outgoing channel spin ς'_1 with relative angular momentum ℓ'_1 leading to the spin J_1 and parity Π_1 of the compound nucleus. The second conjugated S matrix can be interpreted in similar way. In the present work, only one spin state of ^{16}O is considered and the multiplicity of the γ -quantum is uniquely defined, in other words $L_1 = L_2$. Therefore, the term

$SS^* \times \langle J_{t,f} | \hat{H}(L_1) | J'_{t,1} \rangle \langle J_{t,f} | \hat{H}(L_2) | J'_{t,2} \rangle^*$ is a constant value that does not influence the shape of the angular correlation function.

The coefficient Z is given by [86] [49]:

$$Z(\ell_1 J_1 \ell_2 J_2; \varsigma \Gamma) = \Re \left\{ \exp \left[\frac{1}{2} \pi (\ell_2 - \Pi_2 - \ell_1 + \Pi_1 + \Gamma + 2) \right] \langle \ell_1 \ell_2 - 11 | \Gamma 0 \rangle \right. \\ \left. \times \sqrt{(2\ell_1 + 1)(2\ell_2 + 1)(2J_1 + 1)(2J_2 + 1)} W_R(\ell_1 J_1 \ell_2 J_2; \varsigma \Gamma) \right\}, \quad (\text{C.11})$$

The coefficient X was taken from the papers [93] and [49].

$$X \begin{pmatrix} J_1 & \varsigma'_1 & \ell'_1 \\ J_2 & \varsigma'_2 & \ell'_2 \\ \Gamma & \Delta & \Lambda \end{pmatrix} = \sum_v (2v + 1) W_R(J_1 \varsigma'_1 \Lambda \ell'_2; \ell'_1 v) W_R(J_2 \ell'_2 \Delta \varsigma'_1; \varsigma'_2 v) W_R(J_1 J_2 \Lambda \Delta; \Gamma v). \quad (\text{C.12})$$

The sum given in equation C.10 has to be evaluated over the vector

$$\underline{k} = (\varsigma, \ell_1, \ell_2, J_1, J_2, \ell'_1, \ell'_2, \varsigma'_1, \varsigma'_2, J'_{t,1}, J'_{t,2}, L_1, L_2, \Gamma, \Delta, \Lambda, \eta)$$

where the indices Λ , Δ , η and Γ are integers that can have the following values:

$$\Lambda = [0, \dots, \ell'_1 + \ell'_2] \\ \Delta = [0, \dots, L_1 + L_2] \\ \eta = \begin{cases} [-\Lambda, \dots, \Lambda] & \text{if } \Lambda \leq \Delta \\ [-\Delta, \dots, \Delta] & \text{if } \Delta < \Lambda \end{cases}$$

and $|\Lambda - \Delta| \leq \Gamma \leq (\Lambda + \Delta)$.

As the emission angle $(\varphi, \Phi) = (0^\circ, 0^\circ)$ is known, the distribution of $^{12}\text{C}^*$ projectiles as function of ϑ can be calculated using equation C.10.

C.3 Comparison and results

The angular correlation was obtained by the weighted sum of angular correlation functions W_{J_i, ℓ'_i} where the relative angular momentum can have values given by $|J - L| \leq \ell \leq J + L$:

$$W_{\text{tot}}(\theta) = \sum_i w_i W_{J_i, \ell'_i}(\theta) \quad (\text{C.13})$$

The absolute value of the weighting coefficients w_i are related to the strength of the corresponding transition. Due to the repulsive centrifugal potential which is proportional to $\ell(\ell + 1)$ [94], the transition probability rapidly decreases with increasing ℓ' . Therefore, for $J \geq 3$, only the two lowest values of ℓ' were used.

For the determination of the levels which can be occupied by the reaction, the excitation energy in the centre of mass system has to be determined (see equation C.6). This energy can then be used in combination with the energy levels of the compound system given in table C.1. In the case of energy levels that have large width and overlap with neighbouring levels, two or more energy levels with different spins and parities have been taken into account. It has to be mentioned that equation C.10 only takes into account the coherent coupling of two reaction channels. In general, however, more than two reaction channels with different angular momenta may be involved in the decay of the compound nuclei. The consideration of all possible reaction channels is, however, theoretically very difficult. Therefore, the number of involved channels was at first restricted to two in order to allow the usage of the formalism of by Kraus *et al.* [49].

In this work, it was tried to take into account the coherent interference by other reaction channels by means of weighting coefficients which reflect not only the amplitude but also the phase difference between various reaction channels. Hence, the values of the coefficients may also be negative. The coefficient values were determined by the best fit of the experimental angular distribution by the weighted sum of the theoretical distributions calculated using equation C.10.

It can be seen from figure C.2 that the fitted and measured distribution show an excellent agreement for all energies. Although the approach used here may be only a rough approximation if more than two reaction channels are involved, the good reproduction of the experimental angular distributions by the present approach indicates that it may be used to explain and predict the correlation of the flight angles of $^{12}\text{C}^*$ projectiles and the γ -quanta emission angles. The corresponding obtained weighting coefficients are given in the tables C.2 to C.7.

The theoretical explanation of the angular correlation function, and consequently, that of the unattenuated γ -energy spectra dN_u/dE_γ facilitates finding the α -particle energy region where dN_u/dE_γ does not noticeably change with the α -particle energy. Furthermore, it enables the estimate of the uncertainty arising due to the fluctuation of the α -beam energy.

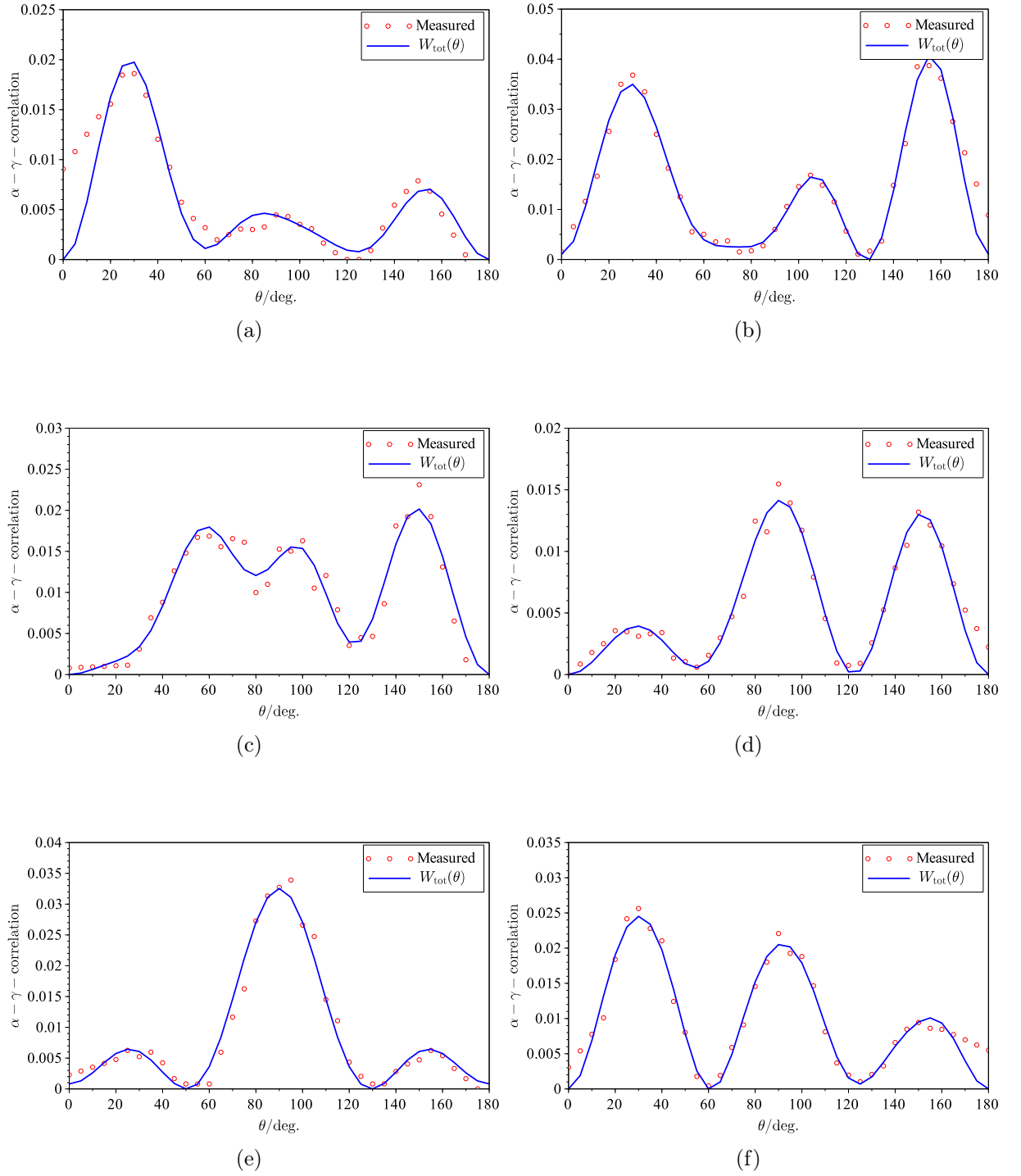


Figure C.2: Angular correlation function in comparison with the measured γ -energy spectra transformed to the angular distribution of the carbon nuclei in the centre of mass system (see also equation C.5) for primary α -particle energies (a) $T_\alpha = 10.1$ MeV, (b) $T_\alpha = 10.2$ MeV, (c) $T_\alpha = 10.3$ MeV, (d) $T_\alpha = 10.5$ MeV, (e) $T_\alpha = 10.95$ MeV and (f) $T_\alpha = 11.57$ MeV.

$W_{J_i, \ell'_i}(\theta)$	w_i
$J = 3, \ell' = 3$	$4.2652 \cdot 10^{-1}$
$J = 4, \ell' = 4$	$4.2737 \cdot 10^{-2}$
$J_1 = 3, \ell'_1 = 3, J_1 = 4, \ell'_1 = 4$	$5.9995 \cdot 10^{-4}$
$J_1 = 3, \ell'_1 = 3, J_1 = 4, \ell'_1 = 2$	$-5.1679 \cdot 10^{-4}$
$J_1 = 3, \ell'_1 = 3, J_1 = 5, \ell'_1 = 3$	$4.6345 \cdot 10^{-1}$
$J_1 = 4, \ell'_1 = 4, J_1 = 4, \ell'_1 = 2$	$-3.1177 \cdot 10^{-2}$
$J_1 = 5, \ell'_1 = 5, J_1 = 5, \ell'_1 = 3$	$3.4998 \cdot 10^{-2}$

Table C.2: Coefficients for α - γ -correlation function for $E_\alpha = 10.1$ MeV.

$W_{J_i, \ell'_i}(\theta)$	w_i
$J = 3, \ell' = 3$	$3.0469 \cdot 10^{-1}$
$J = 3, \ell' = 1$	$-6.2734 \cdot 10^{-2}$
$J = 6, \ell' = 6$	$1.0094 \cdot 10^{-2}$
$J = 6, \ell' = 4$	$3.4189 \cdot 10^{-1}$
$J_1 = 3, \ell'_1 = 3, J_1 = 3, \ell'_1 = 1$	$-2.1230 \cdot 10^{-2}$
$J_1 = 3, \ell'_1 = 3, J_1 = 6, \ell'_1 = 6$	$-6.0237 \cdot 10^{-2}$
$J_1 = 3, \ell'_1 = 3, J_1 = 6, \ell'_1 = 4$	$-4.3992 \cdot 10^{-3}$
$J_1 = 3, \ell'_1 = 1, J_1 = 6, \ell'_1 = 6$	$1.1411 \cdot 10^{-1}$
$J_1 = 3, \ell'_1 = 1, J_1 = 6, \ell'_1 = 4$	$7.0816 \cdot 10^{-2}$
$J_1 = 6, \ell'_1 = 6, J_1 = 6, \ell'_1 = 4$	$9.7996 \cdot 10^{-3}$

Table C.3: Coefficients for α - γ -correlation function for $E_\alpha = 10.2$ MeV.

$W_{J_i, \ell'_i}(\theta)$	w_i
$J = 3, \ell' = 3$	$1.1888 \cdot 10^{-1}$
$J = 3, \ell' = 1$	$-2.2543 \cdot 10^{-1}$
$J = 2, \ell' = 2$	$1.7897 \cdot 10^{-1}$
$J = 2, \ell' = 4$	$1.0502 \cdot 10^{-4}$
$J_1 = 3, \ell'_1 = 3, J_1 = 3, \ell'_1 = 1$	$1.5269 \cdot 10^{-1}$
$J_1 = 2, \ell'_1 = 2, J_1 = 2, \ell'_1 = 4$	$-9.9581 \cdot 10^{-2}$
$J_1 = 3, \ell'_1 = 1, J_1 = 2, \ell'_1 = 2$	$-7.1938 \cdot 10^{-2}$
$J_1 = 3, \ell'_1 = 1, J_1 = 2, \ell'_1 = 4$	$-7.0513 \cdot 10^{-2}$
$J_1 = 3, \ell'_1 = 3, J_1 = 2, \ell'_1 = 2$	$-8.0941 \cdot 10^{-2}$
$J_1 = 3, \ell'_1 = 3, J_1 = 2, \ell'_1 = 4$	$-7.4315 \cdot 10^{-4}$
$J_1 = 4, \ell'_1 = 4, J_1 = 5, \ell'_1 = 5$	$2.0983 \cdot 10^{-4}$

Table C.4: Coefficients for α - γ -correlation function for $E_\alpha = 10.3$ MeV.

$W_{J_i, \ell'_i}(\theta)$	w_i
$J = 2, \ell' = 2$	$-4.6236 \cdot 10^{-2}$
$J = 2, \ell' = 4$	$3.1473 \cdot 10^{-5}$
$J = 3, \ell' = 3$	$2.8445 \cdot 10^{-1}$
$J = 3, \ell' = 1$	$-1.6195 \cdot 10^{-1}$
$J_1 = 2, \ell'_1 = 2, J_1 = 2, \ell'_2 = 4$	$-2.3801 \cdot 10^{-1}$
$J_1 = 2, \ell'_1 = 2, J_1 = 3, \ell'_2 = 3$	$-9.3584 \cdot 10^{-2}$
$J_1 = 2, \ell'_1 = 2, J_1 = 3, \ell'_1 = 1$	$-8.2672 \cdot 10^{-2}$
$J_1 = 2, \ell'_1 = 4, J_1 = 3, \ell'_1 = 3$	$-2.8851 \cdot 10^{-4}$
$J_1 = 2, \ell'_1 = 4, J_1 = 3, \ell'_1 = 1$	$-8.1489 \cdot 10^{-2}$
$J_1 = 3, \ell'_1 = 3, J_1 = 3, \ell'_1 = 1$	$-1.1287 \cdot 10^{-2}$

Table C.5: Coefficients for α - γ -correlation function for $E_\alpha = 10.5$ MeV.

$W_{J_i, \ell'_i}(\theta)$	w_i
$J = 3, \ell' = 3$	$3.4811 \cdot 10^{-1}$
$J = 3, \ell' = 1$	$2.0133 \cdot 10^{-1}$
$J_1 = 3, \ell'_1 = 3, J_1 = 3, \ell'_2 = 1$	$4.5057 \cdot 10^{-1}$

Table C.6: Coefficients for α - γ -correlation function for $E_\alpha = 10.95$ MeV.

$W_{J_i, \ell'_i}(\theta)$	w_i
$J = 1, \ell' = 1$	$1.1888 \cdot 10^{-1}$
$J = 1, \ell' = 3$	$-2.2543 \cdot 10^{-1}$
$J = 6, \ell' = 6$	$1.7897 \cdot 10^{-1}$
$J = 6, \ell' = 4$	$1.0502 \cdot 10^{-4}$
$J_1 = 1, \ell'_1 = 1, J_1 = 1, \ell'_2 = 3$	$1.5269 \cdot 10^{-1}$
$J_1 = 1, \ell'_1 = 1, J_1 = 6, \ell'_2 = 6$	$-9.9581 \cdot 10^{-2}$
$J_1 = 1, \ell'_1 = 1, J_1 = 6, \ell'_1 = 4$	$-7.1938 \cdot 10^{-2}$
$J_1 = 1, \ell'_1 = 3, J_1 = 6, \ell'_1 = 6$	$-7.0513 \cdot 10^{-2}$
$J_1 = 1, \ell'_1 = 3, J_1 = 6, \ell'_1 = 4$	$-8.0941 \cdot 10^{-2}$
$J_1 = 6, \ell'_1 = 6, J_1 = 6, \ell'_1 = 4$	$-7.4315 \cdot 10^{-4}$

Table C.7: Coefficients for α - γ -correlation function for $E_\alpha = 11.57$ MeV.

Acknowledgment

Mein besonderer Dank gilt Dr. Woon Yong Baek, der mich fachlich, methodisch und persönlich, mit großem Engagement, mit Rat und Tat unterstützt hat.

Bedanken möchte ich mich auch bei Dr. Hans Rabus für die vielen konstruktiven Diskussionen, seine Ratschläge und dass er sich stets Zeit für meine Anliegen genommen hat.

Professor Dr. Hans Hofsäss möchte ich für die Betreuung seitens der Universität Göttingen, für die sehr hilfreichen fachlichen Diskussionen und für die Beschichtung meiner Eintrittsfenster meinen Dank aussprechen.

Dr. Ullrich Vetter danke ich auch für die Übernahme meiner Betreuung und seine wertvollen Anregungen.

Ebenso danke ich Professor Dr. Tim Salditt für seine Bereitschaft, meine Arbeit zu begutachten.

PD Dr. Frank Wissmann danke ich für die Möglichkeit, mich an der Lehre im Rahmen seiner Vorlesung zu beteiligen.

Dr. Herbert Janßen danke ich für sein stetes Interesse an meiner Arbeit und die Unterstützung bei der Anschaffung des Detektors.

Ein besonderes Dankeschön geht an Wolfgang Helms und Andreas Pausewang für ihre Unterstützung bei den experimentellen Aufbauten vor den Strahlzeiten. Felix Duwe und Vincent Hahn danke ich für die Fertigung der mechanischen Teile und Beate Lambertsen für ihre Unterstützung während den Strahlzeiten.

Dem Team am Zyklotron-Beschleuniger möchte ich für ihren Einsatz danken, der einen reibungslosen Ablauf ermöglichte.

Heike Nittmann und Sandra Otto danke ich für die Unterstützung bei der Fertigstellung der Dissertation.

Björn Pullner danke ich für seine Unterstützung bei der Planung der Mechanik der Verstelleinrichtung.

Ich danke allen Kollegen für die angenehme Atmosphäre, die gute Zusammenarbeit sowie die unterhaltsamen Kaffeepausen.

Meinen Eltern Elisabeth und Siegbert Rahm danke ich für ihre anhaltende bedingungslose Unterstützung meiner Entscheidungen. Danke auch an Marion Bug für die vielen fachlichen Diskussionen, ihren Beistand und ihre Motivation.

Lebenslauf

Persönliche Daten

Johannes Martin Rahm
Hertzstraße 14
38104 Braunschweig
Tel.: 01 79/ 7 98 06 75
E-Mail: johannes.rahm@gmx.de
geb. am 31. Oktober 1983 in Fulda
ledig, deutsch

Berufserfahrung

- 03/2004–06/2005 Jumo Mess & Regeltechnik, Abteilung Analysemesstechnik
- 08/2011–03/2012 Wissenschaftlicher Mitarbeiter an der Medizinischen Fakultät Carl Gustav Carus der Technischen Universität Dresden.
Arbeitsgruppe:
In-vivo Dosimetrie für neue Strahlenarten
- 04/2012 Wissenschaftlicher Mitarbeiter im Fachbereich 6.5 der Physikalisch-Technischen Bundesanstalt Braunschweig.
Arbeitsgruppe:
Phaseneffekte bei der Strahlenwirkung

Ausbildung

- 07/2000 **Realschulabschluss** Rhönschule Gersfeld
- 08/2000–02/2004 Ausbildung zum **Mechatroniker**, Jumo Mess & Regeltechnik
- 08/2005–06/2007 Besuch der 2 jährigen Fachschule für Technik und Gestaltung
Fachrichtung Elektrotechnik.
Abschluss als **staatlich geprüfter Techniker** mit Fachhochschulreife und Ausbildereignung.
Technikerprojekt Thema:
Steuerung und Visualisierung eines Schichtspeicherkessels
- 10/2007–07/2011 Studium der Medizintechnik FH Gießen–Friedberg
- 10/2010–02/2011 Praxissemester Physikalisch–Technische Bundesanstalt Braunschweig,
Fachbereich 6.4 *“Ionenbeschleuniger und Referenzstrahlungsfelder”*

- 07/2011 Abschluss **Diplom–Ingenieur (FH) Medizintechnik.**
 Titel der Diplomarbeit:
Dosimetrie komplexer Strahlungsfelder mit gewebeäquivalenten Proportionalzählern an der Physikalisch–Technischen Bundesanstalt in Braunschweig im Fachbereich 6.4.
- Seit 10/2012 Promotionsstudent im Fach Physik an der Georg–August–Universität Göttingen.
 Thema:
Measurement of the stopping power of water for carbon ions in the energy range between 1 MeV - 6 MeV using the inverted Doppler-shift attenuation method an der Physikalisch–Technischen Bundesanstalt in Braunschweig im Fachbereich 6.5.

Stipendium

- 03/2010 Aufnahme in die Förderung der Studienstiftung des deutschen Volkes

Patente

- 09/2014 Einrichtung zur Bestimmung der Dosisdeposition von Teilchenstrahlung zur Tumorbehandlung in Gewebe,
German Patent DE102013212983.
- 03/2015 Vorrichtung und Verfahren zur Bestimmung der Lage eines Teilchenstrahls, zum Patent eingereicht.

Weitere Qualifikationen

- | | |
|----------------|---|
| Sprachen | Englisch in Wort und Schrift |
| Office | Microsoft Office, Adobe Illustrator, L ^A T _E X |
| Programmierung | C/C++, Matlab, Scilab, ROOT, Geant4, JAVA (ImageJ), Microcontroller (Atmel, Microchip PIC), FORTRAN |

Göttingen, 27.09.2016